Jordan Journal of
PHYSICS
An International Peer-Reviewed Research Journal

Volume 14, No. 5, December 2021, Jumada-Al-Awwal 1443 H

Jordan Journal of Physics (*JJP*): An International Peer-Reviewed Research Journal funded by the Scientific Research Support Fund, Jordan, and published quarterly by the Deanship of Research and Graduate Studies, Yarmouk University, Irbid, Jordan.

Manuscripts should be submitted to:

Prof. Ibrahim O. Abu Al-Jarayesh
Editor-in-Chief, Jordan Journal of Physics
Deanship of Research and Graduate Studies
Yarmouk University-Irbid-Jordan
Tel. 00 962 2 7211111 Ext. 2075
E-mail: *jjp@yu.edu.jo*
Website: *http://Journals.yu.edu.jo/jjp*

Jordan Journal of
PHYSICS
An International Peer-Reviewed Research Journal

Volume 14, No. 5, December 2021, Jumada-Al-Awwal 1443 H

The Hashemite Kingdom of Jordan

Yarmouk University

Jordan Journal of PHYSICS

An International Peer-Reviewed Research Journal
Funded by the Scientific Research Support Fund

Volume 14, No. 5, December 2021, Jumada-Al-Awwal 1443 H

Instructions to Authors

Instructions to authors concerning manuscript organization and format apply to hardcopy submission by mail, and also to electronic online submission via the Journal homepage website (http://jjp.yu.edu.jo).

Manuscript Submission

1- **E-mail to** : jjp@yu.edu.jo

2- **Online**: Follow the instructions at the journal homepage website.

Original *Research Articles*, *Communications* and *Technical Notes* are subject to critical review by minimum of two competent referees. Authors are encouraged to suggest names of competent reviewers. *Feature Articles* in active Physics research fields, in which the author's own contribution and its relationship to other work in the field constitute the main body of the article, appear as a result of an invitation from the Editorial Board, and will be so designated. The author of a *Feature Article* will be asked to provide a clear, concise and critical status report of the field as an introduction to the article. *Review Articles* on active and rapidly changing Physics research fields will also be published. Authors of *Review Articles* are encouraged to submit two-page proposals to the Editor-in-Chief for approval. Manuscripts submitted in *Arabic* should be accompanied by an Abstract and Keywords in English.

Organization of the Manuscript

Manuscripts should be typed double spaced on one side of A4 sheets (21.6 x 27.9 cm) with 3.71 cm margins, using Microsoft Word 2000 or a later version thereof. The author should adhere to the following order of presentation: Article Title, Author(s), Full Address and E-mail, Abstract, PACS and Keywords, Main Text, Acknowledgment. Only the first letters of words in the Title, Headings and Subheadings are capitalized. Headings should be in **bold** while subheadings in *italic* fonts.

Title Page: Includes the title of the article, authors' first names, middle initials and surnames and affiliations. The affiliation should comprise the department, institution (university or company), city, zip code and state and should be typed as a footnote to the author's name. The name and complete mailing address, telephone and fax numbers, and e-mail address of the author responsible for correspondence (designated with an asterisk) should also be included for official use. The title should be carefully, concisely and clearly constructed to highlight the emphasis and content of the manuscript, which is very important for information retrieval.

Abstract: A one paragraph abstract not exceeding 200 words is required, which should be arranged to highlight the purpose, methods used, results and major findings**.**

Keywords: A list of 4-6 keywords, which expresses the precise content of the manuscript for indexing purposes, should follow the abstract.

PACS: Authors should supply one or more relevant PACS-2006 classification codes, (available at http://www.aip.org/pacs/pacs06/pacs06-toc.html)

Introduction: Should present the purpose of the submitted work and its relationship to earlier work in the field, but it should not be an extensive review of the literature (e.g., should not exceed 1 ½ typed pages).

Experimental Methods: Should be sufficiently informative to allow competent reproduction of the experimental procedures presented; yet concise enough not to be repetitive of earlier published procedures.

Results: should present the results clearly and concisely.

Discussion: Should be concise and focus on the interpretation of the results.

Conclusion: Should be a brief account of the major findings of the study not exceeding one typed page.

Acknowledgments: Including those for grant and financial support if any, should be typed in one paragraph directly preceding the References.

References: References should be typed double spaced and numbered sequentially in the order in which they are cited in the text. References should be cited in the text by the appropriate Arabic numerals, enclosed in square brackets. Titles of journals are abbreviated according to list of scientific periodicals. The style and punctuation should conform to the following examples:

1. Journal Article:

a) Heisenberg, W., Z. Phys. 49 (1928) 619.
b) Bednorz, J. G. and Müller, K. A., Z. Phys. B64 (1986) 189
c) Bardeen, J., Cooper, L.N. and Schrieffer, J. R., Phys. Rev. 106 (1957) 162.
d) Asad, J. H., Hijjawi, R. S., Sakaji, A. and Khalifeh, J. M., Int. J. Theor. Phys. 44(4) (2005), 3977.

2. Books with Authors, but no Editors:

a) Kittel, C., "Introduction to Solid State Physics", 8th Ed. (John Wiley and Sons, New York, 2005), chapter 16.
b) Chikazumi, S., C. D. Graham, JR, "Physics of Ferromagnetism", 2nd Ed. (Oxford University Press, Oxford, 1997).

3. Books with Authors and Editors:

a) Allen, P. B. "Dynamical Properties of Solids", Ed. (1), G. K. Horton and A. A. Maradudin (North-Holland, Amsterdam, 1980), p137.
b) Chantrell, R. W. and O'Grady, K., "Magnetic Properities of Fine Particles" Eds. J. L. Dormann and D. Fiorani (North-Holland, Amsterdam, 1992), p103.

4. Technical Report:

Purcell, J. "The Superconducting Magnet System for the 12-Foot Bubble Chamber", report ANL/HEP6813, Argonne Natt. Lab., Argonne, III, (1968).

5. Patent:

Bigham, C. B., Schneider, H. R., US patent 3 925 676 (1975).

6. Thesis:

Mahmood, S. H., Ph.D. Thesis, Michigan State University, (1986), USA (Unpublished).

7. Conference or Symposium Proceedings:

Blandin, A. and Lederer, P. Proc. Intern. Conf. on Magnetism, Nottingham (1964), P.71.

8. Internet Source:

Should include authors' names (if any), title, internet website, URL, and date of access.

9. Prepublication online articles (already accepted for publication):

Should include authors' names (if any), title of digital database, database website, URL, and date of access.

For other types of referenced works, provide sufficient information to enable readers to access them.

Tables: Tables should be numbered with Arabic numerals and referred to by number in the Text (e.g., Table 1). Each table should be typed on a separate page with the legend above the table, while explanatory footnotes, which are indicated by superscript lowercase letters, should be typed below the table.

Illustrations: Figures, drawings, diagrams, charts and photographs are to be numbered in a consecutive series of Arabic numerals in the order in which they are cited in the text. Computer-generated illustrations and good-quality digital photographic prints are accepted. They should be black and white originals (not photocopies) provided on separate pages and identified with their corresponding numbers. Actual size graphics should be provided, which need no further manipulation, with lettering (Arial or Helvetica) not smaller than 8 points, lines no thinner than 0.5 point, and each of uniform density. All colors should be removed from graphics except for those graphics to be considered for publication in color. If graphics are to be submitted digitally, they should conform to the following minimum resolution requirements: 1200 dpi for black and white line art, 600 dpi for grayscale art, and 300 dpi for color art. All graphic files must be saved as TIFF images, and all illustrations must be submitted in the actual size at which they should appear in the journal. Note that good quality hardcopy original illustrations are required for both online and mail submissions of manuscripts.

Text Footnotes: The use of text footnotes is to be avoided. When their use is absolutely necessary, they should be typed at the bottom of the page to which they refer, and should be cited in the text by a superscript asterisk or multiples thereof. Place a line above the footnote, so that it is set off from the text.

Supplementary Material: Authors are encouraged to provide all supplementary materials that may facilitate the review process, including any detailed mathematical derivations that may not appear in whole in the manuscript.

Revised Manuscript and Computer Disks

Following the acceptance of a manuscript for publication and the incorporation of all required revisions, authors should submit an original and one more copy of the final disk containing the complete manuscript typed double spaced in Microsoft Word for Windows 2000 or a later version thereof. All graphic files must be saved as PDF, JPG, or TIFF images.

Allen, P.B., "…….", in: Horton, G.K., and Muradudin, A. A., (eds.), "Dynamical…….", (North……..), pp….

Reprints

Twenty (20) reprints free of charge are provided to the corresponding author. For orders of more reprints, a reprint order form and prices will be sent with the article proofs, which should be returned directly to the Editor for processing.

Copyright

Disclaimer

Indexing

JJP is currently indexing in:

Scopus	ULRICHSWEB GLOBAL SERIALS DIRECTORY

Jordan Journal of
PHYSICS
An International Peer-Reviewed Research Journal

Volume 14, No. 5, December 2021, Jumada-Al-Awwal 1443 H

Table of Contents:

Volume 14, Number 5, 2021. pp. 379-408

Jordan Journal of Physics

REVIEW ARTICLE

The Electromagnetic Field outside the Steadily Rotating Relativistic Uniform System

Sergey G. Fedosin

P.O. Box 614088, Sviazeva Str. 22-79, Perm, Perm Krai, Russia.

Doi: **https://doi.org/10.47011/14.5.1**

Received on: 14/01/2021; *Accepted on: 24/06/2021*

Abstract: Using the method of retarded potentials, approximate formulae are obtained that describe the electromagnetic field outside the relativistic uniform system in the form of a charged sphere rotating at a constant speed. For the near, middle and far zones, the corresponding expressions are found for the scalar and vector potentials, as well as for the electric and magnetic fields. Then, these expressions are assessed for correspondence to the Laplace equations for potentials and fields. One of the purposes is to test the truth of the assumption that the scalar potential and the electric field depend neither on the value of the angular velocity of rotation of the sphere nor on the direction to the point where the field is measured. However, calculations show that potentials and fields increase as the observation point gets closer to the sphere's equator and to the sphere's surface, compared with the case for a stationary sphere. In this case, additions are proportional to the square of the angular velocity of rotation and the square of the sphere's radius and inversely proportional to the square of the speed of light. The largest found relative increase in potentials and fields could reach the value of 4% for the rapidly rotating neutron star PSR J1614-2230, if the star were charged. For a proton, a similar increase in fields on its surface near the equator reaches 54%.

Keywords: Electromagnetic field, Relativistic uniform system, Rotation.

1. Introduction

In article [1], it is emphasized that in most cases, calculation of the components of electromagnetic field of rapidly changing currents is extremely difficult. Even in simple configurations of moving charges, it appears that non-elementary integrals cannot be expressed in terms of simple functions. The simplest example is a current loop and already here, we have to deal with elliptic integrals. To determine the field components, Maxwell equations for the vector potential were integrated in [1] using Laplace transformation and the solution was found in the form of a sum with the help of Legendre polynomials for the charged spherical shell during its rotation in different cases, including change in the charge configuration on the surface and accelerated rotation.

The solution for the rotating uniformly charged sphere's surface can be found in [2], where the magnetic field was expressed as a vector in the spherical reference frame. In [3], the vector potential and magnetic field are calculated for a uniformly charged rotating sphere. A more complicated situation, where the matter inside the sphere or cylinder is a conductor and an additional charge appears during rotation from the centripetal force and inertia of electrons, is considered in [4-5].

In [6], rotating cylindrical charge distribution was studied and a solution was obtained for the magnetic and electric fields around the rotating sphere. Then, in [7] a general solution was found for symmetric rotating charge distributions.

Corresponding Author: Sergey G. Fedosin **Email**: sergey.fedosin@gmail.com

In contrast to these works, we consider not just uniformly charged matter distributed inside the sphere or in its shell, but a relativistic uniform system. This means that the matter in the sphere's volume is in equilibrium with the gravitational forces, pressure field and acceleration field and the charged particles can move chaotically and have the same invariant charge density. If such a system of particles rotates at a certain constant angular velocity, this leads to the corresponding vector potential and magnetic field, which do not depend on time. We will calculate all the components of the electromagnetic field outside the system, including the scalar and vector potentials, electric and magnetic fields. Previously, these quantities were found in [8-12] for the case of a uniform system at rest without rotation, in which the vector potentials are equal to zero.

The study of a rotating relativistic uniform system is important in itself and it is of academic interest from the point of view of developing an ideal model corresponding to the relativistic approach. But, there are also a number of physical problems, such as calculating the angular momentum, magnetic moment and relativistic energy of rotating objects, where it is necessary to correctly estimate the contributions of various fields associated with these objects.

As a rule, in articles describing a steadily rotating spherical shell, it is assumed that the electric field outside the sphere does not depend on the angular velocity of rotation. In contrast to this, in [13] it is indicated that there is such a dependence both for the electric and magnetic fields. In [14], this question was considered again and an error in calculations was found in [13], associated with the replacement of the partial time derivative with the total derivative.

To check the assumption about the possible dependence of the fields on the angular velocity of rotation and to estimate the contribution from the particles' motion inside the system, the accuracy of our calculations will be increased up to the terms containing the square and even the third power of the speed of light in the denominator. The method of retarded potentials used for calculations provides the result based on first principles, which reduces possible inaccuracies that appear under additional assumptions.

2. Statement of the Problem

The standard equations for the electric field strength $\mathbf{E}$, magnetic field induction $\mathbf{B}$ and electromagnetic field potentials in the framework of the special theory of relativity have the following form:

$$\nabla\cdot\mathbf{E}=\frac{\gamma\rho_{0q}}{\varepsilon_0},\qquad \nabla\times\mathbf{B}=\mu_0\mathbf{j}+\frac{1}{c^2}\frac{\partial\mathbf{E}}{\partial t},$$

$$\nabla\cdot\mathbf{B}=0,\ \nabla\times\mathbf{E}=-\frac{\partial\mathbf{B}}{\partial t}. \qquad (1)$$

$$\partial_\beta\partial^\beta\varphi=\frac{1}{c^2}\frac{\partial^2\varphi}{\partial t^2}-\Delta\varphi=\frac{\gamma\rho_{0q}}{\varepsilon_0},$$

$$\partial_\beta\partial^\beta\mathbf{A}=\frac{1}{c^2}\frac{\partial^2\mathbf{A}}{\partial t^2}-\Delta\mathbf{A}=\mu_0\mathbf{j}. \qquad (2)$$

$$\mathbf{E}=-\nabla\varphi-\frac{\partial\mathbf{A}}{\partial t},\ \mathbf{B}=\nabla\times\mathbf{A},\ A_\mu=\left(\frac{\varphi}{c},-\mathbf{A}\right). \qquad (3)$$

For the particles moving inside the rotating sphere: $\gamma=\dfrac{1}{\sqrt{1-v^2/c^2}}$ is the Lorentz factor; $\mathbf{v}$ is the particles' velocity in the reference frame K, in which the sphere is rotating; ρ_{0q} is the charge density of a moving particle in the comoving reference frame; ε_0 is the electrical constant; μ_0 is the magnetic constant; $\mathbf{j}=\gamma\rho_{0q}\mathbf{v}$ denotes the vector of the electric current density; c is the speed of light, while $\mu_0\varepsilon_0c^2=1$; A_μ is the four-potential of the electromagnetic field; φ and $\mathbf{A}$ are the scalar and vector potentials. Wave equations (2) for the potentials are obtained from equations (1) taking into account (3).

If the sphere with the particles rotates at a constant angular velocity ω, the potentials would not depend on time. Then, the time derivatives disappear in (2) and the following remains:

$$\Delta\varphi=-\frac{\gamma\rho_{0q}}{\varepsilon_0},\ \Delta\mathbf{A}=-\mu_0\mathbf{j}=-\mu_0\gamma\rho_{0q}\mathbf{v}. \qquad (4)$$

Eqs. (4) were solved in the absence of rotation, when $\omega=0$, for a relativistic uniform system [11]. In this case, the Lorentz factor γ'

of the particles' motion relative to the reference frame K', associated with the center of the fixed sphere, was substituted instead of γ in (4). For the spherical system with the particles in the absence of the matter's general rotation, the Lorentz factor according to [8] is equal to:

$$\gamma'(\omega=0)=\frac{c\gamma'_c}{r\sqrt{4\pi\eta\rho_0}}\sin\left(\frac{r}{c}\sqrt{4\pi\eta\rho_0}\right)\approx\gamma'_c-\frac{2\pi\eta\rho_0 r^2\gamma'_c}{3c^2}. \quad (5)$$

In (5), r is the current radius, γ'_c is the Lorentz factor at the center of the sphere, η is the acceleration field coefficient and ρ_0 is the mass density of a moving particle in the comoving reference frame. Taking this into account, the scalar (electric) potential φ_i inside the sphere and the similar potential φ_o outside the sphere are defined by the expressions:

$$\varphi_i=\frac{\rho_{0q}c^2\gamma'_c}{4\pi\varepsilon_0\eta\rho_0 r}\left[\frac{c}{\sqrt{4\pi\eta\rho_0}}\sin\left(\frac{r}{c}\sqrt{4\pi\eta\rho_0}\right)-r\cos\left(\frac{a}{c}\sqrt{4\pi\eta\rho_0}\right)\right]\approx\frac{\rho_{0q}\gamma'_c(3a^2-r^2)}{6\varepsilon_0}. \quad (6)$$

$$\left.\begin{aligned}q_b=\rho_{0q}\int\gamma'(\omega=0)\,dV_s=\frac{\rho_{0q}c^2\gamma'_c}{\eta\rho_0}\left[\frac{c}{\sqrt{4\pi\eta\rho_0}}\sin\left(\frac{a}{c}\sqrt{4\pi\eta\rho_0}\right)-a\cos\left(\frac{a}{c}\sqrt{4\pi\eta\rho_0}\right)\right]\approx\\ \approx\frac{4\pi\rho_{0q}a^3\gamma'_c}{3}\left(1-\frac{2\pi\eta\rho_0a^2}{5c^2}\right)=q\gamma'_c\left(1-\frac{3\eta m}{10ac^2}\right)\end{aligned}\right\} \quad (8)$$

As for the vector (magnetic) potential $\mathbf{A}$ in (4), on the average, it turns out to be equal to zero everywhere due to the chaotic motion of particles.

The particles' rotation at the angular velocity ω about the axis OZ that passes through the center of the sphere changes the particles' linear velocities. Taking into account the rule of relativistic addition of velocities, for the absolute velocity and the Lorentz factor of an arbitrary particle, we find the following:

$$\mathbf{v}=\frac{\mathbf{v}'+\frac{(\gamma_r-1)(\mathbf{v}'\mathbf{v}_r)}{v_r^2}\mathbf{v}_r+\gamma_r\mathbf{v}_r}{\gamma_r\left(1+\frac{\mathbf{v}'\mathbf{v}_r}{c^2}\right)},$$

$$\gamma=\gamma'\gamma_r\left(1+\frac{\mathbf{v}'\mathbf{v}_r}{c^2}\right), \quad (9)$$

where $\mathbf{v}'$ is the velocity of chaotic motion of a particle in the reference frame K' rotating with the matter at the angular velocity ω; $\mathbf{v}_r$ is the linear velocity of motion of the reference frame K' at the particle's location, arising due to rotation in the reference frame K; $\gamma_r=\frac{1}{\sqrt{1-v_r^2/c^2}}$ is the Lorentz factor for the velocity $\mathbf{v}_r$, $\gamma'=\frac{1}{\sqrt{1-v'^2/c^2}}$ is the Lorentz factor for the velocity $\mathbf{v}'$.

Expressions (9) should be averaged over the volume in a small neighborhood of the point under consideration so that a sufficient number of particles would be present in this volume. Due to the chaotic character of motion, the velocities $\mathbf{v}'$ of neighboring particles are directed in different ways. As a result, the average values will be: $\overline{\mathbf{v}}=\mathbf{v}_r$, $\overline{\gamma}=\gamma'\gamma_r$. Next, we will assume that, despite the general rotation, formula (5) for γ' continues to be valid in the reference frame K', with the exception that instead of the Lorentz factor γ'_c at the center of the sphere, the

$$\varphi_o=\frac{\rho_{0q}c^2\gamma'_c}{4\pi\varepsilon_0\eta\rho_0 r}\left[\frac{c}{\sqrt{4\pi\eta\rho_0}}\sin\left(\frac{a}{c}\sqrt{4\pi\eta\rho_0}\right)-a\cos\left(\frac{a}{c}\sqrt{4\pi\eta\rho_0}\right)\right].$$

$$\varphi_o=\frac{q_b}{4\pi\varepsilon_0 r}\approx\frac{q\gamma'_c}{4\pi\varepsilon_0 r}\left(1-\frac{3\eta m}{10ac^2}\right). \quad (7)$$

In (7), the quantity q is the product of ρ_{0q} by the volume V_s of the sphere of radius a; that is $q=\frac{4\pi\rho_{0q}a^3}{3}$. Similarly, m is the product of the invariant mass density ρ_0 of the matter's particles by the sphere's volume. However, the external potential φ_o of the electric field does not depend on q, but it depends on the total charge q_b of the sphere, defined by the expression:

formula must contain a quantity denoted as γ_c. Indeed, γ_c' is determined in the absence of rotation, but the Lorentz factor at the center of the sphere can be changed due to rotation and turn into γ_c.

2.1 Potentials outside the Rotating Sphere

The charge density ρ_{0q} outside the sphere is zero due to the absence of charged particles there. This simplifies the form of equations (4), which turn into Laplace equations:

$$\Delta\varphi = 0,\ \Delta\mathbf{A} = 0. \qquad (10)$$

From the great number of possible solutions of equations (10), we should choose those that, in the absence of rotation, go over to the solution of (7) for the scalar potential φ_o and to the solution $\mathbf{A}_o = 0$ for the vector potential.

In order to find the necessary solutions, we will use the Lienard-Wiechert approach for retarded potentials. Let us assume that a point charged particle rotates along a circle of radius ρ at the angular velocity ω and with the linear velocity $v_r = \omega\rho$. We will place the cylindrical reference frame with coordinates ρ, ϕ, z_d at the center of the sphere and will search for the electromagnetic field potentials from the rotating charge at a certain remote point P with the radius vector $\mathbf{R} = (x, y, z)$.

The current position of the charge is given by the radius vector

$$r_q = (\rho\cos\phi, \rho\sin\phi, z_d) = [\rho\cos(\omega t + \phi_0), \rho\sin(\omega t + \phi_0), z_d],$$

so that the circle of rotation is parallel to the plane XOY, while the angle ϕ depends on the current time: $\phi = \omega t + \phi_0$; here, the constant ϕ_0 is the initial phase.

The vector from the charge to the point P will be as follows:

$$R_P = R - r_q = [x - \rho\cos(\omega t + \phi_0), y - \rho\sin(\omega t + \phi_0), z - z_d],$$

wherein

$$R_P = \left.\begin{array}{l}\sqrt{(x-\rho\cos\phi)^2 + (y-\rho\sin\phi)^2 \\ \quad +(z-z_d)^2} \\ = \sqrt{\begin{array}{l}R^2 + z_d^2 - 2zz_d + \rho^2 \\ -2\rho x\cos\phi - 2\rho y\sin\phi\end{array}}.\end{array}\right\} \qquad (11)$$

The Lienard-Wiechert formulae for the scalar and vector potentials of one particle with the number n have the following form:

$$\varphi_n = \frac{q_n}{4\pi\varepsilon_0\left(\hat{R}_P - \hat{\mathbf{v}}\cdot\hat{\mathbf{R}}_P / c\right)},$$

$$\mathbf{A}_n = \frac{\mu_0 q_n \hat{\mathbf{v}}}{4\pi\left(\hat{R}_P - \hat{\mathbf{v}}\cdot\hat{\mathbf{R}}_P / c\right)}. \qquad (12)$$

Here, $\hat{\mathbf{R}}_P = \mathbf{R} - \hat{\mathbf{r}}_q$ is the vector from the charge to the point P at the early time point $\hat{t} = t - \frac{\hat{R}_P}{c}$; the radius vector

$$\hat{r}_q = (\rho\cos\hat{\phi}, \rho\sin\hat{\phi}, z_p) = [\rho\cos(\omega\hat{t} + \phi_0), \rho\sin(\omega\hat{t} + \phi_0), z_d]$$

defines the position of the charge at the time point $\hat{t}$, while

$$\hat{R}_P = \sqrt{\left(x - \rho\cos\hat{\phi}\right)^2 + \left(y - \rho\sin\hat{\phi}\right)^2 + (z - z_d)^2}.$$

The current rotation velocity of the charge is $\mathbf{v}_r = \frac{d\mathbf{r}_q}{dt} = (-\omega\rho\sin\phi, \omega\rho\cos\phi, 0)$ and the charge's velocity at the early time point will be

$$\hat{\mathbf{v}}_r = \mathbf{v}_r(\hat{t}) = \frac{d\hat{\mathbf{r}}_q}{d\hat{t}} = (-\omega\rho\sin\hat{\phi}, \omega\rho\cos\hat{\phi}, 0),$$

wherein $\hat{\phi} = \omega\hat{t} + \phi_0 = \omega t + \phi_0 - \frac{\omega\hat{R}_P}{c} = \phi - \frac{\omega\hat{R}_P}{c} = \phi - \phi_P$.

Since, according to (9), the average velocity of the particles' motion is $\overline{\mathbf{v}} = \mathbf{v}_r$, in (12), $\hat{\mathbf{v}}_r$ should be used instead of $\hat{\mathbf{v}}$. Then, for $\hat{R}_P$ and the product $\hat{\mathbf{v}}_r\cdot\hat{\mathbf{R}}_P$ in (12), we obtain:

$$\hat{R}_P = \sqrt{\begin{array}{l}R^2 + z_d^2 - 2zz_d + \rho^2 \\ -2\rho x\cos\hat{\phi} - 2\rho y\sin\hat{\phi}\end{array}},$$

$$\hat{\mathbf{v}}_r\cdot\hat{\mathbf{R}}_P = \omega\rho y\cos\hat{\phi} - \omega\rho x\sin\hat{\phi}. \qquad (13)$$

Let's locate the coordinate z_d in such a way that it would define the location of a thin layer with thickness s in the form of a disk parallel to the plane XOY. The radius of such a disk inside the sphere will be $\rho_d = \sqrt{a^2 - z_d^2}$, where the sphere's radius is a. The sphere is tightly filled with rotating particles and the same applies to this disk. We will use the principle of superposition of potentials and will find the scalar potential at the remote point P from the rotating disk with charged particles. For this purpose, we need to take the sum over all N charges in the disk. In view of (12), for the scalar potential, we have the following:

$$\varphi_d = \sum_{n=1}^{N} \varphi_n = \frac{1}{4\pi\varepsilon_0} \sum_{n=1}^{N} \frac{q_n}{\left(\hat{R}_P - \hat{\mathbf{v}}_r \cdot \hat{\mathbf{R}}_P / c\right)_n}. \quad (14)$$

Each charge q_n inside the disk has its own rotation radius ρ_n and motion velocity $v_n = \omega\rho_n$, while the instantaneous position of the charge is given by the vector $\mathbf{r}_{qn} = (\rho_n \cos\phi_n, \rho_n \sin\phi_n, z_d)$. In this regard, in (14), the denominator depends on the location of the particle in the disk and therefore, it has an index n.

The charge of a point particle rotating in the disk can be expressed in terms of the invariant charge density, Lorentz factor and moving volume:

$$q_n = \frac{\rho_{0q}\gamma s \rho\, d\rho\, d\phi}{\gamma_r}.$$

The quantity $\frac{s\rho d\rho d\phi}{\gamma_r}$ here specifies the element of the volume of a rotating disk, which, as a result of Lorentz contraction, is γ_r times less than the volume element $s\rho d\rho d\phi$ of the fixed disk. The quantity $\rho_{0q}\gamma$ defines the effective density of the charge, taking into account its rotation inside the disk and the chaotic motion of particles. As γ in (15), we should substitute the averaged value of the Lorentz factor $\overline{\gamma} = \gamma'\gamma_r$, according to (9). This gives the following:

$$q_n = \rho_{0q}\gamma' s \rho\, d\rho\, d\phi. \quad (15)$$

The charge q_n is expressed in terms of the product of differentials, so that the sum (14) can be transformed into an integral. With this in mind, from (13-15), it follows:

$$\varphi_d = \frac{s\rho_{0q}}{4\pi\varepsilon_0} \int_0^{2\pi} \int_0^{\rho_d} \frac{\gamma'\, \rho\, d\rho\, d\phi}{\sqrt{R^2 + z_d^2 - 2zz_d + \rho^2 - 2\rho x\cos\hat{\phi} - 2\rho y\sin\hat{\phi}} + \frac{\omega\rho x\sin\hat{\phi}}{c} - \frac{\omega\rho y\cos\hat{\phi}}{c}}. \quad (16)$$

In order to be able to perform integration, in (16), we need to express the angle $\hat{\phi}$, defining the position of an arbitrary particle at the early time point $\hat{t}$, in terms of the angle ϕ at the time point t. Since $\phi = \omega t + \phi_0$, $\hat{\phi} = \omega\hat{t} + \phi_0$ and $\hat{t} = t - \frac{\hat{R}_P}{c}$, we will have $\hat{\phi} = \phi - \frac{\omega\hat{R}_P}{c}$ and therefore,

$$\cos\hat{\phi} = \cos\phi\cos\frac{\omega\hat{R}_P}{c} + \sin\phi\sin\frac{\omega\hat{R}_P}{c},$$

$$\sin\hat{\phi} = \sin\phi\cos\frac{\omega\hat{R}_P}{c} - \cos\phi\sin\frac{\omega\hat{R}_P}{c}. \quad (17)$$

From comparison of (12) and (16), it follows that the vector potential of the rotating disk will be equal to:

$$A_d = \frac{\mu_0 s\rho_{0q}}{4\pi} \int_0^{2\pi} \int_0^{\rho_d} \frac{\gamma'\, \hat{v}_r \rho\, d\rho\, d\phi}{\sqrt{R^2 + z_d^2 - 2zz_d + \rho^2 - 2\rho x\cos\hat{\phi} - 2\rho y\sin\hat{\phi}} + \frac{\omega\rho x\sin\hat{\phi}}{c} - \frac{\omega\rho y\cos\hat{\phi}}{c}}.$$

In (16), the scalar potential φ_d is sought for the remote point P with the radius vector $\mathbf{R} = (x, y, z)$. The vector potential $\mathbf{A}_d$ at this point depends on the velocity $\hat{v}_r = v_r(\hat{t}) = (-\omega\rho\sin\hat{\phi}, \omega\rho\cos\hat{\phi}, 0)$ of motion of the charged particles of the rotating disk at the early time $\hat{t}$. The velocity $\hat{\mathbf{v}}_r$ lies in a plane parallel to the plane XOY and the same holds true for $\mathbf{A}_d$. For the components $\mathbf{A}_d$, we can write the following:

$$A_{dx} = -\frac{\mu_0 \omega s \rho_0 q}{4\pi} \int_0^{2\pi} \int_0^{\rho_d} \frac{\gamma' \sin\hat{\phi}\, \rho^2\, d\rho\, d\phi}{\sqrt{R^2+z_d^2-2zz_d+\rho^2-2\rho x\cos\hat{\phi}-2\rho y\sin\hat{\phi}+\frac{\omega\rho x\sin\hat{\phi}}{c}-\frac{\omega\rho y\cos\hat{\phi}}{c}}}.$$

$$A_{dy} = \frac{\mu_0 \omega s \rho_0 q}{4\pi} \int_0^{2\pi} \int_0^{\rho_d} \frac{\gamma' \cos\hat{\phi}\, \rho^2\, d\rho\, d\phi}{\sqrt{R^2+z_d^2-2zz_d+\rho^2-2\rho x\cos\hat{\phi}-2\rho y\sin\hat{\phi}+\frac{\omega\rho x\sin\hat{\phi}}{c}-\frac{\omega\rho y\cos\hat{\phi}}{c}}}.$$

$$A_{dz} = 0. \qquad (18)$$

2.2 Scalar Potential in the Middle Zone

Let us first consider the case when in (17) the conditions $\hat{R}_P >> a$, $\frac{\omega\hat{R}_P}{c} << 1$ are met, which corresponds to the case of sufficiently large distances R from the sphere of radius a to the point P where the scalar potential is sought. As an example, let us assume that the relations of sizes and velocities are given by the relative value of 1%. In this case, the condition of the middle zone at $R \approx \hat{R}_P$ means that $\frac{a}{R} < 0,01$ and $\frac{\omega R}{c} < 0,01$, so that a two-sided inequality $100a < R < \frac{c}{100\omega}$ is obtained for the distance.

Under the above conditions for $\hat{R}_P$, we can assume in (17) that:

$$\cos\hat{\phi} \approx \cos\phi + \frac{\omega\hat{R}_P}{c}\sin\phi,$$
$$\sin\hat{\phi} \approx \sin\phi - \frac{\omega\hat{R}_P}{c}\cos\phi. \qquad (19)$$

Let us square $\hat{R}_P$ in (13), substitute there $\cos\hat{\phi}$ and $\sin\hat{\phi}$ from (19), obtain a quadratic equation to determine $\hat{R}_P$ and write down its solution:

$$\hat{R}_P = -\frac{\omega\rho(x\sin\phi-y\cos\phi)}{c} + \sqrt{R^2+z_d^2-2zz_d+\rho^2-2\rho x\cos\phi-2\rho y\sin\phi+\frac{\omega^2\rho^2(x\sin\phi-y\cos\phi)^2}{c^2}}. \qquad (20)$$

Since the square root in (16) is equal to $\hat{R}_P$ according to (13), we can replace this square root with the expression for $\hat{R}_P$ from (20). Then, using $\sin\hat{\phi}$ and $\cos\hat{\phi}$ from (19) for transformation of (16), we arrive at the expression:

$$\varphi_d = \frac{s\rho_0 q}{4\pi\varepsilon_0} \int_0^{2\pi} \int_0^{\rho_d} \frac{\gamma'\, \rho\, d\rho\, d\phi}{\sqrt{R^2+z_d^2-2zz_d+\rho^2-2\rho x\cos\phi-2\rho y\sin\phi+\frac{\omega^2\rho^2(x\sin\phi-y\cos\phi)^2}{c^2}} - \frac{\omega^2\rho x\hat{R}_P}{c^2}\cos\phi-\frac{\omega^2\rho y\hat{R}_P}{c^2}\sin\phi}. \qquad (21)$$

In (21), we will expand the square root to the third-order terms by the rule $\sqrt{1+\delta} \approx 1+\frac{\delta}{2}-\frac{\delta^2}{8}$:

$$\sqrt{R^2+z_d^2-2zz_d+\rho^2-2\rho x\cos\phi-2\rho y\sin\phi+\frac{\omega^2\rho^2(x\sin\phi-y\cos\phi)^2}{c^2}}$$
$$\approx\sqrt{R^2+z_d^2-2zz_d+\rho^2}\left[\begin{array}{c}1-\frac{\rho x\cos\phi+\rho y\sin\phi}{R^2+z_d^2-2zz_d+\rho^2}+\\ +\frac{\omega^2\rho^2(x\sin\phi-y\cos\phi)^2}{2c^2\left(R^2+z_d^2-2zz_d+\rho^2\right)}-\frac{\rho^2(x\cos\phi+y\sin\phi)^2}{2\left(R^2+z_d^2-2zz_d+\rho^2\right)^2}+\\ +\frac{\omega^2\rho^3(x\sin\phi-y\cos\phi)^2(x\cos\phi+y\sin\phi)}{2c^2\left(R^2+z_d^2-2zz_d+\rho^2\right)^2}\end{array}\right]. \quad (22)$$

Let us substitute (22) into (20):

$$\hat{R}_P\approx\sqrt{R^2+z_d^2-2zz_d+\rho^2}\left[\begin{array}{c}1-\frac{\omega\rho(x\sin\phi-y\cos\phi)}{c\sqrt{R^2+z_d^2-2zz_d+\rho^2}}-\frac{\rho x\cos\phi+\rho y\sin\phi}{R^2+z_d^2-2zz_d+\rho^2}+\\ +\frac{\omega^2\rho^2(x\sin\phi-y\cos\phi)^2}{2c^2\left(R^2+z_d^2-2zz_d+\rho^2\right)}-\frac{\rho^2(x\cos\phi+y\sin\phi)^2}{2\left(R^2+z_d^2-2zz_d+\rho^2\right)^2}+\\ +\frac{\omega^2\rho^3(x\sin\phi-y\cos\phi)^2(x\cos\phi+y\sin\phi)}{2c^2\left(R^2+z_d^2-2zz_d+\rho^2\right)^2}\end{array}\right]. \quad (23)$$

With the help of $\hat{R}_P$ from (23), we will transform the second and third terms in the denominator of (21), leaving only the terms containing c^2 and c^3:

$$-\frac{\omega^2\rho x\hat{R}_P}{c^2}\cos\phi-\frac{\omega^2\rho y\hat{R}_P}{c^2}\sin\phi$$
$$\approx-\sqrt{R^2+z_d^2-2zz_d+\rho^2}\left[\begin{array}{c}\frac{\omega^2\rho\,(x\cos\phi+y\sin\phi)}{c^2}\\ -\frac{\omega^3\rho^2(x\sin\phi-y\cos\phi)(x\cos\phi+y\sin\phi)}{c^3\sqrt{R^2+z_d^2-2zz_d+\rho^2}}\\ -\frac{\omega^2\rho^2\,(x\cos\phi+y\sin\phi)^2}{c^2\left(R^2+z_d^2-2zz_d+\rho^2\right)}\\ -\frac{\omega^2\rho^3(x\cos\phi+y\sin\phi)^3}{2c^2\left(R^2+z_d^2-2zz_d+\rho^2\right)^2}\end{array}\right]. \quad (24)$$

Let us now substitute (22) and (24) into (21) and put $\sqrt{R^2+z_d^2-2zz_d+\rho^2}$ outside the brackets:

$$\varphi_d \approx \frac{s\rho_{0q}}{4\pi\varepsilon_0}\int_0^{2\pi}\int_0^{\rho_d}\frac{1}{\left[\begin{array}{c}1-\frac{\rho(x\cos\phi+y\sin\phi)}{R^2+z_d^2-2zz_d+\rho^2}\\ -\frac{\rho^2(x\cos\phi+y\sin\phi)^2}{2(R^2+z_d^2-2zz_d+\rho^2)^2}\\ -\frac{\omega^2\rho\,(x\cos\phi+y\sin\phi)}{c^2}\\ +\frac{\omega^2\rho^2(x\sin\phi-y\cos\phi)^2}{2c^2(R^2+z_d^2-2zz_d+\rho^2)}\\ +\frac{\omega^2\rho^2\,(x\cos\phi+y\sin\phi)^2}{c^2(R^2+z_d^2-2zz_d+\rho^2)}+\\ +\frac{\omega^2\rho^3(x\cos\phi+y\sin\phi)(x\sin\phi-y\cos\phi)^2}{2\,c^2(R^2+z_d^2-2zz_d+\rho^2)^2}\\ +\frac{\omega^2\rho^3(x\cos\phi+y\sin\phi)^3}{2\,c^2(R^2+z_d^2-2zz_d+\rho^2)^2}\\ +\frac{\omega^3\rho^2(x\sin\phi-y\cos\phi)(x\cos\phi+y\sin\phi)}{c^3\sqrt{R^2+z_d^2-2zz_d+\rho^2}}\end{array}\right]}\frac{\gamma'\,\rho\,d\rho\,d\phi}{\sqrt{R^2+z_d^2-2zz_d+\rho^2}}.$$

In this integral, we will use an approximate expression of the form $\frac{1}{1+\delta}\approx 1-\delta+\delta^2$ for small δ. This gives the following:

$$\varphi_d \approx \frac{s\rho_{0q}}{4\pi\varepsilon_0}\int_0^{2\pi}\int_0^{\rho_d}\frac{D\gamma'\rho\,d\rho\,d\phi}{\sqrt{R^2+z_d^2-2zz_d+\rho^2}}. \quad (25)$$

The quantity D in (25) is given by the expression:

$$\left.\begin{aligned} D \approx 1 &+ \frac{\rho x\cos\phi+\rho y\sin\phi}{R^2+z_d^2-2zz_d+\rho^2} + \frac{3\rho^2(x\cos\phi+y\sin\phi)^2}{2\left(R^2+z_d^2-2zz_d+\rho^2\right)^2} + \frac{\rho^3(x\cos\phi+y\sin\phi)^3}{\left(R^2+z_d^2-2zz_d+\rho^2\right)^3} + \\ &+ \frac{\rho^4(x\cos\phi+y\sin\phi)^4}{4\left(R^2+z_d^2-2zz_d+\rho^2\right)^4} + \frac{\omega^2\rho\,(x\cos\phi+y\sin\phi)}{c^2} - \frac{\omega^2\rho^2\left(x^2+y^2\right)}{2c^2\left(R^2+z_d^2-2zz_d+\rho^2\right)} + \\ &+ \frac{3\omega^2\rho^2\,(x\cos\phi+y\sin\phi)^2}{2c^2\left(R^2+z_d^2-2zz_d+\rho^2\right)} - \frac{3\omega^2\rho^3\left(x^2+y^2\right)(x\cos\phi+y\sin\phi)}{2c^2\left(R^2+z_d^2-2zz_d+\rho^2\right)^2} - \\ &- \frac{2\omega^2\rho^4\left(x^2+y^2\right)(x\cos\phi+y\sin\phi)^2}{c^2\left(R^2+z_d^2-2zz_d+\rho^2\right)^3} + \frac{\omega^2\rho^4(x\cos\phi+y\sin\phi)^2(x\sin\phi-y\cos\phi)^2}{2c^2\left(R^2+z_d^2-2zz_d+\rho^2\right)^3} - \\ &- \frac{\omega^2\rho^5\left(x^2+y^2\right)(x\cos\phi+y\sin\phi)^3}{2c^2\left(R^2+z_d^2-2zz_d+\rho^2\right)^4} - \frac{\omega^3\rho^2(x\sin\phi-y\cos\phi)(x\cos\phi+y\sin\phi)}{c^3\sqrt{R^2+z_d^2-2zz_d+\rho^2}} - \\ &- \frac{2\omega^3\rho^3(x\sin\phi-y\cos\phi)(x\cos\phi+y\sin\phi)^2}{c^3\left(R^2+z_d^2-2zz_d+\rho^2\right)^{3/2}} - \frac{\omega^3\rho^4(x\sin\phi-y\cos\phi)(x\cos\phi+y\sin\phi)^3}{c^3\left(R^2+z_d^2-2zz_d+\rho^2\right)^{5/2}}. \end{aligned}\right\} \quad (26)$$

In (25), only the quantity D depends on the angle ϕ, according to (26). After integration over this angle in (25), the following remains:

$$\varphi_d \approx \frac{s\rho_{0q}}{2\varepsilon_0}\int_0^{\rho_d} \frac{\left[1+\frac{\omega^2\rho^2\left(x^2+y^2\right)}{4c^2\left(R^2+z_d^2-2zz_d+\rho^2\right)}+\frac{3\rho^2\left(x^2+y^2\right)}{4\left(R^2+z_d^2-2zz_d+\rho^2\right)^2}-\frac{15\omega^2\rho^4\left(x^2+y^2\right)^2}{16c^2\left(R^2+z_d^2-2zz_d+\rho^2\right)^3}+\frac{3\rho^4\left(x^2+y^2\right)^2}{32\left(R^2+z_d^2-2zz_d+\rho^2\right)^4}\right]\gamma'\rho\,d\rho}{\sqrt{R^2+z_d^2-2zz_d+\rho^2}}.$$

The last two terms in the square brackets inside the integral, due to their smallness, can be further neglected. The Lorentz factor γ', similarly to (5), is written in the first approximation as follows:

$$\gamma' = \frac{c\gamma_c}{r\sqrt{4\pi\eta\rho_0}}\sin\left(\frac{r}{c}\sqrt{4\pi\eta\rho_0}\right) \approx \gamma_c - \frac{2\pi\eta\rho_0 r^2\gamma_c}{3c^2} = \gamma_c - \frac{2\pi\eta\rho_0\left(\rho^2+z_d^2\right)\gamma_c}{3c^2}, \quad (27)$$

We will note that here we use the Lorentz factor γ_c at the center of the rotating sphere, which may not be equal to γ_c' in (5) at the center of the sphere at rest. In view of γ' from (27), we can write for φ_d the following:

$$\varphi_d \approx \frac{s\rho_{0q}\gamma_c}{2\varepsilon_0}\int_0^{\rho_d} \frac{\left[1-\frac{2\pi\eta\rho_0\left(\rho^2+z_d^2\right)}{3c^2}+\frac{\omega^2\rho^2\left(x^2+y^2\right)}{4c^2\left(R^2+z_d^2-2zz_d+\rho^2\right)}+\frac{3\rho^2\left(x^2+y^2\right)}{4\left(R^2+z_d^2-2zz_d+\rho^2\right)^2}\right]\rho\,d\rho}{\sqrt{R^2+z_d^2-2zz_d+\rho^2}}.$$

We will represent the potential as the sum of four terms, obtained by integrating the potential φ_d over the variable ρ:

$$\varphi_d \approx \frac{s\rho_{0q}\gamma_c}{2\varepsilon_0}\left(I_1+I_2+I_3+I_4\right),$$

where

$$I_1 = \int_0^{\rho_d} \frac{\rho\,d\rho}{\sqrt{R^2+z_d^2-2zz_d+\rho^2}},$$

$$I_2 = -\frac{2\pi\eta\rho_0}{3c^2}\int_0^{\rho_d} \frac{\left(\rho^2+z_d^2\right)\rho\,d\rho}{\sqrt{R^2+z_d^2-2zz_d+\rho^2}},$$

$$I_3=\frac{\omega^2\left(x^2+y^2\right)}{4c^2}\int\limits_0^{\rho_d}\frac{\rho^3\,d\rho}{\left(R^2+z_d^2-2zz_d+\rho^2\right)^{3/2}},$$

$$I_4=\frac{3\left(x^2+y^2\right)}{4}\int\limits_0^{\rho_d}\frac{\rho^3\,d\rho}{\left(R^2+z_d^2-2zz_d+\rho^2\right)^{5/2}}.$$

These integrals, taking into account the relation $\rho_d^2=a^2-z_d^2$, equal:

$$I_1=\sqrt{R^2+a^2-2zz_d}-\sqrt{R^2+z_d^2-2zz_d}.$$

$$I_2=-\frac{2\pi\eta\rho_0}{3c^2}\left[\frac{(R^2+a^2-2zz_d)^{3/2}}{3}-\left(R^2+z_d^2-2zz_d\right)\sqrt{R^2+a^2-2zz_d}+\right.$$
$$\left.+\frac{2\left(R^2+z_d^2-2zz_d\right)^{3/2}}{3}\right]$$
$$-\frac{2\pi\eta\rho_0 z_d^2}{3c^2}\left(\sqrt{R^2+a^2-2zz_d}-\sqrt{R^2+z_d^2-2zz_d}\right).$$

$$I_3=\frac{\omega^2\left(x^2+y^2\right)}{4c^2}\left[\sqrt{R^2+a^2-2zz_d}+\frac{R^2+z_d^2-2zz_d}{\sqrt{R^2+a^2-2zz_d}}-2\sqrt{R^2+z_d^2-2zz_d}\right].$$

$$I_4=-\frac{\left(x^2+y^2\right)}{4}\left[\frac{a^2-z_d^2}{(R^2+a^2-2zz_d)^{3/2}}+\frac{2}{\sqrt{R^2+a^2-2zz_d}}-\frac{2}{\sqrt{R^2+z_d^2-2zz_d}}\right].$$

(28)

The potential φ_d is the potential at the remote point P from one thin layer in the form of a disk, which is parallel to the plane XOY and shifted along the axis OZ by distance z_d. Now, it is necessary to sum up separate potentials created at the point P by all layers of the ball, taking into account that the layer thickness s is the differential dz_d. Passing from the sum to the integral, we find:

$$\varphi\approx\frac{\rho_{0q}\gamma_c}{2\varepsilon_0}\int\limits_{-a}^{a}\left(I_1+I_2+I_3+I_4\right)dz_d.$$

Using (28), we have the following:

$$\int\limits_{-a}^{a}I_1\,dz_d\approx\frac{2a^3}{3R},\ \int\limits_{-a}^{a}I_2\,dz_d\approx-\frac{4\pi\eta\rho_0a^5}{15c^2R},$$

$$\int\limits_{-a}^{a}I_3\,dz_d\approx\frac{\omega^2a^5\left(x^2+y^2\right)}{15c^2R^3},$$

$$\int\limits_{-a}^{a}I_4\,dz_d\approx\frac{a^5\left(x^2+y^2\right)}{5R^5}.$$

Taking this into account, the following is obtained for the potential:

$$\varphi\approx\frac{\rho_{0q}a^3\gamma_c}{3\varepsilon_0R}\left[1-\frac{2\pi\eta\rho_0a^2}{5c^2}+\frac{3a^2\left(x^2+y^2\right)}{10R^4}+\right.$$
$$\left.\frac{\omega^2a^2\left(x^2+y^2\right)}{10c^2R^2}\right].\qquad(29)$$

Expression (29) for the potential is an approximate solution in the middle zone, where the conditions $R>>a$, $\frac{\omega\hat{R}_P}{c}\approx\frac{\omega R_P}{c}\approx\frac{\omega R}{c}<<1$ are met.

Let us now calculate the charge of a slowly rotating sphere in spherical coordinates r,θ,ϕ. According to (9), the averaged Lorentz factor of the particles' motion is $\overline{\gamma}=\gamma'\gamma_r$, the charge density inside the sphere is $\gamma'\gamma_r\rho_{0q}$ and the element of volume moving due to rotation is $dV_s=\frac{r^2drd\phi\sin\theta d\theta}{\gamma_r}$. Hence, in view of (27), we find for the charge by integrating over the sphere's volume in spherical coordinates:

$$q_\omega=\rho_{0q}\int\gamma'\gamma_r\,dV_s=$$
$$\frac{c\,\rho_{0q}\gamma_c}{\sqrt{4\pi\eta\rho_0}}\int\sin\left(\frac{r}{c}\sqrt{4\pi\eta\rho_0}\right)r\,drd\phi\sin\theta d\theta.\qquad(30)$$

The integration result is as follows:

$$q_\omega = \frac{\rho_{0q} c^2 \gamma_c}{\eta \rho_0}\left[\frac{c}{\sqrt{4\pi\eta\rho_0}}\sin\left(\frac{a}{c}\sqrt{4\pi\eta\rho_0}\right) - a\cos\left(\frac{a}{c}\sqrt{4\pi\eta\rho_0}\right)\right] \approx \frac{4\pi\rho_{0q}a^3\gamma_c}{3}\left(1-\frac{2\pi\eta\rho_0 a^2}{5c^2}\right). \quad (31)$$

According to the method of calculation in (31), the charge q_ω is the sum of invariant charges of all the system's particles and therefore, is an invariant quantity that does not depend on the angular velocity of rotation ω. In this case, the charge q_ω (31) must be equal to the charge q_b in (8). Hence, we find the equality of the Lorentz factors at the center of the sphere for the cases of a sphere at rest and a similar rotating sphere: $\gamma_c = \gamma_c'$.

From (29) and (31), it follows:

$$\varphi \approx \frac{q_\omega}{4\pi\varepsilon_0 R}\left[1+\frac{3a^2(x^2+y^2)}{10R^4}+\frac{\omega^2 a^2(x^2+y^2)}{10c^2R^2}\right]. \quad (32)$$

In order to check the solution of (32) for the potential, we can substitute it in (10) into the equation $\Delta\varphi = \frac{\partial^2\varphi}{\partial x^2}+\frac{\partial^2\varphi}{\partial y^2}+\frac{\partial^2\varphi}{\partial z^2}=0$. As a consequence, it appears that in (32), the sum of the two terms $\frac{3a^2\left(x^2+y^2\right)}{10R^4}+\frac{\omega^2a^2\left(x^2+y^2\right)}{10c^2R^2}$ does not agree with this equation. This is possible, because during integration, we neglected all the possible small terms, the presence of which could lead to satisfying the Laplace equation $\Delta\varphi=0$. In this regard, we will remind that in (17), we expanded the sine and cosine only to the first-order terms in the form $\sin\left(\omega\hat{R}_P/c\right)\approx\omega\hat{R}_P/c$, $\cos\left(\omega\hat{R}_P/c\right)\approx 1$, obtaining (19). But in (32), the angular velocity ω is present in the second-order term containing the square of the speed of light in the denominator. This term can change if in (17) we expand the sine and cosine to the second-order terms in the form $\sin\left(\frac{\omega\hat{R}_P}{c}\right)\approx\frac{\omega\hat{R}_P}{c}-\frac{\omega^3\hat{R}_P^3}{6c^3}$, $\cos\left(\frac{\omega\hat{R}_P}{c}\right)\approx 1-\frac{\omega^2\hat{R}_P^2}{2c^2}$. On the other hand, the presence of the small term $\frac{3a^2\left(x^2+y^2\right)}{10R^4}$ contradicts the Coulomb law at $\omega=0$ and its very appearance may be a consequence of the adopted approximation procedure.

For the Laplace equation to hold, we will substitute the sum of the two terms in (32) with $\frac{\omega^2a^2}{10c^2}$. At least, such substitution is quite acceptable under the conditions $R>>a$, $x^2+y^2>>z^2$, $x^2+y^2\approx R^2$. In view of the above, the potential takes the following form:

$$\varphi \approx \frac{q_\omega}{4\pi\varepsilon_0 R}\left(1+\frac{\omega^2a^2}{10c^2}\right). \quad (33)$$

It follows from the above that in the general case, the potential outside the rotating sphere can be represented by the formula:

$$\varphi = \frac{q_\omega}{4\pi\varepsilon_0 R}F, \quad (34)$$

where the function F can be a function of ω, a, R and of x^2+y^2. At $\omega=0$, it must be $F=1$ and in case of rotation of the sphere with charged particles, for the middle zone, where the conditions $R>>a$, $\frac{\omega R}{c}<<1$, $x^2+y^2\approx R^2$ are met, we must have $F\approx 1+\frac{\omega^2a^2}{10c^2}$ if we consider (33) true. Thus, the function F differs a little from 1.

It follows from expression (32) that in the middle zone, the potential actually can depend on the direction to the observation point and at the same distance R, it increases as it gets closer to the equatorial plane. This could be a consequence of the spherical-cylindrical symmetry of arrangement of the moving charges when the potential is calculated. Indeed, according to (16), the potential φ_d from one disk inside the sphere depends on the retarded angle $\hat{\phi}=\omega\hat{t}+\phi_0=\omega t+\phi_0-\frac{\omega\hat{R}_P}{c}=\phi-\frac{\omega\hat{R}_P}{c}$, which is a function of the angular velocity ω. This implies the dependence of the potential φ outside the sphere on ω, which can be realized in the form of (32-34).

2.3 Vector Potential in the Middle Zone

Proceeding in the same way as when we obtained (25) from (16), we will transform the components of the vector potential of the rotating disk (18):

$$A_{dx} = -\frac{\mu_0 \omega s \rho_{0q}}{4\pi} \int_0^{2\pi} \int_0^{\rho_d} \frac{D\gamma' \sin\hat{\phi}\, \rho^2 d\rho d\phi}{\sqrt{R^2 + z_d^2 - 2zz_d + \rho^2}},$$

$$A_{dy} \approx \frac{\mu_0 \omega s \rho_{0q}}{4\pi} \int_0^{2\pi} \int_0^{\rho_d} \frac{D\gamma' \cos\hat{\phi}\, \rho^2 d\rho d\phi}{\sqrt{R^2 + z_d^2 - 2zz_d + \rho^2}},$$

$$A_{dz} = 0. \qquad (35)$$

Substitution of $\hat{R}_P$ from (23) into (19) gives the following:

$$\cos\hat{\phi} \approx \cos\phi + \frac{\omega}{c}\sqrt{R^2 + z_d^2 - 2zz_d + \rho^2}\sin\phi - \frac{\omega^2 \rho (x\sin\phi - y\cos\phi)\sin\phi}{c^2}$$
$$- \frac{\omega\rho(x\cos\phi + y\sin\phi)\sin\phi}{c\sqrt{R^2 + z_d^2 - 2zz_d + \rho^2}} + \frac{\omega^3 \rho^2 (x\sin\phi - y\cos\phi)^2 \sin\phi}{2c^3\sqrt{R^2 + z_d^2 - 2zz_d + \rho^2}}$$
$$- \frac{\omega\rho^2 (x\cos\phi + y\sin\phi)^2 \sin\phi}{2c(R^2 + z_d^2 - 2zz_d + \rho^2)^{3/2}} + \frac{\omega^3 \rho^3 (x\sin\phi - y\cos\phi)^2 (x\cos\phi + y\sin\phi)\sin\phi}{2c^3 (R^2 + z_d^2 - 2zz_d + \rho^2)^{3/2}}.$$

$$\sin\hat{\phi} \approx \sin\phi - \frac{\omega}{c}\sqrt{R^2 + z_d^2 - 2zz_d + \rho^2}\cos\phi + \frac{\omega^2 \rho (x\sin\phi - y\cos\phi)\cos\phi}{c^2}$$
$$+ \frac{\omega\rho(x\cos\phi + y\sin\phi)\cos\phi}{c\sqrt{R^2 + z_d^2 - 2zz_d + \rho^2}} - \frac{\omega^3 \rho^2 (x\sin\phi - y\cos\phi)^2 \cos\phi}{2c^3\sqrt{R^2 + z_d^2 - 2zz_d + \rho^2}}$$
$$+ \frac{\omega\rho^2 (x\cos\phi + y\sin\phi)^2 \cos\phi}{2c(R^2 + z_d^2 - 2zz_d + \rho^2)^{3/2}} - \frac{\omega^3 \rho^3 (x\sin\phi - y\cos\phi)^2 (x\cos\phi + y\sin\phi)\cos\phi}{2c^3 (R^2 + z_d^2 - 2zz_d + \rho^2)^{3/2}}. \qquad (36)$$

We will use D from (26), as well as $\cos\hat{\phi}$ and $\sin\hat{\phi}$ from (36) and will integrate the products of these quantities over the angle ϕ:

$$\int_0^{2\pi} D\sin\hat{\phi}\, d\phi \approx \frac{\rho y\pi}{R^2 + z_d^2 - 2zz_d + \rho^2} + \frac{3\rho^3 y(x^2 + y^2)\pi}{4(R^2 + z_d^2 - 2zz_d + \rho^2)^3} + \frac{3\omega\rho^3 x(x^2 + y^2)\pi}{4c(R^2 + z_d^2 - 2zz_d + \rho^2)^{5/2}}$$
$$- \frac{15\omega^2 \rho^3 y(x^2 + y^2)\pi}{8c^2 (R^2 + z_d^2 - 2zz_d + \rho^2)^2} - \frac{\omega^3 \rho\, x\pi}{c^3}\sqrt{R^2 + z_d^2 - 2zz_d + \rho^2} + \frac{7\omega^3 \rho^3\, x(x^2 + y^2)\pi}{4c^3 (R^2 + z_d^2 - 2zz_d + \rho^2)^{3/2}}.$$

$$\int_0^{2\pi} D\cos\hat{\phi}\, d\phi \approx \frac{\rho x\pi}{R^2 + z_d^2 - 2zz_d + \rho^2} + \frac{3\rho^3 x(x^2 + y^2)\pi}{4(R^2 + z_d^2 - 2zz_d + \rho^2)^3} - \frac{3\omega\rho^3 y(x^2 + y^2)\pi}{4c(R^2 + z_d^2 - 2zz_d + \rho^2)^{5/2}}$$
$$- \frac{15\omega^2 \rho^3 x(x^2 + y^2)\pi}{8c^2 (R^2 + z_d^2 - 2zz_d + \rho^2)^2} + \frac{\omega^3 \rho y\pi}{c^3}\sqrt{R^2 + z_d^2 - 2zz_d + \rho^2} - \frac{7\omega^3 \rho^3\, y(x^2 + y^2)\pi}{4c^3 (R^2 + z_d^2 - 2zz_d + \rho^2)^{3/2}}. \qquad (37)$$

From (35) and (37), it follows:

$$A_{dx} \approx -\frac{\mu_0 \omega s \rho_{0q} x}{4} \int_0^{\rho_d} \left[\frac{3\omega\rho^2(x^2+y^2)}{4c(R^2+z_d^2-2zz_d+\rho^2)^3} - \frac{\omega^3}{c^3} + \frac{7\omega^3\rho^2(x^2+y^2)}{4c^3(R^2+z_d^2-2zz_d+\rho^2)^2} \right] \gamma' \rho^3 d\rho$$

$$-\frac{\mu_0 \omega s \rho_{0q} y}{4} \int_0^{\rho_d} \left[1 + \frac{3\rho^2(x^2+y^2)}{4(R^2+z_d^2-2zz_d+\rho^2)^2} - \frac{15\omega^2\rho^2(x^2+y^2)}{8c^2(R^2+z_d^2-2zz_d+\rho^2)} \right] \frac{\gamma' \rho^3 d\rho}{(R^2+z_d^2-2zz_d+\rho^2)^{3/2}}.$$

$$A_{dy} \approx -\frac{\mu_0 \omega s \rho_{0q} y}{4} \int_0^{\rho_d} \left[\frac{3\omega\rho^2(x^2+y^2)}{4c(R^2+z_d^2-2zz_d+\rho^2)^3} - \frac{\omega^3}{c^3} + \frac{7\omega^3\rho^2(x^2+y^2)}{4c^3(R^2+z_d^2-2zz_d+\rho^2)^2} \right] \gamma' \rho^3 d\rho$$

$$+\frac{\mu_0 \omega s \rho_{0q} x}{4} \int_0^{\rho_d} \left[1 + \frac{3\rho^2(x^2+y^2)}{4(R^2+z_d^2-2zz_d+\rho^2)^2} - \frac{15\omega^2\rho^2(x^2+y^2)}{8c^2(R^2+z_d^2-2zz_d+\rho^2)} \right] \frac{\gamma' \rho^3 d\rho}{(R^2+z_d^2-2zz_d+\rho^2)^{3/2}}. \quad (38)$$

Let us substitute the Lorentz factor γ' from (27) into (38). Next, we will consider the following integrals:

$$I_5 \approx \gamma_c \int_0^{\rho_d} \left[1 - \frac{2\pi\eta\rho_0(\rho^2+z_d^2)}{3c^2} \right] \left[\frac{3\omega\rho^2(x^2+y^2)}{4c(R^2+z_d^2-2zz_d+\rho^2)^3} - \frac{\omega^3}{c^3} + \frac{7\omega^3\rho^2(x^2+y^2)}{4c^3(R^2+z_d^2-2zz_d+\rho^2)^2} \right] \rho^3 d\rho.$$

$$I_6 \approx \gamma_c \int_0^{\rho_d} \left[1 - \frac{2\pi\eta\rho_0(\rho^2+z_d^2)}{3c^2} + \frac{3\rho^2(x^2+y^2)}{4(R^2+z_d^2-2zz_d+\rho^2)^2} - \frac{15\omega^2\rho^2(x^2+y^2)}{8c^2(R^2+z_d^2-2zz_d+\rho^2)} \right] \frac{\rho^3 d\rho}{(R^2+z_d^2-2zz_d+\rho^2)^{3/2}}. \quad (39)$$

With the help of (39), expressions (38) are written as follows:

$$A_{dx} \approx -\frac{\mu_0 \omega s \rho_{0q} x}{4} I_5 - \frac{\mu_0 \omega s \rho_{0q} y}{4} I_6,$$

$$A_{dy} \approx -\frac{\mu_0 \omega s \rho_{0q} y}{4} I_5 + \frac{\mu_0 \omega s \rho_{0q} x}{4} I_6. \quad (40)$$

After integrating the integrals (39) over the variable ρ, in view of the relation $\rho_d = \sqrt{a^2 - z_d^2}$, we obtain:

$$I_5 \approx \gamma_c \left(1 - \frac{2\pi\eta\rho_0 z_d^2}{3c^2} \right) D_1 - \frac{2\pi\eta\rho_0\gamma_c}{3c^2} D_2,$$

where

$$D_1 = \int_0^{\rho_d} \left[\frac{3\omega\rho^2(x^2+y^2)}{4c(R^2+z_d^2-2zz_d+\rho^2)^3} - \frac{\omega^3}{c^3} + \frac{7\omega^3\rho^2(x^2+y^2)}{4c^3(R^2+z_d^2-2zz_d+\rho^2)^2} \right] \rho^3 d\rho.$$

$$D_2 = \int_0^{\rho_d} \left[\frac{3\omega\rho^2(x^2+y^2)}{4c(R^2+z_d^2-2zz_d+\rho^2)^3} - \frac{\omega^3}{c^3} + \frac{7\omega^3\rho^2(x^2+y^2)}{4c^3(R^2+z_d^2-2zz_d+\rho^2)^2} \right] \rho^5 d\rho.$$

Besides

$$D_1 \approx \frac{3\omega(x^2+y^2)}{4c(R^2+z_d^2-2zz_d)^3}\left[\begin{array}{c}\frac{\left(a^2-z_d^2\right)^3}{6}-\frac{3\left(a^2-z_d^2\right)^4}{8(R^2+z_d^2-2zz_d)}\\ +\frac{3\left(a^2-z_d^2\right)^5}{5(R^2+z_d^2-2zz_d)^2}\end{array}\right]$$

$$-\frac{\omega^3}{c^3}\frac{\left(a^2-z_d^2\right)^2}{4}+\frac{7\omega^3(x^2+y^2)}{4c^3(R^2+z_d^2-2zz_d)^2}\left[\begin{array}{c}\frac{\left(a^2-z_d^2\right)^3}{6}-\frac{\left(a^2-z_d^2\right)^4}{4(R^2+z_d^2-2zz_d)}\\ +\frac{3\left(a^2-z_d^2\right)^5}{10(R^2+z_d^2-2zz_d)^2}\end{array}\right].$$

$$D_2 \approx \frac{3\omega(x^2+y^2)}{4c(R^2+z_d^2-2zz_d)^3}\left[\begin{array}{c}\frac{\left(a^2-z_d^2\right)^4}{8}-\frac{3\left(a^2-z_d^2\right)^5}{10(R^2+z_d^2-2zz_d)}\\ +\frac{\left(a^2-z_d^2\right)^6}{2(R^2+z_d^2-2zz_d)^2}\end{array}\right]$$

$$-\frac{\omega^3}{c^3}\frac{\left(a^2-z_d^2\right)^3}{4}+\frac{7\omega^3(x^2+y^2)}{4c^3(R^2+z_d^2-2zz_d)^2}\left[\begin{array}{c}\frac{\left(a^2-z_d^2\right)^4}{8}-\frac{\left(a^2-z_d^2\right)^5}{5(R^2+z_d^2-2zz_d)}\\ +\frac{\left(a^2-z_d^2\right)^6}{4(R^2+z_d^2-2zz_d)^2}\end{array}\right].$$

(41)

In addition, we have where

$I_6 = D_3 + D_4 + D_5 + D_6$,

$$D_3 = \left(\gamma_c - \frac{2\pi\eta\rho_0 z_d^2\gamma_c}{3c^2}\right)\int_0^{\rho_d}\frac{\rho^3\,d\rho}{(R^2+z_d^2-2zz_d+\rho^2)^{3/2}}$$

$$=\left(\gamma_c - \frac{2\pi\eta\rho_0 z_d^2\gamma_c}{3c^2}\right)\left(\sqrt{R^2+a^2-2zz_d}+\frac{R^2+z_d^2-2zz_d}{\sqrt{R^2+a^2-2zz_d}}-2\sqrt{R^2+z_d^2-2zz_d}\right).$$

$$D_4 = -\frac{2\pi\eta\rho_0\gamma_c}{3c^2}\int_0^{\rho_d}\frac{\rho^5\,d\rho}{(R^2+z_d^2-2zz_d+\rho^2)^{3/2}}$$

$$=-\frac{2\pi\eta\rho_0\gamma_c}{3c^2}\left[\begin{array}{c}\frac{(R^2+a^2-2zz_d)^{3/2}}{3}+\frac{8\left(R^2+z_d^2-2zz_d\right)^{3/2}}{3}-\\ -2\left(R^2+z_d^2-2zz_d\right)\sqrt{R^2+a^2-2zz_d}-\frac{\left(R^2+z_d^2-2zz_d\right)^2}{\sqrt{R^2+a^2-2zz_d}}\end{array}\right].$$

$$D_5 = \frac{3(x^2+y^2)\gamma_c}{4}\int_0^{\rho_d}\frac{\rho^5\,d\rho}{(R^2+z_d^2-2zz_d+\rho^2)^{7/2}}$$

$$= \frac{3(x^2+y^2)\gamma_c}{4}\left[\begin{array}{l}-\dfrac{1}{\sqrt{R^2+a^2-2zz_d}}+\dfrac{8}{15\sqrt{R^2+z_d^2-2zz_d}}+\dfrac{2\left(R^2+z_d^2-2zz_d\right)}{3(R^2+a^2-2zz_d)^{3/2}}-\\ \qquad -\dfrac{\left(R^2+z_d^2-2zz_d\right)^2}{5(R^2+a^2-2zz_d)^{5/2}}\end{array}\right].$$

$$D_6 = -\frac{15\omega^2(x^2+y^2)\gamma_c}{8c^2}\int_0^{\rho_d}\frac{\rho^5\,d\rho}{(R^2+z_d^2-2zz_d+\rho^2)^{5/2}}$$

$$= -\frac{15\omega^2(x^2+y^2)\gamma_c}{8c^2}\left[\begin{array}{l}\sqrt{R^2+a^2-2zz_d}+\dfrac{2\left(R^2+z_d^2-2zz_d\right)}{\sqrt{R^2+a^2-2zz_d}}-\\ -\dfrac{8\sqrt{R^2+z_d^2-2zz_d}}{3}-\dfrac{\left(R^2+z_d^2-2zz_d\right)^2}{3(R^2+a^2-2zz_d)^{3/2}}\end{array}\right].$$

(42)

Substituting in (40) s with the differential dz_d and integrating over all the disks inside the sphere between $-a$ and a, we arrive at the components A_x and A_y of the vector potential from the entire sphere:

$$A_x \approx -\frac{\mu_0\omega\rho_{0q}x}{4}\int_{-a}^{a} I_5\,dz_d - \frac{\mu_0\omega\rho_{0q}y}{4}\int_{-a}^{a} I_6\,dz_d.$$

$$A_y \approx -\frac{\mu_0\omega\rho_{0q}y}{4}\int_{-a}^{a} I_5\,dz_d + \frac{\mu_0\omega\rho_{0q}x}{4}\int_{-a}^{a} I_6\,dz_d.$$

Here, we will take into account that the integrals I_5 and I_6 in (39) are calculated using the quantities D_1, D_2, D_3, D_4, D_5 and D_6 from (41-42):

$$A_x \approx -\frac{\mu_0\omega\rho_{0q}x\gamma_c}{4}\int_{-a}^{a}\left(1-\frac{2\pi\eta\rho_0 z_d^2}{3c^2}\right)D_1\,dz_d + \frac{\pi\mu_0\eta\rho_0\omega\rho_{0q}x\gamma_c}{6c^2}\int_{-a}^{a}D_2\,dz_d$$
$$-\frac{\mu_0\omega\rho_{0q}y}{4}\int_{-a}^{a}(D_3+D_4+D_5+D_6)\,dz_d.$$

$$A_y \approx -\frac{\mu_0\omega\rho_{0q}y\gamma_c}{4}\int_{-a}^{a}\left(1-\frac{2\pi\eta\rho_0 z_d^2}{3c^2}\right)D_1\,dz_d + \frac{\pi\mu_0\eta\rho_0\omega\rho_{0q}y\gamma_c}{6c^2}\int_{-a}^{a}D_2\,dz_d$$
$$+\frac{\mu_0\omega\rho_{0q}x}{4}\int_{-a}^{a}(D_3+D_4+D_5+D_6)\,dz_d.$$

(43)

The integrals of the quantities $\left(1-\frac{2\pi\eta\rho_0 z_d^2}{3c^2}\right)D_1$, D_2, D_3, D_4, D_5 and D_6 over the variable z_d are weakly dependent on z and in the first approximation are equal to:

$$\int_{-a}^{a}\left(1-\frac{2\pi\eta\rho_0 z_d^2}{3c^2}\right)D_1\,dz_d\approx$$

$$\frac{4\omega a^7(x^2+y^2)}{35cR^6}-\frac{4\omega^3a^5}{15c^3}+\frac{4\omega^3a^7(x^2+y^2)}{15c^3R^4}-\frac{8\pi\eta\omega\rho_0a^9(x^2+y^2)}{945c^3R^6}.$$

$$\int_{-a}^{a}D_2\,dz_d\approx\frac{8\omega a^9(x^2+y^2)}{105cR^6}-\frac{8\omega^3a^7}{35c^3}+\frac{8\omega^3a^9(x^2+y^2)}{45c^3R^4}.$$

$$\int_{-a}^{a}D_3\,dz_d\approx\frac{4a^5\gamma_c}{15R^3}-\frac{8\pi\eta\rho_0a^7\gamma_c}{315c^2R^3},\qquad \int_{-a}^{a}D_5\,dz_d\approx\frac{4a^7\left(x^2+y^2\right)\gamma_c}{35R^7},$$

$$\int_{-a}^{a}D_4\,dz_d\approx-\frac{32\pi\eta\rho_0a^7\gamma_c}{315c^2R^3}.\qquad \int_{-a}^{a}D_6\,dz_d\approx-\frac{2\omega^2a^7\left(x^2+y^2\right)\gamma_c}{7c^2R^5}.$$

Substituting these integrals into (43), we find:

$$A_x\approx-\frac{\mu_0\omega^2\rho_{0q}a^3x\gamma_c}{5c}\left[\frac{a^4(x^2+y^2)}{7R^6}-\frac{\omega^2a^2}{3c^2}+\frac{\omega^2a^4(x^2+y^2)}{3c^2R^4}-\frac{2\pi\eta\rho_0a^6(x^2+y^2)}{27c^2R^6}\right]-$$
$$-\frac{\mu_0\omega\rho_{0q}a^5y\gamma_c}{15R^3}\left[1-\frac{10\pi\eta\rho_0a^2}{21c^2}+\frac{3a^2(x^2+y^2)}{7R^4}-\frac{15\omega^2a^2(x^2+y^2)}{14c^2R^2}\right].$$

$$A_y\approx-\frac{\mu_0\omega^2\rho_{0q}a^3y\gamma_c}{5c}\left[\frac{a^4(x^2+y^2)}{7R^6}-\frac{\omega^2a^2}{3c^2}+\frac{\omega^2a^4(x^2+y^2)}{3c^2R^4}-\frac{2\pi\eta\rho_0a^6(x^2+y^2)}{27c^2R^6}\right]+$$
$$+\frac{\mu_0\omega\rho_{0q}a^5x\gamma_c}{15R^3}\left[1-\frac{10\pi\eta\rho_0a^2}{21c^2}+\frac{3a^2(x^2+y^2)}{7R^4}-\frac{15\omega^2a^2(x^2+y^2)}{14c^2R^2}\right].\qquad(44)$$

In view of the approximate nature of our calculations, we should define more precisely all the terms in (44) by substituting the components A_x and A_y of the vector potential into the Laplace equation (10), which has the form $\Delta\mathbf{A}=0$. For this equation to hold, we need to perform simplification in (44), eliminating the small terms and assuming $\frac{x^2+y^2}{R^2}\approx1$. Previously we used a similar approach, in order to pass on from (32) to expression (33) for the potential. This gives the following expression, which is valid at small z:

$$A_x\approx\frac{\mu_0\omega^4\rho_{0q}a^5x\gamma_c}{15c^3}-\frac{\mu_0\omega\rho_{0q}a^5y\gamma_c}{15R^3}\left(1-\frac{10\pi\eta\rho_0a^2}{21c^2}-\frac{15\omega^2a^2}{14c^2}\right).$$

$$A_y\approx\frac{\mu_0\omega^4\rho_{0q}a^5y\gamma_c}{15c^3}+\frac{\mu_0\omega\rho_{0q}a^5x\gamma_c}{15R^3}\left(1-\frac{10\pi\eta\rho_0a^2}{21c^2}-\frac{15\omega^2a^2}{14c^2}\right).\qquad(45)$$

Since in (35) $A_{dz}=0$ for each rotating disk inside the sphere, the component A_z of the vector potential from the entire rotating sphere with charged particles is also equal to zero.

2.4 Electric and Magnetic Fields in the Middle Zone

The electric field strength $\mathbf{E}$ and the magnetic field induction $\mathbf{B}$ are given by standard formulae:

$$\mathbf{E}=-\nabla\varphi-\frac{\partial\mathbf{A}}{\partial t},\ \mathbf{B}=\nabla\times\mathbf{A}.\qquad(46)$$

Since the sphere rotates at the constant angular velocity ω, the vector potential components in (45) do not depend on time and then the field $\mathbf{E}$ is defined only by the gradient of the scalar potential φ. Let us substitute (33) and (45) into (46) and find the fields $\mathbf{E}$ and $\mathbf{B}$, taking into account that $A_z=0$:

$$\mathbf{E} \approx \frac{q_\omega \mathbf{R}}{4\pi\varepsilon_0 R^3}\left(1+\frac{\omega^2 a^2}{10c^2}\right).$$

$$B_x = \frac{\partial A_z}{\partial y} - \frac{\partial A_y}{\partial z} \approx \frac{\mu_0 \omega \rho_{0q} a^5 x z \gamma_c}{5R^5}\left(1 - \frac{10\pi\eta\rho_0 a^2}{21c^2} - \frac{15\omega^2 a^2}{14c^2}\right).$$

$$B_y = \frac{\partial A_x}{\partial z} - \frac{\partial A_z}{\partial x} \approx \frac{\mu_0 \omega \rho_{0q} a^5 y z \gamma_c}{5R^5}\left(1 - \frac{10\pi\eta\rho_0 a^2}{21c^2} - \frac{15\omega^2 a^2}{14c^2}\right).$$

$$B_z = \frac{\partial A_y}{\partial x} - \frac{\partial A_x}{\partial y} \approx \frac{\mu_0 \omega \rho_{0q} a^5 \gamma_c (2R^2 - 3x^2 - 3y^2)}{15R^5}\left(1 - \frac{10\pi\eta\rho_0 a^2}{21c^2} - \frac{15\omega^2 a^2}{14c^2}\right). \quad (47)$$

Since we simplified (44) and used for the vector potential (45), (47) contains only the dipole component of the magnetic field.

In the special theory of relativity, the wave equations are valid for the electric and magnetic fields [15]:

$$\partial_\beta \partial^\beta \mathbf{E} = \frac{1}{c^2}\frac{\partial^2 \mathbf{E}}{\partial t^2} - \Delta\mathbf{E} = -\frac{1}{\varepsilon_0}\nabla(\gamma\rho_{0q}) - \mu_0\frac{\partial \mathbf{j}}{\partial t},$$

$$\partial_\beta \partial^\beta \mathbf{B} = \frac{1}{c^2}\frac{\partial^2 \mathbf{B}}{\partial t^2} - \Delta\mathbf{B} = \mu_0 \nabla \times \mathbf{j}.$$

Since there are no charges or currents outside the rotating charged sphere, the right-hand side of the wave equations becomes equal to zero. In addition, at the constant velocity of rotation, $\mathbf{E}$ and $\mathbf{B}$ do not depend on time. As a result, the wave equations for the fields turn into Laplace equations:

$$\Delta\mathbf{E} = 0,\ \Delta\mathbf{B} = 0. \quad (48)$$

By directly substituting the components of the electric field $\mathbf{E}$ and the magnetic field $\mathbf{B}$ from (47) into (48), we can make sure that the fields in the middle zone satisfy the Laplace equations.

2.5 Scalar Potential in the Far Zone

As conditions for the far zone, we can consider the conditions $R >> a$, $\frac{\omega \hat{R}_P}{c} \approx 1$.

Since $\hat{\phi} = \phi - \frac{\omega \hat{R}_P}{c}$, in this case, we can write:

$$\cos\hat{\phi} = \cos(\phi - \phi_P),\ \sin\hat{\phi} = \sin(\phi - \phi_P), \quad (49)$$

where, in view of (13), the angle $\phi_P = \frac{\omega \hat{R}_P}{c} = \frac{\omega}{c}\sqrt{\begin{matrix}R^2 + z_d^2 - 2zz_d + \rho^2 \\ -2\rho x\cos\hat{\phi} - 2\rho y\sin\hat{\phi}\end{matrix}} \approx \frac{\omega R}{c}$.

Substitution of (49) into (16) gives the following:

$$\varphi_d = \frac{s\rho_{0q}}{4\pi\varepsilon_0}\int_0^{2\pi}\int_0^{\rho_d} \frac{\gamma' \rho\, d\rho\, d\phi}{\hat{R}_P + \frac{\omega\rho x\sin(\phi-\phi_P)}{c} - \frac{\omega\rho y\cos(\phi-\phi_P)}{c}}. \quad (50)$$

where

$$\hat{R}_P = \sqrt{\begin{matrix}R^2 + z_d^2 - 2zz_d + \rho^2 - 2\rho x\cos(\phi-\phi_P) \\ -2\rho y\sin(\phi-\phi_P)\end{matrix}}.$$

Let us take into account the following transformations for the expression under the integral sign:

$$H = \frac{1}{\hat{R}_P + \frac{\omega\rho x\sin(\phi-\phi_P)}{c} - \frac{\omega\rho y\cos(\phi-\phi_P)}{c}} = \frac{\left(R^2 + z_d^2 - 2zz_d + \rho^2\right)^{-1/2}}{\sqrt{1 - \frac{2\rho\,[x\cos(\phi-\phi_P) + y\sin(\phi-\phi_P)]}{R^2 + z_d^2 - 2zz_d + \rho^2}} + \frac{\omega\rho\,[x\sin(\phi-\phi_P) - y\cos(\phi-\phi_P)]}{c\sqrt{R^2 + z_d^2 - 2zz_d + \rho^2}}}.$$

In this expression, we use the rule for expanding the square root in the form $\sqrt{1-\delta} \approx 1 - \frac{\delta}{2} - \frac{\delta^2}{8}$ and an approximate expression $\frac{1}{1-\frac{\delta}{2}-\frac{\delta^2}{8}+\gamma} \approx 1 + \frac{\delta}{2} + \frac{3\delta^2}{8} - \gamma - \gamma\delta(1+\delta) + \gamma^2$:

$$H \approx \frac{\left(\begin{array}{c} 1+\frac{\rho\,[x\cos(\phi-\phi_P)+y\sin(\phi-\phi_P)]}{R^2+z_d^2-2zz_d+\rho^2}+\frac{3\rho^2\,[x\cos(\phi-\phi_P)+y\sin(\phi-\phi_P)]^2}{2\left(R^2+z_d^2-2zz_d+\rho^2\right)^2}- \\ -\frac{\omega\rho\,[x\sin(\phi-\phi_P)-y\cos(\phi-\phi_P)]}{c\sqrt{R^2+z_d^2-2zz_d+\rho^2}}+\frac{\omega^2\rho^2\,[x\sin(\phi-\phi_P)-y\cos(\phi-\phi_P)]^2}{c^2\left(R^2+z_d^2-2zz_d+\rho^2\right)}- \\ -\frac{2\omega\rho^2\,[x\sin(\phi-\phi_P)-y\cos(\phi-\phi_P)][x\cos(\phi-\phi_P)+y\sin(\phi-\phi_P)]}{c\left(R^2+z_d^2-2zz_d+\rho^2\right)^{3/2}} \end{array} \right)}{\sqrt{R^2+z_d^2-2zz_d+\rho^2}}. \qquad (51)$$

In view of (51), for the potential (50), we can write the following:

$$\varphi_d \approx \frac{s\rho_{0q}}{4\pi\varepsilon_0}\int_0^{2\pi}\int_0^{\rho_d} H\,\gamma'\rho\,d\rho\,d\phi\,. \qquad (52)$$

As the distance R increases, the angle $\phi_P=\frac{\omega\hat{R}_P}{c}\approx\frac{\omega R}{c}$ can first reach the value $\frac{\pi}{2}$, then π, $\frac{3\pi}{2}$, 2π, … etc. In the general case, the angle ϕ_P will pass through the values $\frac{k\pi}{2}$, where $k=1,2,3...$

Let us integrate the quantity H in (52) over the angle ϕ, assuming the angle ϕ_P to be constant and almost independent of ϕ. Taking into account that the integrals of $\cos\left(\phi-\phi_P\right)$, $\sin\left(\phi-\phi_P\right)$ and $\sin\left(\phi-\phi_P\right)\cos\left(\phi-\phi_P\right)$ between the limits of 0 and 2π are equal to zero, we find:

$$\varphi_d \approx \frac{s\rho_{0q}}{2\varepsilon_0}\int_0^{\rho_d}\frac{\left[1+\frac{\omega^2\rho^2\,(x^2+y^2)}{2c^2\left(R^2+z_d^2-2zz_d+\rho^2\right)}+\frac{3\rho^2\,(x^2+y^2)}{4\left(R^2+z_d^2-2zz_d+\rho^2\right)^2}\right]\gamma'\rho\,d\rho}{\sqrt{R^2+z_d^2-2zz_d+\rho^2}}. \qquad (53)$$

If we substitute the expression for γ' from (27) into (53), then we will see that the potential can be represented in the form $\varphi_d \approx \frac{s\rho_{0q}\gamma_c}{2\varepsilon_0}\left(I_1+I_2+2I_3+I_4\right)$, where the integrals I_1, I_2, I_3 and I_4 were found in (28).

The sum of the potentials φ_d of all the sphere's layers gives the sought-for sphere potential. Assuming $s=dz_d$ and substituting the sum of the layers' potentials with the integral over the variable z_d, for the sphere potential we can write:

$$\varphi \approx \frac{\rho_{0q}\gamma_c}{2\varepsilon_0}\int_{-a}^{a}(I_1+I_2+2I_3+2I_4)dz_d \approx \frac{\rho_{0q}a^3\gamma_c}{3\varepsilon_0 R}\left[1-\frac{2\pi\eta\rho_0 a^2}{5c^2}+\frac{3a^2\left(x^2+y^2\right)}{10R^4}+\frac{\omega^2a^2\left(x^2+y^2\right)}{5c^2R^2}\right]. \qquad (54)$$

The scalar potential (54) in the far zone differs from the potential (29) in the middle zone in the fact that in (54), the last term in the square brackets is twice as large.

In (54), we can substitute (31) and express the potential in terms of the charge q_ω. To ensure that the potential corresponds to the Laplace equation, in (54) we will eliminate the small term $\frac{3a^2\left(x^2+y^2\right)}{10R^4}$ and assume that $x^2+y^2\approx R^2$, which is true at small z. As a result, we obtain the following:

$$\varphi \approx \frac{q_\omega}{4\pi\varepsilon_0 R}\left(1+\frac{\omega^2a^2}{5c^2}\right). \qquad (55)$$

We suppose that the small difference between the potentials in (55) and in (33) is associated with the fact that the solutions for these potentials were obtained in two different ways and with different degrees of approximation.

2.6 Vector Potential in the Far Zone

We will transform (18) using (51) in the same way as potential (50) was transformed and we will also take into account (49). Then, for the vector potential components of the rotating disk, we find the following:

$$A_{dx} \approx -\frac{\mu_0 \omega s \rho_{0q}}{4\pi} \int_0^{2\pi} \int_0^{\rho_d} H\gamma' \sin(\phi - \phi_P)\, \rho^2\, d\rho\, d\phi.$$

$$A_{dy} \approx \frac{\mu_0 \omega s \rho_{0q}}{4\pi} \int_0^{2\pi} \int_0^{\rho_d} H\gamma' \cos(\phi - \phi_P)\, \rho^2\, d\rho\, d\phi.$$

At large distances, we may neglect the change in the angle $\phi_P = \frac{\omega \hat{R}_P}{c} \approx \frac{\omega R}{c}$ when integrating over the angle ϕ and consider ϕ_P a constant. This makes it easier to integrate components A_{dx} and A_{dy}. Taking into account the expression for H from (51), we find:

$$A_{dx} \approx \frac{\mu_0 \omega^2 s \rho_{0q} x}{4c} \int_0^{\rho_d} \frac{\gamma' \rho^3 d\rho}{R^2 + z_d^2 - 2zz_d + \rho^2} - \frac{\mu_0 \omega s \rho_{0q} y}{4} \int_0^{\rho_d} \frac{\gamma' \rho^3 d\rho}{(R^2 + z_d^2 - 2zz_d + \rho^2)^{3/2}}.$$

$$A_{dy} \approx \frac{\mu_0 \omega^2 s \rho_{0q} y}{4c} \int_0^{\rho_d} \frac{\gamma' \rho^3 d\rho}{R^2 + z_d^2 - 2zz_d + \rho^2} + \frac{\mu_0 \omega s \rho_{0q} x}{4} \int_0^{\rho_d} \frac{\gamma' \rho^3 d\rho}{(R^2 + z_d^2 - 2zz_d + \rho^2)^{3/2}}. \quad (56)$$

If we substitute the Lorentz factor γ' from (27) into (56), the following integrals appear:

$$I_7 = \gamma_c \int_0^{\rho_d} \left[1 - \frac{2\pi\eta\rho_0(\rho^2 + z_d^2)}{3c^2}\right] \frac{\rho^3 d\rho}{R^2 + z_d^2 - 2zz_d + \rho^2}.$$

$$I_8 = \gamma_c \int_0^{\rho_d} \left[1 - \frac{2\pi\eta\rho_0(\rho^2 + z_d^2)}{3c^2}\right] \frac{\rho^3 d\rho}{(R^2 + z_d^2 - 2zz_d + \rho^2)^{3/2}}.$$

Using the integrals I_7 and I_8, we can write (56) as follows:

$$A_{dx} \approx \frac{\mu_0 \omega^2 s \rho_{0q} x}{4c} I_7 - \frac{\mu_0 \omega s \rho_{0q} y}{4} I_8,$$

$$A_{dy} \approx \frac{\mu_0 \omega^2 s \rho_{0q} y}{4c} I_7 + \frac{\mu_0 \omega s \rho_{0q} x}{4} I_8. \quad (57)$$

Let us calculate the integrals I_7 and I_8 taking into account the relation $\rho_d = \sqrt{a^2 - z_d^2}$, expanding the denominators into series by the rule $\frac{1}{1+\delta} \approx 1 - \delta + \delta^2$, where $\delta = \frac{\rho^2}{R^2 + z_d^2 - 2zz_d}$:

$$I_7 \approx \frac{(a^2 - z_d^2)^2}{4(R^2 + z_d^2 - 2zz_d)} \left(\gamma_c - \frac{2\pi\eta\rho_0 z_d^2 \gamma_c}{3c^2}\right) \left[1 - \frac{2(a^2 - z_d^2)}{3(R^2 + z_d^2 - 2zz_d)} + \frac{(a^2 - z_d^2)^2}{2(R^2 + z_d^2 - 2zz_d)^2}\right] - \frac{\pi\eta\rho_0\gamma_c(a^2 - z_d^2)^3}{9c^2(R^2 + z_d^2 - 2zz_d)} \left[1 - \frac{3(a^2 - z_d^2)}{4(R^2 + z_d^2 - 2zz_d)} + \frac{3(a^2 - z_d^2)^2}{5(R^2 + z_d^2 - 2zz_d)^2}\right].$$

$$I_8 = \left(\gamma_c - \frac{2\pi\eta\rho_0 z_d^2 \gamma_c}{3c^2}\right) \left[\sqrt{R^2 + a^2 - 2zz_d} + \frac{R^2 + z_d^2 - 2zz_d}{\sqrt{R^2 + a^2 - 2zz_d}} - 2\sqrt{R^2 + z_d^2 - 2zz_d}\right] - \frac{2\pi\eta\rho_0\gamma_c}{3c^2} \left[\frac{(R^2 + a^2 - 2zz_d)^{3/2}}{3} - 2(R^2 + z_d^2 - 2zz_d)\sqrt{R^2 + a^2 - 2zz_d} - \frac{(R^2 + z_d^2 - 2zz_d)^2}{\sqrt{R^2 + a^2 - 2zz_d}} + \frac{8(R^2 + z_d^2 - 2zz_d)^{3/2}}{3}\right]. \quad (58)$$

The quantities A_{dx} and A_{dy} are the components of the vector potential from one thin disk. To pass on to the corresponding components of the potential from the entire sphere, in (57) it is necessary to set $s = dz_d$ and integrate over the variable z_d that specifies the position of the disks inside the sphere on the axis OZ:

$$A_x \approx \frac{\mu_0 \omega^2 \rho_{0q} x}{4c} \int\limits_{-a}^{a} I_7 \, dz_d - \frac{\mu_0 \omega \rho_{0q} y}{4} \int\limits_{-a}^{a} I_8 \, dz_d ,$$

$$A_y \approx \frac{\mu_0 \omega^2 \rho_{0q} y}{4c} \int\limits_{-a}^{a} I_7 \, dz_d + \frac{\mu_0 \omega \rho_{0q} x}{4} \int\limits_{-a}^{a} I_8 \, dz_d . \quad (59)$$

Substitution of (58) into (59) and subsequent integration over the variable z_d give the following:

$$A_x \approx \frac{\mu_0 \omega^2 \rho_{0q} a^5 x \gamma_c}{15 c R^2}\left(1 - \frac{10\pi\eta\rho_0 a^2}{21 c^2}\right) - \frac{\mu_0 \omega \rho_{0q} a^5 y \gamma_c}{15 R^3}\left(1 - \frac{10\pi\eta\rho_0 a^2}{21 c^2}\right).$$

$$A_y \approx \frac{\mu_0 \omega^2 \rho_{0q} a^5 y \gamma_c}{15 c R^2}\left(1 - \frac{10\pi\eta\rho_0 a^2}{21 c^2}\right) + \frac{\mu_0 \omega \rho_{0q} a^5 x \gamma_c}{15 R^3}\left(1 - \frac{10\pi\eta\rho_0 a^2}{21 c^2}\right). \quad (60)$$

Here, only the last terms containing R^3 in the denominator exactly satisfy the Laplace equation. As for the first terms, the far zone condition $\frac{\omega R}{c} \approx 1$ can be taken into account in them. This gives the following expressions:

$$A_x \approx \frac{\mu_0 \omega \rho_{0q} a^5 x \gamma_c}{15 R^3}\left(1 - \frac{10\pi\eta\rho_0 a^2}{21 c^2}\right) - \frac{\mu_0 \omega \rho_{0q} a^5 y \gamma_c}{15 R^3}\left(1 - \frac{10\pi\eta\rho_0 a^2}{21 c^2}\right),$$

$$A_y \approx \frac{\mu_0 \omega \rho_{0q} a^5 y \gamma_c}{15 R^3}\left(1 - \frac{10\pi\eta\rho_0 a^2}{21 c^2}\right) + \frac{\mu_0 \omega \rho_{0q} a^5 x \gamma_c}{15 R^3}\left(1 - \frac{10\pi\eta\rho_0 a^2}{21 c^2}\right),$$

that satisfy the Laplace equation. The component $A_z = 0$ and therefore, A_z automatically satisfies the Laplace equation.

2.7 The Electric and Magnetic Fields in the Far Zone

In order to find the fields $\mathbf{E}$ and $\mathbf{B}$, it is necessary to substitute (55) and (60) into (46):

$$\mathbf{E} \approx \frac{q_\omega \mathbf{R}}{4\pi\varepsilon_0 R^3}\left(1 + \frac{\omega^2 a^2}{5c^2}\right).$$

$$B_x = \frac{\partial A_z}{\partial y} - \frac{\partial A_y}{\partial z} \approx \frac{2\mu_0 \omega^2 \rho_{0q} a^5 y z \gamma_c}{15 c R^4}\left(1 - \frac{10\pi\eta\rho_0 a^2}{21 c^2}\right) + \frac{\mu_0 \omega \rho_{0q} a^5 x z \gamma_c}{5 R^5}\left(1 - \frac{10\pi\eta\rho_0 a^2}{21 c^2}\right).$$

$$B_y = \frac{\partial A_x}{\partial z} - \frac{\partial A_z}{\partial x} \approx -\frac{2\mu_0 \omega^2 \rho_{0q} a^5 x z \gamma_c}{15 c R^4}\left(1 - \frac{10\pi\eta\rho_0 a^2}{21 c^2}\right) + \frac{\mu_0 \omega \rho_{0q} a^5 y z \gamma_c}{5 R^5}\left(1 - \frac{10\pi\eta\rho_0 a^2}{21 c^2}\right).$$

$$B_z = \frac{\partial A_y}{\partial x} - \frac{\partial A_x}{\partial y} \approx \frac{\mu_0 \omega \rho_{0q} a^5 \gamma_c (2R^2 - 3x^2 - 3y^2)}{15 R^5}\left(1 - \frac{10\pi\eta\rho_0 a^2}{21 c^2}\right). \quad (61)$$

The fields in (61) differ insignificantly from the fields in (47) in the middle zone due to the small additions proportional to the value $\frac{\omega^2 a^2}{c^2}$. This difference can be considered the consequence of the fact that during calculations, different methods of obtaining an approximate solution were used. In addition, a rotational component of the magnetic field appears in the first terms in B_x and B_y in (61).

2.8 Scalar Potential in the Near Zone

In the near zone, the conditions $R \geq a$, $\frac{\omega \hat{R}_P}{c} << 1$ are met, so that the point P, where the potential is determined, is not far from the sphere. We can start with expression (21) for the potential φ_d, generated by a thin disk-shaped layer inside the sphere, located on the axis OZ at the height z_d. For the near zone, we can assume that the early time point $\hat{t} = t - \frac{\hat{R}_P}{c}$ is approximately equal to $\hat{t} \approx t - \frac{R_P}{c}$. In this case, the quantity R_P in (11) differs a little from $\hat{R}_P$ in (13), since their difference is associated with a small difference between the angle ϕ and the angle $\hat{\phi} = \phi - \frac{\omega \hat{R}_P}{c}$. Therefore, the quantity $\hat{R}_P$ in the denominator in (21) can be substituted with R_P.

The quantity R_P is the distance from the integration point inside the sphere to the observation point P. Further, we will assume that the point P is located outside the sphere and the condition $R_P >> \frac{\omega\rho\left(x\sin\phi - y\cos\phi\right)}{c}$ is met. This allows us to expand the root in (21) so as to distinguish a small term containing the square of the speed of light:

$$\sqrt{R^2+z_d^2-2zz_d+\rho^2-2\rho x\cos\phi-2\rho y\sin\phi+\frac{\omega^2\rho^2(x\sin\phi-y\cos\phi)^2}{c^2}}$$
$$\approx R_P+\frac{\omega^2\rho^2(x\sin\phi-y\cos\phi)^2}{2c^2R_P}.$$

Here, the quantity R_P represents the square root and corresponds to (11):

$$R_P=\sqrt{\begin{matrix}R^2+z_d^2-2zz_d+\rho^2\\-2\rho x\cos\phi-2\rho y\sin\phi\end{matrix}}. \quad (62)$$

Now, the denominator in (21) can be transformed by the rule $\frac{1}{R_P+\delta}\approx\frac{1}{R_P}\left(1-\frac{\delta}{R_P}\right)$. The potential φ_d is generated by one layer in the form of a thin disk of radius $\rho_d=\sqrt{a^2-z_d^2}$. The total potential of the sphere is the sum of the potentials of all the layers and this sum, in view of the equality $s=dz_d$, can be substituted with the integral:

$$\varphi\approx \frac{\rho_0 q}{4\pi\varepsilon_0}\int_{-a}^{a}\int_0^{\rho_d}\int_0^{2\pi}\left[1-\frac{\omega^2\rho^2(x\sin\phi-y\cos\phi)^2}{2c^2R_P^2}+\frac{\omega^2\rho x}{c^2}\cos\phi+\frac{\omega^2\rho y}{c^2}\sin\phi\right]\frac{\gamma'\rho\,d\rho\,d\phi\,dz_d}{R_P}. \quad (63)$$

In (63), the expression in square brackets depends on the angle ϕ, as well as R_P according to (62). When integrating over the angle, we need four integrals:

$$I_9=\int_0^{2\pi}\frac{d\phi}{R_P}=\int_0^{2\pi}\frac{d\phi}{\sqrt{R^2+z_d^2-2zz_d+\rho^2-2\rho x\cos\phi-2\rho y\sin\phi}}.$$

$$I_{10}=\int_0^{2\pi}\frac{(x\sin\phi-y\cos\phi)^2}{\left(R^2+z_d^2-2zz_d+\rho^2-2\rho x\cos\phi-2\rho y\sin\phi\right)^{3/2}}d\phi.$$

$$I_{11}=\int_0^{2\pi}\frac{\cos\phi}{\sqrt{R^2+z_d^2-2zz_d+\rho^2-2\rho x\cos\phi-2\rho y\sin\phi}}d\phi.$$

$$I_{12}=\int_0^{2\pi}\frac{\sin\phi}{\sqrt{R^2+z_d^2-2zz_d+\rho^2-2\rho x\cos\phi-2\rho y\sin\phi}}d\phi. \quad (64)$$

As shown in [16], integrals (64) are expressed in terms of the elliptic integrals $E\left(k,\frac{\pi}{2}\right)$ and $F\left(k,\frac{\pi}{2}\right)$. Taking into account (64), as well as (27) for γ', (63) will be written as follows:

$$\varphi\approx\frac{\rho_0 q\,\gamma_c}{4\pi\varepsilon_0}\int_{-a}^{a}\int_0^{\rho_d}\left\{\left[1-\frac{2\pi\eta\rho_0(\rho^2+z_d^2)}{3c^2}\right]I_9-\frac{\omega^2\rho^2}{2c^2}I_{10}+\frac{\omega^2\rho x}{c^2}I_{11}+\frac{\omega^2\rho y}{c^2}I_{12}\right\}\rho\,d\rho\,dz_d.$$

This expression shows that we need to calculate the integrals $\int_0^{\rho_d}I_9\,\rho\,d\rho$, $\int_0^{\rho_d}I_9\,\rho^3\,d\rho$, $\int_0^{\rho_d}I_{10}\,\rho^3\,d\rho$, $\int_0^{\rho_d}I_{11}\,\rho^2\,d\rho$, $\int_0^{\rho_d}I_{12}\,\rho^2\,d\rho$. To do this, it is necessary to represent the quantities I_9, I_{10}, I_{11} and I_{12} so that the variable ρ appears in them in an explicit form. For this purpose, we will expand the elliptic integrals $E\left(k,\frac{\pi}{2}\right)$ and $F\left(k,\frac{\pi}{2}\right)$ into series by the standard formulae:

$$F\left(k,\frac{\pi}{2}\right)=\frac{\pi}{2}\left(1+\frac{k^2}{4}+\frac{9k^4}{64}\ldots\right)=\frac{\pi}{2}\sum_{n=0}^{\infty}\left(\frac{(2n)!}{2^{2n}n!^2}\right)^2k^{2n}.$$

$$E\left(k,\frac{\pi}{2}\right)=\frac{\pi}{2}\left(1-\frac{k^2}{4}-\frac{3k^4}{64}\ldots\right)=\frac{\pi}{2}\sum_{n=0}^{\infty}\left(\frac{(2n)!}{2^{2n}n!^2}\right)^2\frac{k^{2n}}{1-2n}. \quad (65)$$

In (65), we take into account the first two expansion terms $F\left(k,\frac{\pi}{2}\right)$ and substitute them into I_9 and then substitute three terms of each expansion into I_{10}, I_{11} и I_{12}. The quantities I_{10}, I_{11} and I_{12} are proportional to each other, so that their substitution into the expression for the potential leads to cancellation of the terms:

$$\varphi \approx \frac{\rho_{0q}\gamma_c}{4\pi\varepsilon_0}\int_{-a}^{a}\int_{0}^{\rho_d}\left\{\left[1-\frac{2\pi\eta\rho_0(\rho^2+z_d^2)}{3c^2}\right]I_9+\frac{\omega^2\rho^2}{2c^2}I_{10}\right\}\rho\,d\rho\,dz_d.$$

Now, we can calculate the integrals $H_1=\int_0^{\rho_d} I_9\,\rho\,d\rho$, $H_2=\int_0^{\rho_d} I_9\,\rho^3\,d\rho$ and $H_3=\int_0^{\rho_d} I_{10}\,\rho^3\,d\rho$ and then express the potential in terms of integrals over the variable z_d of the quantities H_1, H_2 and H_3 [16]:

$$\varphi \approx \frac{\rho_{0q}\gamma_c}{4\pi\varepsilon_0}\int_{-a}^{a}H_1\,dz_d+\frac{\omega^2\rho_{0q}\gamma_c}{8\pi c^2\varepsilon_0}\int_{-a}^{a}H_3\,dz_d-\frac{\eta\rho_0\rho_{0q}\gamma_c}{6c^2\varepsilon_0}\int_{-a}^{a}z_d^2H_1\,dz_d-\frac{\eta\rho_0\rho_{0q}\gamma_c}{6c^2\varepsilon_0}\int_{-a}^{a}H_2\,dz_d\ . \quad (66)$$

Due to the cumbersomeness of the expressions for H_1, H_2 and H_3, integration in (66) becomes difficult; besides, the solution is expressed in terms of special functions and cannot be represented in an explicit form without expansion into series. In this regard, we will consider here only three simplest cases.

The first term on the right-hand side of (66), that is, the term $\varphi'=\frac{\rho_{0q}\gamma_c}{4\pi\varepsilon_0}\int_{-a}^{a}H_1\,dz_d$, does not contain the speed of light and does not depend on the angular velocity of rotation ω. In the case of a classical uniform solid body and in the absence of rotation, this term should define the scalar potential in accordance with Coulomb law. Indeed, if we calculate φ' using H_1 on the axis OZ, on condition that $x=y=0$, $z=R$, then we will obtain:

$$H_1(z=R)=2\pi\sqrt{R^2+a^2-2Rz_d}-2\pi(R-z_d).$$

$$\varphi'(z=R)=\frac{\rho_{0q}\gamma_c}{4\pi\varepsilon_0}\int_{-a}^{a}H_1(z=R)\,dz_d=\frac{\rho_{0q}a^3\gamma_c}{3\varepsilon_0 R}. \quad (67)$$

In a solid body, the Lorentz factor at the center of the sphere is $\gamma_c=1$. Taking into account that the electric charge of a uniformly charged solid spherical body is $q=\frac{4\pi\rho_{0q}a^3}{3}$, we have: $\varphi'(z=R)=\frac{q}{4\pi\varepsilon_0 R}$, which corresponds to the Coulomb law on the axis OZ.

In the case of a relativistic uniform system, potential (66) on the axis OZ, on condition that $x=y=0$, $z=R$, will depend only on H_1 and H_2, since H_3 vanishes. Since

$$H_2(z=R)=\frac{2\pi}{3}\left(a^2-2R^2-3z_d^2+4Rz_d\right)\sqrt{R^2+a^2-2Rz_d}+\frac{4\pi}{3}(R-z_d)^3,$$

then, in view of (67) and (31), potential (66) becomes equal to:

$$\varphi(z=R)\approx\frac{\rho_{0q}a^3\gamma_c}{3\varepsilon_0 R}\left(1-\frac{2\pi\eta\rho_0a^2}{5c^2}\right)\approx\frac{q_\omega}{4\pi\varepsilon_0 R}. \quad (68)$$

Determination of the potential on the sphere's surface, where $z=0$, $R=a$, is of particular interest. Using H_1 from [16], we will express $\int_{-a}^{a}H_1\,dz_d$ in (66) in the following form:

$$\int_{-a}^{a}H_1\,dz_d=2\pi I_{13}-2\pi\int_{-a}^{a}\sqrt{R^2+z_d^2-2zz_d}\,dz_d+2\pi I_{14}-2\pi(x^2+y^2)\int_{-a}^{a}\frac{\sqrt{R^2+z_d^2-2zz_d}}{(z-z_d)^2}\,dz_d+2\pi I_{15}+2\pi I_{16}-2\pi I_{17}\ . \quad (69)$$

Here,

$$I_{13} = \int_{-a}^{a} \sqrt{R^2 + a^2 - 2zz_d + 2\sqrt{a^2 - z_d^2}\sqrt{x^2 + y^2}}\, dz_d.$$

$$I_{14} = (x^2 + y^2)^2 \int_{-a}^{a} \frac{dz_d}{(z - z_d)^2 \sqrt{R^2 + a^2 - 2zz_d + 2\sqrt{a^2 - z_d^2}\sqrt{x^2 + y^2}}}.$$

$$I_{15} = (x^2 + y^2)^{3/2} \int_{-a}^{a} \frac{\sqrt{a^2 - z_d^2}}{(z - z_d)^2 \sqrt{R^2 + a^2 - 2zz_d + 2\sqrt{a^2 - z_d^2}\sqrt{x^2 + y^2}}}\, dz_d.$$

$$I_{16} = (x^2 + y^2) \int_{-a}^{a} \frac{1}{\sqrt{R^2 + a^2 - 2zz_d + 2\sqrt{a^2 - z_d^2}\sqrt{x^2 + y^2}}}\, dz_d.$$

$$I_{17} = \sqrt{x^2 + y^2} \int_{-a}^{a} \frac{\sqrt{a^2 - z_d^2}}{\sqrt{R^2 + a^2 - 2zz_d + 2\sqrt{a^2 - z_d^2}\sqrt{x^2 + y^2}}}\, dz_d.$$

When $z = 0$, $R = a$, all the integrals in (69) are taken exactly, without applying elliptic integrals, by using substitution $z_d = a \sin 2\gamma$. In particular, we have:

$$I_{13}(R = a) = \frac{8\sqrt{2}a^2}{3}.$$

$$I_{14}(R = a) = -\frac{a^2}{4} \ln \operatorname{tg}\left(\frac{\pi}{8}\right) - \frac{3\sqrt{2}a^2}{4}.$$

$$I_{15}(R = a) = -\frac{\sqrt{2}a^2}{4} + \frac{5a^2}{4} \ln \operatorname{tg}\left(\frac{\pi}{8}\right).$$

$$I_{16}(R = a) = 2\sqrt{2}a^2 + 2a^2 \ln \operatorname{tg}\left(\frac{\pi}{8}\right).$$

$$I_{17}(R = a) = \frac{2\sqrt{2}a^2}{3} + 2a^2 \ln \operatorname{tg}\left(\frac{\pi}{8}\right). \qquad (70)$$

Substituting (70) into (69), we find:

$$\int_{-a}^{a} H_1(R = a)\, dz_d = 2\pi \left[\frac{16\sqrt{2}a^2}{3} + 5a^2 \ln \operatorname{tg}\left(\frac{\pi}{8}\right) - 3a^2 \ln\left(1 + \sqrt{2}\right)\right] \approx 0{,}98\pi a^2.$$

On the other hand, for the Coulomb law to hold true for a fixed solid body at $z = 0$, $R = a$, in (66), only the first term is taken into account and it must be $\int_{-a}^{a} H_1\, dz_d = \frac{4\pi a^2}{3} \approx 1{,}32\pi a^2$. The obtained above value $0.98\pi a^2$ turns out to be 26% less. The difference arose from the fact that when calculating the integrals I_9 and I_{10}, expansion (65) of complete elliptic integrals was used only up to the second- and third-order terms, respectively. For greater accuracy, an increased number of expansion terms should be used.

Thus, it can be stated that the scalar potential outside the sphere is determined exactly on the axis OZ and in the other directions, we obtain only an approximate estimate, depending on the number of expansion terms used in (65). Nevertheless, since H_1 does not depend on either the speed of light or the angular velocity of rotation ω, this also applies to the potential $\varphi' = \frac{\rho_{0q}\gamma_c}{4\pi\varepsilon_0} \int_{-a}^{a} H_1\, dz_d$ in (66). This means that the value of the potential φ' in an arbitrary direction cannot differ significantly from the value $\varphi'(z = R)$ in (67) on the axis OZ and from $\varphi(z = R)$ in (68). Indeed, the dependence

of the potential on the direction of the radius-vector $\mathbf{R}$ from the center of the sphere to the point with coordinates x,y,z, where the potential is calculated, could arise due to rotation. However, the potential φ' does not depend on ω and for the sphere at rest with $\omega = 0$, the potential is symmetric with respect to the choice of direction of the vector $\mathbf{R}$.

In this regard, we will assume that in (66),

$$\varphi' = \frac{\rho_{0q}\gamma_c}{4\pi\varepsilon_0}\int_{-a}^{a} H_1\, dz_d \approx \varphi'(z=R) = \frac{\rho_{0q}a^3\gamma_c}{3\varepsilon_0 R}. \quad (71)$$

Calculating the last three terms on the right-hand side of (66) in accordance with [16], taking into account (31), we find the potential at rather large R:

$$\varphi(R >> a) \approx \frac{q_\omega}{4\pi\varepsilon_0 R}\left[1 + \frac{\omega^2 a^2(x^2+y^2)}{10\,c^2R^2}\left(1 - \frac{225\pi a\sqrt{x^2+y^2}}{128R^2} - \frac{15a^2}{14R^2}\right)\right]. \quad (72)$$

Potential (72) actually has the same dependence on the angular velocity ω as potential (32) in the middle zone, but it is not exact in the near zone, where the radius R is not much larger than the sphere's radius a.

We can also estimate the potential in the case when $z = 0$, $R = a$ and all the integrals are taken quite easily. In this case, we find:

$$\int_{-a}^{a} H_3\,(R=a)dz_d = -\frac{1279\sqrt{2}\pi a^4}{240} - \frac{427\pi a^4}{16}\operatorname{lntg}\left(\frac{\pi}{8}\right) \approx 15{,}98\,\pi a^4.$$

Instead of (72) for the potential, we obtain the following:

$$\varphi\left(R=a\right) \approx \frac{q_\omega}{4\pi\varepsilon_0 a}\left(1 + \frac{6\omega^2 a^2}{c^2}\right). \quad (73)$$

Comparison of (73) with (72) shows that in our calculations at $z = 0$ on the surface of a rotating sphere, the correction with respect to the potential of a fixed sphere reaches the value of the order of $\frac{6\omega^2 a^2}{c^2}$.

2.9. Vector Potential in the Near Zone

Based on the similarity of formulae for scalar potential (16) and vector potential (18), in view of (63), we can express the components of the vector potential of the rotating disk in the near zone:

$$A_{dx} \approx -\frac{\mu_0\omega s\rho_{0q}}{4\pi}\int_0^{2\pi}\int_0^{\rho_d}\left[1 - \frac{\omega^2\rho^2(x\sin\phi - y\cos\phi)^2}{2c^2R_P^2} + \frac{\omega^2\rho x}{c^2}\cos\phi + \frac{\omega^2\rho y}{c^2}\sin\phi\right]\frac{\gamma'\sin\hat{\phi}\,\rho^2\,d\rho\,d\phi}{R_P}.$$

$$A_{dy} \approx \frac{\mu_0\omega s\rho_{0q}}{4\pi}\int_0^{2\pi}\int_0^{\rho_d}\left[1 - \frac{\omega^2\rho^2(x\sin\phi - y\cos\phi)^2}{2c^2R_P^2} + \frac{\omega^2\rho x}{c^2}\cos\phi + \frac{\omega^2\rho y}{c^2}\sin\phi\right]\frac{\gamma'\cos\hat{\phi}\,\rho^2\,d\rho\,d\phi}{R_P}.$$

Assuming $\hat{R}_P \approx R_P$, instead of (19), we have the following:

$$\cos\hat{\phi} \approx \cos\phi + \frac{\omega R_P}{c}\sin\phi,$$

$$\sin\hat{\phi} \approx \sin\phi - \frac{\omega R_P}{c}\cos\phi.$$

Taking this into account, we will transform the vector potential components A_{dx} and A_{dy}:

$$A_{dx} \approx -\frac{\mu_0\,\omega\,s\rho_{0q}}{4\pi}\int_0^{2\pi}\int_0^{\rho_d}\left[1-\frac{\omega^2\rho^2(x\sin\phi-y\cos\phi)^2}{2c^2R_P^2}+\right.$$
$$\left.+\frac{\omega^2\rho x}{c^2}\cos\phi+\frac{\omega^2\rho y}{c^2}\sin\phi\right]\frac{\gamma'\,\sin\phi\,\rho^2\,d\rho\,d\phi}{R_P}+$$
$$+\frac{\mu_0\,\omega^2\,s\rho_{0q}}{4\pi c}\int_0^{2\pi}\int_0^{\rho_d}\left[1-\frac{\omega^2\rho^2(x\sin\phi-y\cos\phi)^2}{2c^2R_P^2}+\right.$$
$$\left.+\frac{\omega^2\rho x}{c^2}\cos\phi+\frac{\omega^2\rho y}{c^2}\sin\phi\right]\gamma'\cos\phi\,\rho^2\,d\rho\,d\phi\,.$$
$$A_{dy} \approx \frac{\mu_0\,\omega\,s\rho_{0q}}{4\pi}\int_0^{2\pi}\int_0^{\rho_d}\left[1-\frac{\omega^2\rho^2(x\sin\phi-y\cos\phi)^2}{2c^2R_P^2}+\right.$$
$$\left.+\frac{\omega^2\rho x}{c^2}\cos\phi+\frac{\omega^2\rho y}{c^2}\sin\phi\right]\frac{\gamma'\cos\phi\,\rho^2\,d\rho\,d\phi}{R_P}+$$
$$+\frac{\mu_0\,\omega^2\,s\rho_{0q}}{4\pi c}\int_0^{2\pi}\int_0^{\rho_d}\left[1-\frac{\omega^2\rho^2(x\sin\phi-y\cos\phi)^2}{2c^2R_P^2}+\right.$$
$$\left.+\frac{\omega^2\rho x}{c^2}\cos\phi+\frac{\omega^2\rho y}{c^2}\sin\phi\right]\gamma'\,\sin\phi\,\rho^2\,d\rho\,d\phi\,.$$

(74)

Here, R_P is defined in (62).

After integration over the angle ϕ and the cylindrical coordinate ρ, the following is obtained:

$$A_x \approx -\frac{\mu_0\,\omega\,\rho_{0q}\,y\,\gamma_c}{4}\int_{-a}^{a}\left[\left(1-\frac{2\pi\eta\rho_0 z_d^2}{3c^2}\right)I_{26}-\frac{2\pi\eta\rho_0}{3c^2}I_{28}+\frac{\omega^2}{c^2}I_{25}+\right.$$
$$\left.+\frac{\omega^2\sqrt{x^2+y^2}}{c^2}I_{27}+\frac{3\pi\eta\rho_0\sqrt{x^2+y^2}}{c^2}I_{30}+\right.$$
$$\left.+\left(\frac{3\pi\eta\rho_0 z_d^2\sqrt{x^2+y^2}}{c^2}-\frac{9\sqrt{x^2+y^2}}{2}\right)I_{29}\right]dz_d-$$
$$\frac{\mu_0\,\omega^4\rho_{0q}\,x\,\gamma_c}{192\,c^3(x^2+y^2)}\int_{-a}^{a}[(R^2+a^2-2zz_d)^3-(R^2+z_d^2-2zz_d)^3-15(x^2+y^2)(a^2-z_d^2)^2]dz_d\,.$$
$$A_y \approx \frac{\mu_0\,\omega\,\rho_{0q}\,x\,\gamma_c}{4}\int_{-a}^{a}\left[\left(1-\frac{2\pi\eta\rho_0 z_d^2}{3c^2}\right)I_{26}-\frac{2\pi\eta\rho_0}{3c^2}I_{28}+\frac{\omega^2}{c^2}I_{25}+\right.$$
$$\left.+\frac{\omega^2\sqrt{x^2+y^2}}{c^2}I_{27}+\frac{3\pi\eta\rho_0\sqrt{x^2+y^2}}{c^2}I_{30}+\right.$$
$$\left.+\left(\frac{3\pi\eta\rho_0 z_d^2\sqrt{x^2+y^2}}{c^2}-\frac{9\sqrt{x^2+y^2}}{2}\right)I_{29}\right]dz_d-$$
$$\frac{\mu_0\,\omega^4\rho_{0q}\,y\,\gamma_c}{192\,c^3(x^2+y^2)}\int_{-a}^{a}[(R^2+a^2-2zz_d)^3-(R^2+z_d^2-2zz_d)^3-15(x^2+y^2)(a^2-z_d^2)^2]dz_d\,.$$

(75)

Here, the integrals I_{25}, I_{26}, I_{27}, I_{28}, I_{29} and I_{30} are calculated in [16].

It should be recalled that in the course of calculations, the integrals I_{11} and I_{12}, defined in (64), were calculated approximately, by using in (65) expansion up to the second-order terms. The same holds true for some integrals that appear when integrating over the angle ϕ.

A similar situation took place in the previous section, where we found that deviation of the scalar potential in our calculations in the equatorial plane on the sphere's surface reached 26% due to the fact that not all the expansion terms were used in (65). Therefore, it should be expected that although the dependence of the vector potential components on the coordinates x, y, z is shown correctly in (75), the inaccuracy increases as the sphere and the equatorial plane are approached.

In this regard, we will consider below two particular cases when the potential components are calculated in a relatively simple way, which makes it easy to analyze the solution. The first case refers to the region of space near the axis OZ, where it can be assumed that $z \approx R$, $R >> x$, $R >> y$. The second case refers to the points on the sphere's surface, where $z = 0$, $R^2 = x^2 + y^2$, while $R = a$.

2.9.1 The Case When $z \approx R$

In this case, at $x \approx 0$, $y \approx 0$, the integrals I_{11} and I_{12}, defined in (64), can be simplified, if we make substitution:

$$\frac{1}{\sqrt{R^2+z_d^2-2zz_d+\rho^2-2\rho x\cos\phi-2\rho y\sin\phi}} \approx \frac{1+\frac{\rho x\cos\phi+\rho y\sin\phi}{R^2+z_d^2-2zz_d+\rho^2}}{\sqrt{R^2+z_d^2-2zz_d+\rho^2}}.$$

Making similar replacements in the integrals that appear during integration over the angle ϕ and acting similarly to [16], we find the components of the vector potential at large distances, when $z \approx R$, $R > a$:

$$A_x(z \approx R > a) \approx -\frac{\mu_0\,\omega\,\rho_{0q}\,a^5 y\gamma_c}{15R^3}\left(1-\frac{10\pi\,\eta\,\rho_0\,a^2}{21\,c^2}-\frac{\omega^2 a^2}{7c^2}\right)- -\frac{\mu_0\,\omega^3\,\rho_{0q}\,a^5 y\gamma_c}{15\,c^2 R}+\frac{\mu_0\,\omega^4\,\rho_{0q}\,a^5 x\gamma_c}{15\,c^3}.$$

$$A_y(z \approx R > a) \approx \frac{\mu_0\,\omega\,\rho_{0q}\,a^5 x\gamma_c}{15R^3}\left(1-\frac{10\pi\,\eta\,\rho_0\,a^2}{21\,c^2}-\frac{\omega^2 a^2}{7c^2}\right)+ +\frac{\mu_0\,\omega^3\,\rho_{0q}\,a^5 x\gamma_c}{15\,c^2 R}+\frac{\mu_0\,\omega^4\,\rho_{0q}\,a^5 y\gamma_c}{15\,c^3}. \quad (76)$$

2.9.2 The Case When $R = \sqrt{x^2 + y^2} = a$

Let us now consider the second case, referring to the points on the sphere's surface, where $z = 0$, $R^2 = x^2 + y^2$, while $R = a$.

In order to simplify the calculations, in (75), we will limit ourselves to only the largest terms that do not contain c^2 and c^3 in the denominator. This gives us the following:

$$A_x\left(R=\sqrt{x^2+y^2}=a\right) \approx -\frac{10^{-4}\mu_0\,\omega\,\rho_{0q}\,a^2 y\,\gamma_c}{4},$$

$$A_y\left(R=\sqrt{x^2+y^2}=a\right) \approx \frac{10^{-4}\mu_0\,\omega\,\rho_{0q}\,a^2 x\,\gamma_c}{4}. \quad (77)$$

If we proceed from the form of (60) and (76), the vector potential components at $z = 0$ and $R = a$ should be approximately as follows:

$$A_x \approx -\frac{\mu_0\,\omega\,\rho_{0q}\,a^2 y\gamma_c}{15},\ A_y \approx \frac{\mu_0\,\omega\,\rho_{0q}\,a^2 x\gamma_c}{15}. \quad (78)$$

Apparently, the difference between the results of (77) and (78) was due to an inaccuracy that arose when some integrals were found by expanding the elliptic integrals into a series up to the second-order terms. Although the general behavior of the vector potential outside the rotating charged sphere is determined correctly, this accuracy turns out to be insufficient for the correct determination of the vector potential

directly at the equator of the sphere and expansion of the elliptic integrals up to higher-order terms is required here.

2.10 Electric and Magnetic Fields in the Near Zone

According to (46), the electric field depends on the potentials' rates of change in space and time. Since the vector potential at constant rotation of the sphere's particles does not depend on time, the expression $\mathbf{E} = -\nabla\varphi$ will hold true. Using (66), for the electric field, we find the following expression with the use of the sum of integrals:

$$E \approx -\frac{\rho_{0q}\gamma_c}{4\pi\varepsilon_0}\int_{-a}^{a}\nabla H_1\, dz_d - \frac{\omega^2\rho_{0q}\gamma_c}{8\pi c^2\varepsilon_0}\int_{-a}^{a}\nabla H_3\, dz_d + \frac{\eta\rho_0\rho_{0q}\gamma_c}{6c^2\varepsilon_0}\int_{-a}^{a} z_d^2\nabla H_1\, dz_d + \\ + \frac{\eta\rho_0\rho_{0q}\gamma_c}{6c^2\varepsilon_0}\int_{-a}^{a}\nabla H_2\, dz_d \ . \tag{79}$$

Still this expression is not final, since in it, we must first take the spatial gradients of the quantities H_1, H_2 and H_3 and then perform integration over the variable z_d.

The situation on the axis OZ turns out to be much simpler. Here, in view of (68), the field depends on the distance R approximately according to the Coulomb law for the charge q_ω:

$$\mathbf{E}(z=R) = -\nabla\varphi(z=R) = -\frac{d\varphi(z=R)}{d\mathbf{R}} \approx -\frac{q_\omega}{4\pi\varepsilon_0}\frac{d}{d\mathbf{R}}\frac{1}{\sqrt{\mathbf{R}^2}} = \frac{q_\omega\mathbf{R}}{4\pi\varepsilon_0 R^3}. \tag{80}$$

At small z, when $x^2+y^2 \approx R^2$ and $R >> a$, in order to estimate the electric field, we can use (72):

$$\mathbf{E}(R>>a) = -\nabla\varphi(R>>a) \approx \frac{q_\omega\mathbf{R}}{4\pi\varepsilon_0 R^3}\left(1+\frac{\omega^2a^2}{10c^2}\right). \tag{81}$$

If we proceed from the form of (73), then at $z=0$, $R\approx a$, for the electric field, we obtain the following:

$$\mathbf{E}(R\approx a) = -\nabla\varphi(R\approx a) \approx \frac{q_\omega\mathbf{R}}{4\pi\varepsilon_0 R^3}\left(1+\frac{6\omega^2a^2}{c^2}\right). \tag{82}$$

The inaccuracy in the definition of $\mathbf{E}(R\approx a)$ depends on the inaccuracy of the potential in (73).

In (75), approximate expressions were presented for the vector potential components $\mathbf{A}$. The subsequent application of the curl operation allows us to find the magnetic field by the formula $\mathbf{B} = \nabla\times\mathbf{A}$; however, the result is cumbersome.

The expressions for the vector potential components are greatly simplified near the axis OZ. Leaving the largest terms in (76) and taking into account that $A_z = 0$, we find:

$$A_x(z\approx R>a) \approx -\frac{\mu_0\,\omega\,\rho_{0q}a^5y\gamma_c}{15R^3}\left(1-\frac{10\pi\eta\rho_0a^2}{21c^2}-\frac{\omega^2a^2}{7c^2}\right).$$

$$A_y(z\approx R>a) \approx \frac{\mu_0\,\omega\,\rho_{0q}a^5x\gamma_c}{15R^3}\left(1-\frac{10\pi\eta\rho_0a^2}{21c^2}-\frac{\omega^2a^2}{7c^2}\right).$$

$$B_x(z\approx R>a) = \frac{\partial A_z}{\partial y}-\frac{\partial A_y}{\partial z} \approx \frac{\mu_0\,\omega\,\rho_{0q}a^5xz\gamma_c}{5R^5}\left(1-\frac{10\pi\eta\rho_0a^2}{21c^2}-\frac{\omega^2a^2}{7c^2}\right).$$

$$B_y(z\approx R>a) = \frac{\partial A_x}{\partial z}-\frac{\partial A_z}{\partial x} \approx \frac{\mu_0\,\omega\,\rho_{0q}a^5yz\gamma_c}{5R^5}\left(1-\frac{10\pi\eta\rho_0a^2}{21c^2}-\frac{\omega^2a^2}{7c^2}\right)$$

$$B_z(z \approx R > a) = \frac{\partial A_y}{\partial x} - \frac{\partial A_x}{\partial y} \approx \frac{\mu_0 \omega \rho_{0q} a^5 \gamma_c (2R^2 - 3x^2 - 3y^2)}{15R^5} \left(1 - \frac{10\pi\eta\rho_0 a^2}{21c^2} - \frac{\omega^2 a^2}{7c^2}\right). \quad (83)$$

In (83), $R > a$, but R is not much larger than the sphere's radius a.

The components of the magnetic field in (83) actually repeat expressions (47) for the magnetic field in the middle zone, with a slight difference in the terms containing the square of the speed of light.

3. Conclusion

The presence of the sphere's rotation leads to addition of cylindrical symmetry about the rotation axis OZ to the sphere's radial symmetry in the formulae for the potential. As a rule, this is expressed in the fact that the scalar potential of the electromagnetic field becomes dependent not only on the sphere's radius a, the distance R and the angular velocity ω, but also on the angle θ between the axis OZ and the direction to the point P where the potential is measured. The latter is confirmed by expressions for the potential (32) in the middle zone, (54) in the far zone, (72) and (73) in the near zone, from which it follows that the potential increases as the radius-vector $\mathbf{R}$ of the observation point approaches the equatorial plane of the rotating sphere. By the order of magnitude, the relative change in the potential does not exceed $\frac{6\omega^2 a^2}{c^2}$, depending on the sphere's radius a and on the angular velocity of rotation ω.

Thus, for the potential of the rotating sphere, we can expect dependence of the form $\varphi = \frac{q_\omega}{4\pi\varepsilon_0 R} F(a, R, \omega, \theta)$, where $F(a, R, \omega, \theta)$ is a certain function. In this case, the remote point P, where the potential is calculated, has a radius-vector $\boldsymbol{R} = (x, y, z) = (R\sin\theta\cos\phi,\ R\sin\theta\cos\phi,\ R\cos\theta)$. However, due to the sphere's symmetry, there is no dependence on the angle ϕ in the function $F(a, R, \omega, \theta)$ and in the potential φ.

In addition to the scalar potential, we calculate the vector potential in the middle zone (45), in the far zone (60) and in the near zone (75). The first terms in the vector potential components in (45) contain c^3 in the denominator and in (60), the similar terms contain c in the denominator. Such a change in the potential dependence, which appears when going over from the middle zone to the far zone, is a typical consequence of the method of retarded potentials.

In (45) and in (60), there is the same term $-\frac{10\pi\eta\rho_0 a^2}{21c^2}$ associated with the properties of the relativistic uniform system. However, the terms, which are proportional to $\frac{\omega^2 a^2}{c^2}$ and define the dependence on the angular velocity ω, have different coefficients. A similar situation occurs in the near zone for the case when $z \approx R > a$, which is seen in (76).

This can be explained by the fact that in the course of calculations, we used not coincident procedures for expansion of functions and their subsequent integration, which give different accuracy. Another possible explanation may be that, indeed, in different zones, the dependence on ω is different. The accuracy of the results obtained can be improved by increasing the terms in expansion of functions into series; however, introduction of each new term significantly complicates the calculations. It should be noted that for the purpose of more convenient analytical presentation of the results in an explicit form, some elliptic integrals were expanded into series up to the second- and third-order terms, while other integrals were expanded into series up to the sixth-order terms.

Using the obtained expressions for the scalar and vector potentials, we calculate the electric and magnetic fields outside the rotating charged sphere. The corresponding expressions for the fields are presented in (47) for the middle zone, in (61) for the far zone and in (79) in the near zone for $\mathbf{E}$. The formulae for the electric field $\mathbf{E}$ in the near zone are made more precise in (80) on the axis OZ, at small z in (81) and at $z = 0$, $R \approx a$ in (82). In all cases, we can see that the field $\mathbf{E}$ increases due to rotation, while the maximum relative increase does not exceed the value $\frac{6\omega^2 a^2}{c^2}$ near the sphere's surface in the plane XOY.

The components of the magnetic field $\mathbf{B}$ in the near zone on the axis OZ on condition that $z \approx R > a$ are presented in (83). Comparison of (47), (61) and (83) shows that within the framework of the approach used, the obtained approximate expressions for $\mathbf{B}$ differ in different zones in small terms, associated with the dependence on the angular velocity ω, repeating the corresponding difference for the vector potential $\mathbf{A}$.

Due to the charge conservation condition, the charge q_ω (31) of the rotating sphere is equal to the charge q_b of the fixed sphere in (8). This allows us to equate the Lorentz factor γ_c of the particles' motion in the center of the rotating sphere and the similar Lorentz factor γ_c' for the same and generally fixed sphere.

The results obtained can be applied to nucleons in atomic nuclei when calculating the binding energy in the gravitational model of strong interaction, which takes into account attraction of nucleons to each other in the strong gravitational field, repulsion of protons due to the electric force, repulsion of nucleons' magnetic moments oriented in the combined magnetic field, as well as interaction of the nucleons' spin gravitational moments in the torsion field of strong gravitation due to the nucleons' proper rotation. Since near the equatorial plane at the surface of a rotating proton the electric potential can be increased due to the addition of the order of $\frac{6\omega^2 a^2}{c^2}$ according to (73), then at a typical angular rotation velocity $\omega = 1.03 \times 10^{23}$ rad/s, according to [17], and at the proton radius of the order of 8.73×10^{-16} m, this increases the potential by a factor of 1.54. As a result, this also has an impact on the value of the binding energy of atomic nuclei.

Similar calculation for the neutron star PSR J1614–2230, for which the angular velocity of rotation is $\omega = 1.994 \times 10^3$ rad/s and the radius is $a = 12.8$ km according to [18], gives $\frac{\omega a}{c} = 8.51 \times 10^{-2}$ and $\frac{6\omega^2 a^2}{c^2} \approx 0.04$. So, if this star were charged, the field near the star's equator would probably also be increased by a factor of $1 + \frac{6\omega^2 a^2}{c^2} \approx 1.04$ as compared to the field of a non-rotating star. The same applies to the gravitational field in the covariant theory of gravitation, the equations of which are similar to the equations of the electromagnetic field [12].

Due to the fact that the calculations contain a great number of integrals, the key details of these calculations are presented in special files, which are included in an appendix to this work [16].

References

[1] Olbert, S. and Belcher, J.W., "The Electromagnetic Fields of a Spinning Spherical Shell of Charge". arXiv:1010.1917 (2010).

[2] Jackson, J.D., "Classical Electrodynamics", 2nd Ed., (John Wiley and Sons, 1975) Chapter 3 and 5.

[3] Griffiths, D.J., "Introduction to Electrodynamics", 3rd Ed., (Prentice Hall, Problem 5.29, 2007).

[4] Redzic, D.V., Progress In Electromagnetics Research, 110 (2010) 83.

[5] Gron, O. and Voyenli, K., European Journal of Physics, 3 (4) (1982) 210.

[6] Marsh, J.S., American Journal of Physics, 50 (1) (1982) 51.

[7] Marsh, J.S., American Journal of Physics, 52 (8) (1984) 758.

[8] Fedosin, S.G., American Journal of Modern Physics, 3 (4) (2014) 152.

[9] Fedosin, S.G., Jordan J. Phys., 8 (1) (2015) 1.

[10] Fedosin, S.G., Jordan J. Phys, 9 (1) (2016) 1.

[11] Fedosin, S.G., International Journal of Pure and Applied Sciences, 4 (2) (2018) 110.

[12] Fedosin, S.G., International Letters of Chemistry, Physics and Astronomy, 78 (2018) 39.

[13] Jefimenko, O.D., J. Phys. A: Math. Gen., 34 (31) (2001) 6143.

[14] Healy, W.P., J. Phys. A: Math. Gen., 35 (2002) 2527.

[15] Fedosin, S.G., International Letters of Chemistry, Physics and Astronomy, 83 (2019) 12.

[16] Fedosin, S.G., "Calculation of integrals and related data. Appendix to the article «The electromagnetic field outside the steadily rotating relativistic uniform system»". [Data set], (Zenodo, 2020).

[17] Fedosin, S.G., Hadronic Journal, 35 (4) (2012) 349.

[18] Demorest, P.B., Pennucci, T., Ransom, S.M., Roberts, M.S.E. and Hessels, J.W.T., Nature, 467 (7319) (2010) 1081.

Volume 14, Number 5, 2021. pp. 409-417

Jordan Journal of Physics

ARTICLE

Structural and Optical Properties of Pure NiO Nanoparticles and NiO-Mn_2O_3, NiO-CdO, NiO-Pb_2O_3, NiO-ZnO Nanocomposites

E. J. Vishaka[a], **M. Priya Dharshini**[b], **V. Shally**[b] and **Sr. Gerardin Jayam**[b]

[a] *Research Scholar (Reg.No:20213042132010), Research Department of Physics, Holy Cross College, Nagercoil – 629004. Affiliated to Manonmaniam Sundaranar University, Abishekapatti, Tirunelveli- 627012, India.*

[b] *Research Department of Physics, Holy Cross College, Nagercoil – 629004.*

Doi: **https://doi.org/10.47011/14.5.2**

Received on: 01/05/2020; *Accepted on: 25/1/2021*

Abstract: Pure nickel oxide (NiO) nanoparticles and NiO-Mn_2O_3, NiO-CdO, NiO-Pb_2O_3, NiO –ZnO nanocomposites were synthesized by co-precipitation method. The PXRD studies revealed that NiO, Mn_2O_3 and CdO possessed cubic structure, Pb_2O_3 possessed monoclinic structure, ZnO possessed hexagonal structure and confirmed the presence of polycrystallinity nature of NiO and Mn_2O_3, CdO, Pb_2O_3, ZnO in the nanocomposites. The average grain size of NiO nanoparticles was found to be 30.10 nm using Debye Scherer's formula. The FESEM images of NiO nanoparticles and their nanocomposites revealed spherical shaped structure and NiO-Pb_2O_3 revealed needle shaped rod-like structure. EDAX analysis confirmed the composition of NiO nanoparticles and their nanocomposites. Raman spectra exhibited characteristic peaks of pure NiO and that of NiO- Mn_2O_3, NiO-CdO, NiO- Pb_2O_3, NiO-ZnO in the synthesized nanocomposites. In the PL spectra, blue and green emission was observed in the samples. UV-vis spectra revealed the absorption peaks of NiO nanoparticles and their nanocomposites. Thus, the synthesized NiO- Mn_2O_3, NiO-CdO, NiO - Pb_2O_3 and NiO-ZnO nanocomposites can be a suitable material for electrocatalysis applications.

Keywords: Nickel oxide nanocomposites, Structure, Morphology, Absorption, Luminescence.

1. Introduction

Nickel oxide (NiO) is an important transition metal oxide that has been under the extensive investigation for decades due to its interesting electronic structures, strongly affected by Ni-3d electrons [1] which are localized in space, but spread out over a wide energy range because of strong Coulomb repulsion between them [2]. The high specific surface area of NiO nanoparticles has significant implications with respect to the energy storage devices based on electrochemically active sites (batteries, super capacitors) and energy conversion devices depending on catalytic sites or defect structures. NiO nanoparticles and their nanocomposites have been synthesized *via* a cost-effective and highly convenient co-precipitation method [3]. Mn_2O_3 nanoparticles can be utilized for advanced materials in batteries, as well as other applications, such as water treatment and imaging contrast agents [4]. CdO has potential applications in flat panel displays, organic light emitting diodes, optoelectronic devices, gas sensors and electrodes [5]. CdO also possesses both antibacterial and anticancer activity. Previous studies reported the synthesis of nanocomposites containing CdO and other metal oxide combinations [6]. The Pb_2O_3 nanoparticles are used in magnetic resonance and as magnetic nanoparticles for magnetic data storage and magnetic resonance imaging (MRI). The most

Corresponding Author: E. J. Vishaka **Email**: vishaka8397@gmail.com

common use of ZnO nanoparticles is in sunscreen, because they reflect ultraviolet light, but they are small enough to be transparent to visible light [7]. They are also being investigated to kill harmful microorganisms in packaging [8]. In this paper, nanocomposites of NiO were synthesized and their structural optical properties were analyzed.

2. Materials and Methods

In the present work, co-precipitation method is used to prepare NiO and their nanocomposites. All the precursors used for synthesis were of analytical grade (Merck). Pure nickel acetate, manganese acetate, cadmium acetate, lead acetate, zinc acetate, double distilled water, urea and ammonium hydroxide solution were used to synthesize NiO nanoparticles and their nanocomposites.

2.1 Synthesis of NiO Nanoparticles

Nickel acetate (0.25 M) is dissolved in double distilled water (100 ml) separately and stirred well for 30 minutes. Then, urea (0.75 M) is dissolved in double distilled water (100 ml) separately and stirred well. Then, both nickel acetate and urea solutions are mixed together. Ammonium hydroxide solution (32 M) is added drop by drop to maintain the pH of 10.The obtained green color precipitate is kept in the hot air oven at 100°C for drying. After grinding in agate mortar, the powder is kept in the muffle furnace at 400°C for 2 hours and the black color powder is obtained.

2.2 Synthesis of NiO Nanocomposites

Manganese acetate (0.25 M) is dissolved in double distilled water separately and stirred well for 30 minutes. Then, manganese acetate solution is added dropwise to the nickel acetate and urea solutions which are already mixed together. Ammonium hydroxide solution is added dropwise to maintain the pH of 10. The brown color precipitate is dried at 100°C in the hot air oven. After grinding the sample, it is kept in the muffle furnace at 400°C for two hours. Similar procedure is adopted for synthesizing other nanocomposites. In the place of manganese acetate, cadmium acetate is used for NiO-CdO nanocomposites, lead acetate is used for NiO-Pb_2O_3 nanocomposites and zinc acetate is used for NiO-ZnO nanocomposites.

3. Results and Discussion

3.1 PXRD Analysis

The powder X-Ray diffraction pattern of NiO nanoparticles and their nanocomposites were recorded using XPERT-PRO Diffraction system with Cu$K\alpha$ radiation of wavelength 1.54056 Å. The PXRD patterns obtained for the NiO and their nanocomposites are shown in Fig.1 (a-e).The observed 2θ values were matched well with the cubic structure of NiO(JCPDS File No.89-5881) [9,10]. The relatively sharp and high intense diffraction peaks clearly indicate the crystalline nature of the synthesized pure NiO nanoparticles. The high intensity peaks are observed at (222), (400), (440) and (622) corresponding to 2θ = 37.1979°, 2θ = 43.1980°, 2θ = 62.8085° and 2θ = 75.2708°, respectively. (Fig.1a) indicates the PXRD pattern of NiO nanoparticles. No peaks were observed from other impurities, such as $Ni(OH)_2$, indicating the high purity of the synthesized NiO nanoparticles.

Fig.1b portrays the XRD pattern of NiO-Mn_2O_3 nanocomposites. Diffraction peaks of both NiO and Mn_2O_3 were observed and matched with the standard JCPDS file (for Mn_2O_3(JCPDS File No.71-0636) and NiO(JCPDS File No. 89-5881)). The material belongs to the cubic structure. The diffraction peaks are of low intensity when compared to the pure NiO nanoparticles (Fig.1b), which shows less crystallinity of NiO-Mn_2O_3 nanocomposites. The peaks of Mn_2O_3 are observed at (321), (440) corresponding to 2θ = 35.7703° and 2θ = 63.4698° respectively and the peaks of NiO are observed at (111), (222), (400), (511) and (622) corresponding to 2θ = 18.4211°, 2θ=37.4112°, 2θ = 43.5952°, 2θ = 57.6035° and 2θ = 75.8341°, respectively.

In the NiO-CdO composites, both the diffraction peaks of the cubic phases were present for CdO(JCPDS File No. 05-0640) and NiO(JCPDS File No. 89-5881) [11].The peaks of CdO are observed at (200), (220), (311) and (222) corresponding to 2θ = 38.2483°, 2θ = 55.2383°, 2θ = 65.9156° and 2θ = 69.1591°, respectively and the peaks of NiO are observed at (111), (311), (400) and (440) corresponding to 2θ = 32.9683°, 2θ = 35.5949°, 2θ = 43.1799° and 2θ = 63.0358°, respectively (Fig.1c). The NiO peak corresponding to (111) is of high relative intensity.

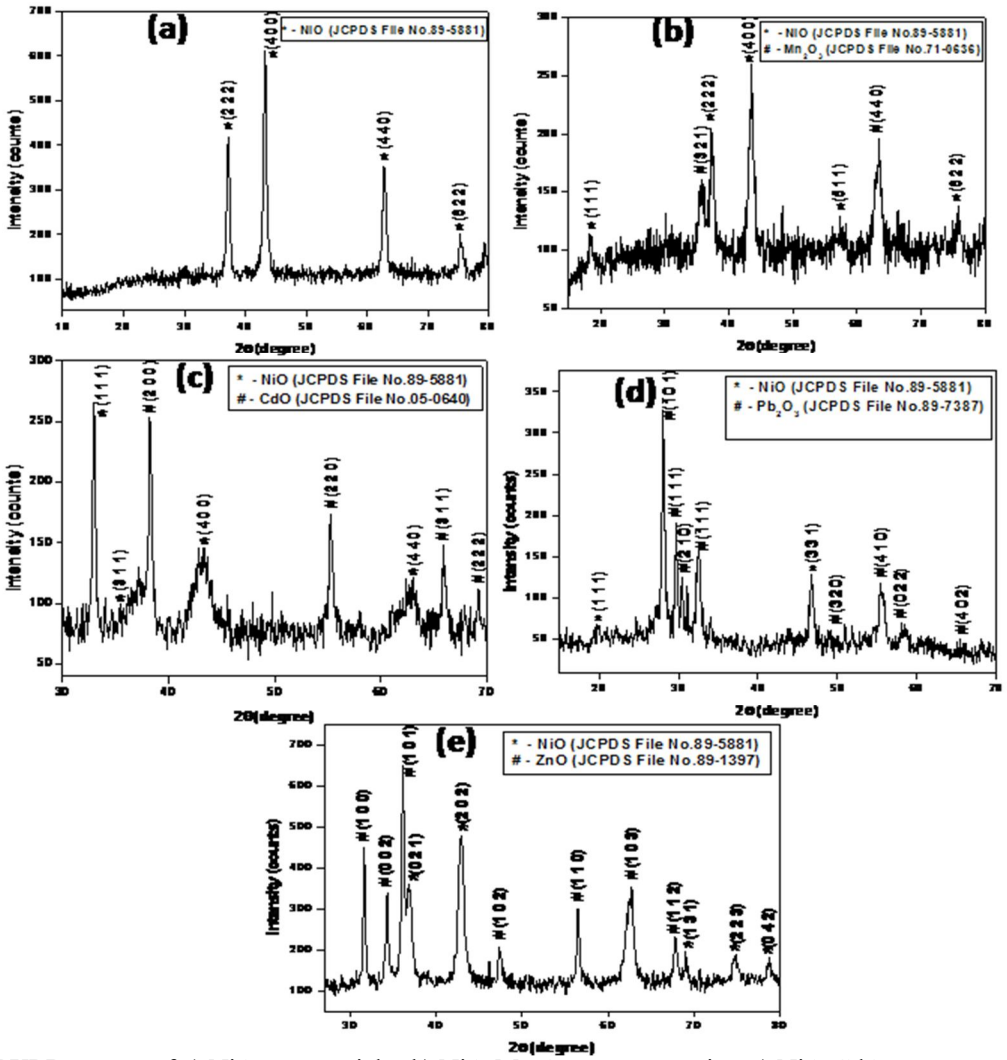

FIG. 1. PXRD pattern of a) NiO nanoparticles b) NiO-Mn_2O_3 nanocomposites c) NiO-CdO nanocomposites d) NiO-Pb_2O_3 nanocomposites e) NiO-ZnO nanocomposites.

The presence of monoclinic Pb_2O_3 (JCPDS File No.89-7387) and cubic NiO (JCPDS File No.89-5881) in the synthesized nanocomposites confirms the formation of NiO-Pb_2O_3 nanocomposites [12] (Fig.1d). The peaks of Pb_2O_3 are observed at (101), (111), (210), (020), (111), (320), (410), (022) and (402) corresponding to 2θ = 28.0724°, 2θ = 29.7112°, 2θ = 30.4154°, 2θ = 31.1061°, 32.5639°, 2θ = 50.9270°, 2θ = 55.2597°, 2θ = 58.4788° and 2θ = 65.7442°, respectively and the peaks of NiO are observed at (111) and (331) corresponding to 2θ = 19.9476° and 2θ = 46.7938°, respectively.

The presence of hexagonal ZnO (JCPDSFileNo.89-1397) and cubic NiO (JCPDSFile No.89-5881) in the synthesized nanocomposites confirms the formation of NiO-ZnO nanocomposites [13, 14]. The peaks of ZnO are observed at (100), (002), (101), (102), (110), (103) and (112) corresponding to 2θ = 31.6276°, 2θ = 34.2888°, 2θ = 36.1362°, 2θ = 47.3647°, 2θ = 56.4882°, 2θ = 62.8006° and 2θ = 67.8877°, respectively and the peaks of NiO are observed at (021), (202), (131), (223) and (042) corresponding to 2θ = 36.9005°, 2θ = 42.7812°, 2θ=68.9920°, 2θ = 74.6008° and 2θ = 78.6843°, respetively. More number of ZnO peaks are observed and the ZnO peak corresponding to (101) is of high relative intensity (Fig.1e).

The average grain size of synthesized Nickel Oxide nanoparticles is found out from the powder XRD pattern using Debye Scherrer's formula:

$$D = 0.9\lambda/\beta\cos\theta \text{ (nm)}$$

where λ is the wavelength of PXRD, β is the full width half maximum; θ is the Bragg's angle for the peak. The average size of NiO nanoparticles is found to be 30.1052 nm.

TABLE 1. Comparison of average grain size of nanopowder samples.

S.No.	Nanopowder samples	Angle 2θ (degree)	θ (degree)	FWHM β (degree)	Average grain size D (nm)
1	NiO	47.7348	23.8674	0.328	30.1052
2	NiO-Mn_2O_3	48.1587	24.0793	0.5576	19.6660
3	NiO-CdO	48.0926	24.0463	0.2952	29.4914
4	NiO-Pb_2O_3	34.2853	17.1426	0.2583	32.2104
5	NiO-ZnO	43.3364	21.6682	0.3075	27.8206

3.2 SEM and EDAX Analysis

In order to produce clearer, less electrostatically distorted images, Field Emission Scanning Electron Microscopy (FESEM) was used in the present work and the FESEM images of the NiO nanoparticles and their nanocomposites were obtained using a JEOL JSM – 6390 microscope operating at an accelerating voltage of 20 kV.

Particles of average size 250 nm were observed in the FESEM image of pure NiO nanoparticles at a magnification of 1 μm [15] (Fig.2a). The FESEM image of the NiO-CdO nanocomposites (Fig.2b) displays the particles with an average size of 855 nm. Needle-shaped rod-like structure with an average size of 880 nm was observed for NiO-Pb_2O_3 nanocomposites at a magnification of 2 μm (Fig.2c). Fig.2d shows that the NiO-Mn_2O_3 nanocomposites contain spherical-shaped particles with an average size of 350 nm at a magnification of 1 μm. The spherical-shaped morphology is obtained for NiO-ZnO nanocomposites with an average size of 900 nm at a magnification of 30 μm (Fig.2e).

EDAX images (Fig. 3) show the formation of the respective elements present in the pure NiO nanoparticles and their nanocomposites.

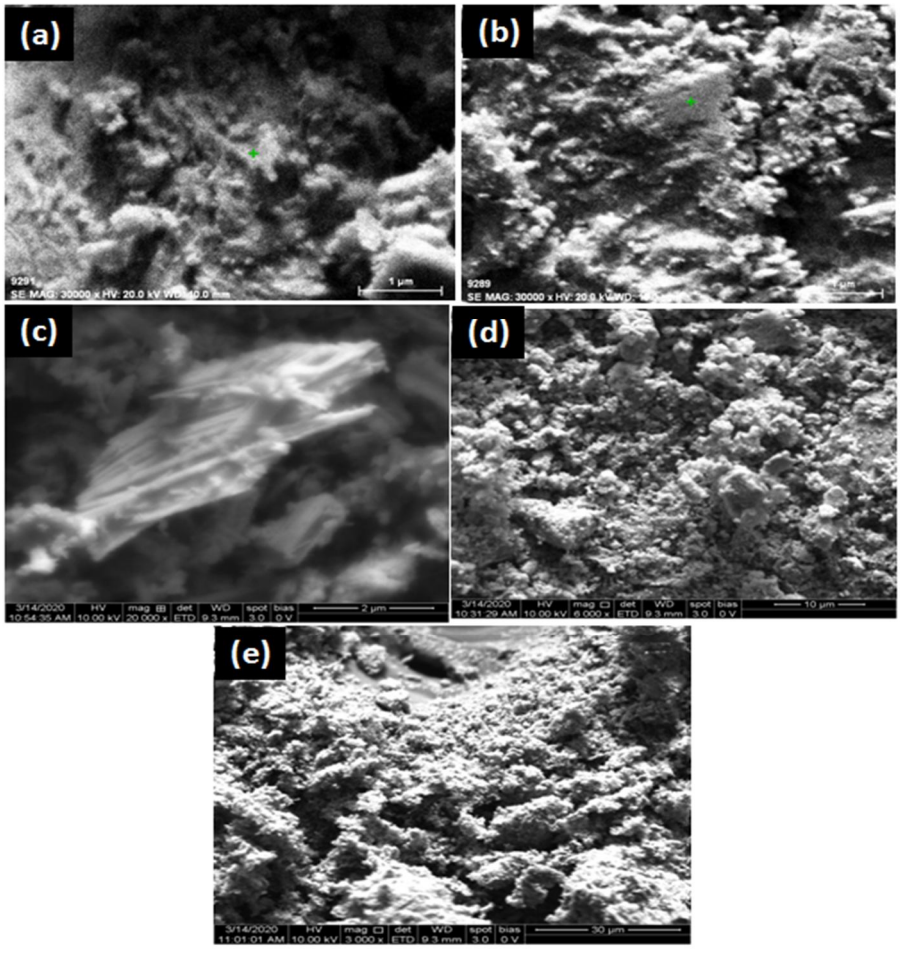

FIG. 2. FESEM image of a) NiO nanoparticles b) NiO-CdO nanocompositesc) NiO-Pb_2O_3 nanocomposites d) NiO-Mn_2O_3 nanocomposites e) NiO-ZnO nanocomposites.

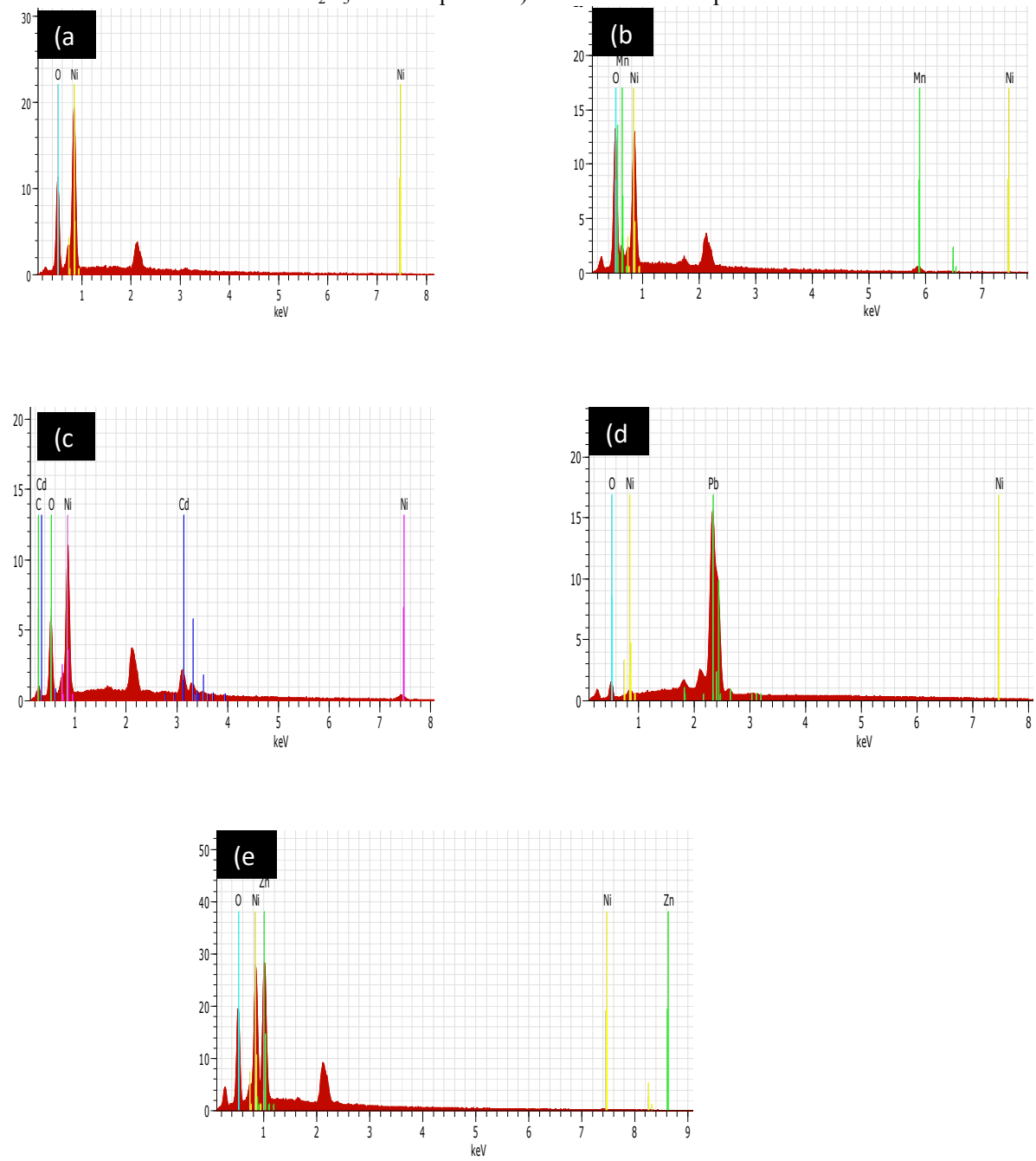

FIG. 3. EDAX image of a) NiO nanoparticles b) NiO-Mn_2O_3 nanocomposites c) NiO-CdO nanocomposites d) NiO- Pb_2O_3 nanocomposites e) NiO-ZnO nanocomposites.

3.2 Raman Analysis

Raman analysis is a spectroscopic technique used to observe vibrational, rotational and other low-frequency modes in a system. Raman spectroscopy is commonly used in chemistry to provide a structural fingerprint by which molecules can be identified.

Three Raman peaks of NiO located at 165, 510 and 1042 cm^{-1} confirm the characteristic feature of NiO [16]. The band at 510 cm^{-1} is attributed to one phonon (450 cm^{-1}) plus one magnon (60 cm^{-1}) excitation of NiO. The NiO-Mn_2O_3 nanocomposites show Raman peaks at 507cm^{-1}, 579 cm^{-1} and 633 cm^{-1}. The intensity of the characteristic peak is found to be decreasing when compared to pure NiO nanoparticles.The

NiO-CdO nanocomposites show Raman peaks at 486 and 1012 cm^{-1}. The shift in band from 510 cm^{-1} to 486 cm^{-1} might be due to the decreased particle size compared to pure NiO nanoparticles [17]. The NiO-Pb_2O_3 nanocomposites show Raman peaks at 262 and 525 cm^{-1}. The peaks have different shift values and the intensity of the peak is found to be increasing when compared to the spectrum of pure NiO nanoparticles. The NiO-ZnO nanocomposites show Raman peaks at 552 and 1058 cm^{-1}. This modification is probably due to the loss of lattice oxygen at high temperatures that leads to the surface reconstruction [18]. Generally, one phonon TO and LO modes of NiO would be observed at ~ 500-570 cm^{-1} [19]. The band observed at 500-525 cm^{-1} symbolizes the presence of NiO.

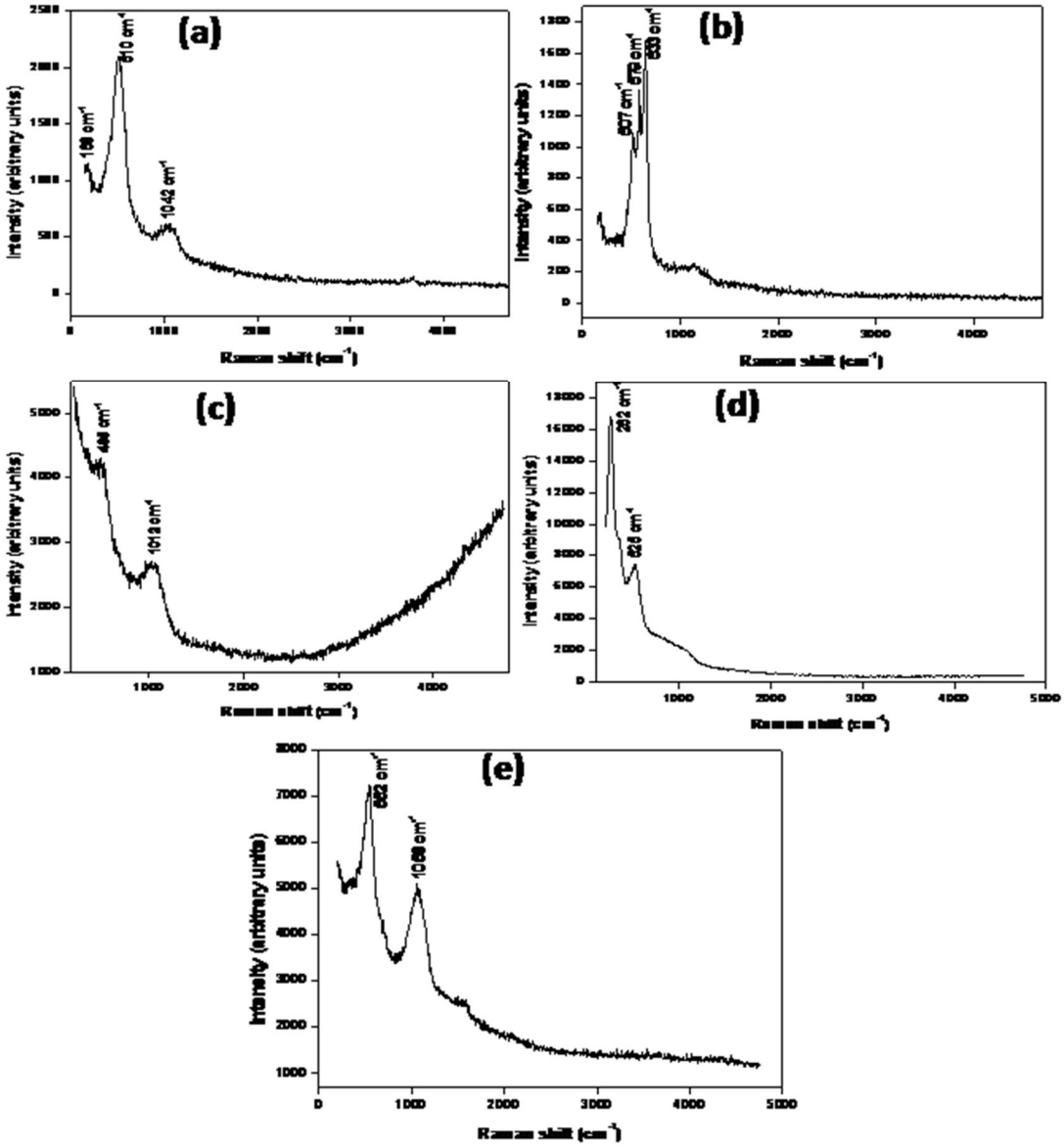

FIG. 4. Raman spectrum of a) NiO nanoparticles b) NiO-Mn_2O_3 nanocomposites c) NiO-CdO nanocomposites d) NiO- Pb_2O_3 nanocomposites e) NiO-ZnO nanocomposites.

3.3 Photoluminescent Analysis

Photoluminescence (PL) studies for the synthesized nanostructures were carried out using a photoluminescence spectrophotometer (Cary Eclipse) and the emission spectra were recorded at a scan rate of 600 nm/min using an excitation wavelength of 325nm.

Fig.5a depicts the photoluminescence (PL) emission spectrum and shows a maximum peak at 361 nm. High intense peaks centered at 361 nm are assigned to band edge emission of NiO nanocrystallites. The PL emission spectrum of NiO - Mn_2O_3 nanocomposites (Fig.5d) shows prominent peak at 360 nm. The PL emission

spectrum of NiO–CdO nanocomposites (Fig.5b) shows prominent peak at 491 nm. The intensity of the maximum peak is decreasing when compared to the pure NiO nanoparticles. The PL emission spectrum of NiO - Pb_2O_3 nanocomposites (Fig.5c) shows strong emission band at 491 nm close to the edge of the blue region. The PL emission spectrum of NiO–ZnO nanocomposites (Fig.5e) which shows maximum peak at 491 nm is similar to Petronela et al.'s work on NiO-ZnO [20]. In the photoluminescent spectra, blue and green emission is observed in the NiO nanoparticle and their composites [21].

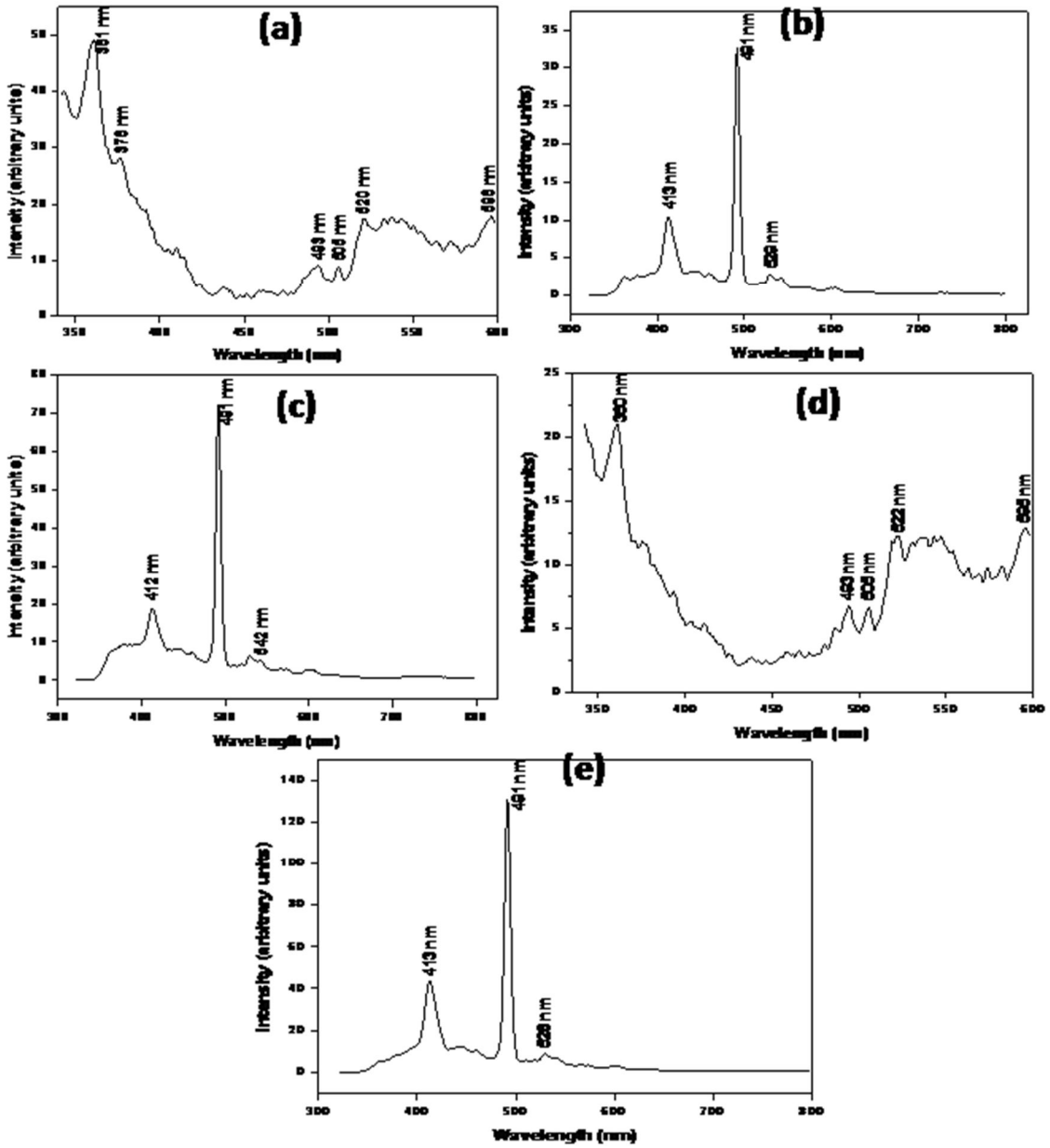

FIG. 5. PL spectrum of a) NiO nanoparticles b) NiO-CdO nanocomposites c) NiO-Pb_2O_3 nanocomposites d) NiO-Mn_2O_3 nanocomposites e) NiO-ZnO nanocomposites.

3.4 UV – Visible Analysis

To characterize the absorption properties of the synthesized samples, UV-Vis absorption spectrophotometer (Hitachi U-2900) was used at a scan speed of 400 nm/min in the range of 190 nm-800 nm.

It can be seen that the absorption edge corresponding to NiO appeared at 327 nm [22], the absorption edge corresponding to NiO-Mn_2O_3 appeared at 367 nm, the absorption edge corresponding to NiO-CdO appeared at 443 nm, the absorption edge corresponding to NiO-Pb_2O_3 appeared at 372 nm and the absorption edge

corresponding to NiO-ZnO appeared at 323 nm [23], respectively. There was blue shift absorbed in all the synthesized samples.

UV studies also support the blue emission of the synthesized NiO nanoparticles and nanocomposites.

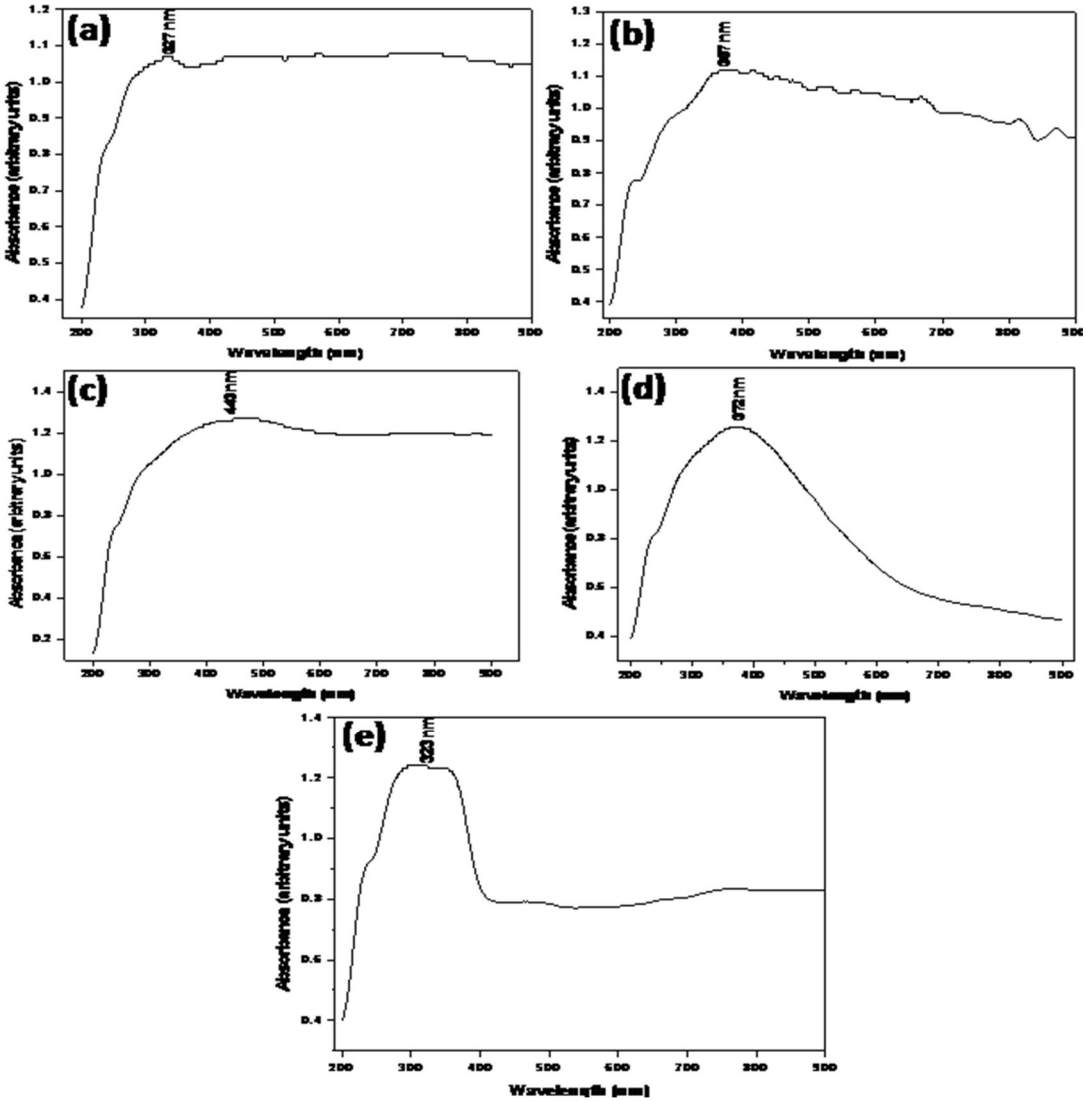

FIG. 6. UV-vis absorption spectrum of a) NiO nanoparticles b) NiO-Mn_2O_3 nanocomposites c) NiO-CdO nanocomposites d) NiO-Pb_2O_3 nanocomposites e) NiO-ZnO nanocomposites.

4. Conclusion

Co-precipitation method is used to synthesize pure NiO nanoparticles and their nanocomposites. PXRD and SEM studies confirmed the nanostructures for the prepared samples. The average size of NiO nanoparticles is found to be 30.1052 nm using Debye Scherer's formula. Spherical-shaped structure was obtained for NiO nanoparticles and their nanocomposites and needle-shaped rod-like structure was obtained for NiO-Pb_2O_3. The formation of NiO nanoparticles and their nanocomposites was confirmed by EDAX. Raman spectrum showed the characteristic peaks of pure NiO and their synthesized nanocomposites. The PL study of NiO nanoparticles and their nanocomposites revealed the blue and green emissions. UV-vis spectra revealed the absorption edges corresponding to NiO at 327 nm, NiO- Mn_2O_3 at 367 nm, NiO-CdO at 443 nm, NiO-Pb_2O_3 at 372 nm and NiO-ZnO at 323 nm. Thus, the synthesized NiO nanocomposites are suitable for electrocatalysis application in future. Transition metal oxides have proved to be active in catalytic reactions and were used as good electrocatalysts as reported in literature. Since the nanocomposites of oxides Mn_2O_3, CdO, Pb_2O_3 and ZnO based on NiO are successfully synthesized; in future works, the synthesized samples can be further modified for electrocatalysis applications.

References

[1] Xiaoming, F. and Zaizhi, Y., Advanced Materials Research, 228-229 (2011) 34.

[2] Fu, S.-Y. and Liu, X.-M., Progress in Solid State Chemistry Research, 2007 (2007)165.

[3] Kaur, N., Singh, J., Kaur, G., Kumar, S., Kukkar, D. and Rawat, M., Micro and Macro Letters, 14 (2019) 856.

[4] Chen, H. and He, J., J. Phys. Chem., 112 (2008) 17540.

[5] Kumar, P.S., Selvakumar, M., Bhagabati, P., Bharathi, B., Karuthapandian, S. and Balakumar, S., RSC Adv., 4 (2014) 32977.

[6] Liu, B., Chew, C.H., Gan, L.M. and Xu, G.Q., J. Mater. Res., 16 (2001) 1644.

[7] Kessler, R., Environmental Health Perspectives, 119 (3) (2011) A120.

[8] Iosub, C.S., Olareţ, E., Grumezescu, A.M., Holban, A.M. and Andronescu, E., Nanostructures for Novel Therapy, Elsevier, 2017 (2017) 793.

[9] Davar, F., Fereshteh, Z. and Salavati-Niasari, M., J. Alloys Compd., 476 (2009) 797.

[10] Zhu, J., Gui, Z., Ding, Y., Wang, Z., Hu, Y. and Zou, M., J. Phys. Chem. C, 111 (2007) 5622.

[11] Karthik, K., Dhanuskodi, S., Gobinath, C., Prabukumar, S. and Sivaramakrishnan, S., J. Phys. Chem. Solids, 112 (2018) 106.

[12] Aliakbari, A., Najafi, E., Amini, M.M. and Weng Ng, S., Monatsh. Chem., 145 (2014) 1277.

[13] Zhou, J., Zhao, F., Wang, Y., Zhang, Y. and Yang, L., J. Lumin., 122-123 (1-2) (2007) 195.

[14] Khoshhesab, Z.M., Sarfaraz, M. and Asadabad, M.A., Synthesis and Reactivity in Inorganic, Metal-Organic and Nano-Metal Chemistry, 41 (7) (2011) 814.

[15] Khalaji, A.D. and Das, D., International Nano Letters, 4 (2014) 117.

[16] Cordoba-Torresi, S.I., Hugot-Le Goff, A. and Joiret, S., J. Electrochem. Soc., 138 (1991) 1554.

[17] Mironova-Ulmane, N, J. Phys.: Conf. Ser., 93 (2007) 012039.

[18] Luo, Y., Deng, Y., Mao, W., Yang, X.-J., Zhu, K., Xu, J. and Han, Y.-F., J. Phys. Chem. C, 116 (39) (2012) 20975.

[19] Sone, B.T., Fuku, X.G. and Maaza, M., Int. J. Electrochem. Sci., 11 (2016) 8204.

[20] Dorneanu, P.P., Airinei, A., Olaru, N., Homocianu, M., Nica, V. and Doroftei, F., Mater. Chem. Phys., 148 (2014) 1029.

[21] Riegel, G. and Bolton, J.R., J. Phys. Chem., 99 (1995) 4215.

[22] Dharmaraj, N., Prabu, P., Nagarajan, S., Kim, C.H., Park, J.H. and Kim, H.Y., Mater. Sci. Eng. B, 128 (2006) 111.

[23] Mote, V.D., Purushotham, Y. and Dole, B.N., Journal of Theoretical and Applied Physics, 6 (6) (2012) 2251.

Volume 14, Number 5, 2021. pp. 419-424

Jordan Journal of Physics

ARTICLE

Structural and Surface Characteristics of CuO and Pt/CuO Nanostructured Thin Films

C. G. Jinitha[a], **P. Abisha**[b], **S. Sonia**[c], **Naidu Dhanpal Jeyram**[d] and **S. Virgin Jeba**[e]

[a] *Research Scholar (Reg. No. 19213042132016), Department of Physics, Holy Cross College, Nagercoil, Affiliated to Manonmaniam Sundaranar University, Abishekapatti, Tirunelveli-627012, India.*

[b] *M. Phil Scholar (Reg. No. 191408), Department of Physics, Holy Cross College, Nagercoil, Affiliated to Manonmaniam Sundaranar University, Abishekapatti, Tirunelveli-627012, India.*

[c] *Department of Physics, Holy Cross College, Nagercoil-4, India.*

[d] *Department of Physics, Kalasalingam Academy of Research and Education, Krishnan Koil - 626126, India.*

[e] *Research Scholar, Department of Physics, Holy Cross College, Nagercoil, Affiliated to Manonmaniam Sundaranar University, Abishekapatti, Tirunelveli-627012, India.*

Doi: **https://doi.org/10.47011/14.5.3**

Received on: 01/05/2020; *Accepted on: 05/04/2021*

Abstract: The most prominent and utilizable platinum-coated copper Oxide nanostructured thin films are prepared using the SILAR method. Their structural properties have been studied using X-ray diffraction (XRD) and Raman spectroscopy. XRD pattern reveals the phase purity and crystallinity of CuO nanostructures. The average grain size estimated from XRD gives diameters in the range of 14 - 27 nm. Raman spectra explain the structural information of CuO and Pt/CuO nanostructured thin films, in which the peaks observed at 328 cm^{-1}, 609.32 cm^{-1} and 1141.77 cm^{-1} are the different phonon modes of CuO. The peak at 2136 cm^{-1} provides strong evidence for the formation of platinum on CuO nanostructures. The SEM micrograph confirms the floral morphology, which is composed of nano petals. From the observed morphology, it is observed that the deposited thin films such as CuO and Pt/CuO will give interesting applications to our society by being self-cleaning agents, photocatalysts, semiconductor devices, optical fibers, … etc.

Keywords: CuO, Pt/CuO, Structural analysis, SILAR, Crystallinity.

1. Introduction

Copper oxide, including cuprous oxide (copper (I) oxide) and cupric oxide (copper (II) oxide), is formed when copper is exposed to oxygen [1]. These semiconductor oxides have been investigated for various purposes, such as the inherent abundance of starting material (Cu), the ease of production by Cu oxidation, their non-toxic nature and the reasonably good electrical and optical properties exhibited by CuO [2]. Previous works showed that many of the growth methods for copper oxide resulted in a combined growth of copper (I) oxide (Cu_2O) and copper (II) oxide (CuO). However, CuO is a more widely used material than Cu_2O due to its stability. Cupric oxide (CuO) possesses a monoclinic crystal structure with a bandgap of 1.22–2.0 eV [3, 4]. Its high optical absorption coefficient in the visible range and reasonably good electrical properties constitute important advantages and render CuO as the most

Corresponding Author: S. Sonia **Email**: sonianst10@gmail.com

interesting phase of copper oxides. CuO has been employed as a heterogeneous catalyst for several environmental processes, solid-state gas sensor heterostructures and microwave dielectric materials.

In solution-phase deposition methods, various complexing agents have been added to the growth solution to enhance the physical properties of the thin films. CuO thin films exhibit an exceptional combination of multifunctional characteristics, including optical, electronic, optoelectronic, magnetic and semiconducting. SILAR is a simple solution-based method for the suitable formation of thin films with controlled thickness and deposition temperature [5, 6]. Novel morphology of CuO was obtained by SILAR method due to metal doping or presence of additives [7, 8, 9]. The chief purpose of this article is to study the CuO thin films and SILAR method as an alternative to standard coating methods, which are budgetary and easily suitable. In order to achieve this goal, CuO thin films were deposited on glass substrates using SILAR method without any additives or dopants. The structural and surface properties of the untreated sample and thin films were characterized by X-ray diffraction (XRD), scanning electron microscopy (SEM) and Raman spectroscopy [10, 11].Copper (II) oxide, CuO, is a p-type semiconductor with a narrow bandgap (1.2–1.7 eV) and high stability in harsh terms [12, 13]. The structural, morphological and optical properties of CuO thin films can be used in photovoltaic applications [14]. Nanostructures of CuO films have different forms, such as tetrapods, flowers, nanorods, nanoribbons, nanowires, nanobelts, nanosheets, micro-roses, woolen, lotus, nanowire, nanosheet and flower-like [15]. The monoclinic structured CuO thin films are appropriate for photovoltaic and optoelectronic applications, such as optical devices [16], super hydrophobic [17], photocatalysis [18], microwave dielectric materials [19], lithium-ion batteries [20] and gas sensors [21].Among different chemical methods, successive ionic layer adsorption and reaction (SILAR) is a facile, economically feasible and most versatile method in order to deposit material directly on the substrate. Moreover, the SILAR method holds a promise to develop different morphologies by controlling simple preparative parameters [16, 22, 23]. Hence, the present report focused on the synthesis of such CuO nanostructured thin films and structural properties of CuO thin films deposited by SILAR method.

2. Experimental Section

2.1 Substrate Preparation

Glass substrates were used to grow copper (II) oxide thin films. Before starting the growth, the substrates were cleaned using soap, acetone and distilled water for 10 minutes. Then, the substrates were air-dried.

2.2 Preparation of CuO Nanostructured Thin Films

Initially, the glass substrate is dipped in copper ammonia complex [(Cu $(NH_3)_4)^{2+}$] solution for 40 sec for the adsorption of the cationic solution. Next, the glass substrate is immersed in double distilled water for 20 sec for rinsing. Then, the substrate is dipped in the anionic solution (i.e., double distilled water at 80ºC) for 50 sec. Then, the substrate is immersed in double distilled water for 20 sec for rinsing. As the final step of the cycle, the substrate is dried in air for 20 secs. Thus, one SILAR cycle is completed. In order to obtain uniform deposition, cycles were repeated for 20 and 40 times.

2.3 Preparation of Pt/CuO Nanostructured Thin Films

20 ml of 1 mM aqueous solution of $H_2PtCl_6 \cdot 6H_2O$ was added and stirring was performed for 15 min. The redox reaction was started by adding solid tri-sodium citrate. The reaction was carried out for 120 min. All experiments were performed at room temperature. CuO nanostructured thin films were immersed in platinum sol for 3h. After 3hr, Pt/CuO nanostructured thin films were dried in air and subjected to different characterization techniques to study their structural and surface properties.

3. Results and Discussion

3.1 Structural Analysis

The phase purity and crystallinity of the prepared CuO and Pt/CuO nanostructured thin films were identified by X-ray diffraction analysis. The XRD patterns of the CuO and Pt/CuO nanostructured thin films are shown in Fig. 1 (a and b). All the diffraction peaks of CuO nanostructured thin films can be readily indexed

with the standard JCPDS (PDF#05-0661) file. The XRD patterns of CuO nanostructured thin films prepared by different deposition cycles consist of diffraction peaks derived from the monoclinic phase of crystalline CuO with ($\bar{1}$11) and (111) lattice planes. Conversely, no extra diffraction peaks are detected from the copper hydroxide or cuprous oxide, clearly showing that only CuO is formed in the substrate. The high intensity of peaks indicates that the prepared CuO thin films are highly crystalline in nature. Fig.2 (a and b) indicates the XRD pattern of Pt/CuO nanostructured thin films and shows the amorphous nature. The average crystallite size for the CuO thin films is estimated from Scherrer's formula and is varying from 14 to 27 nm.

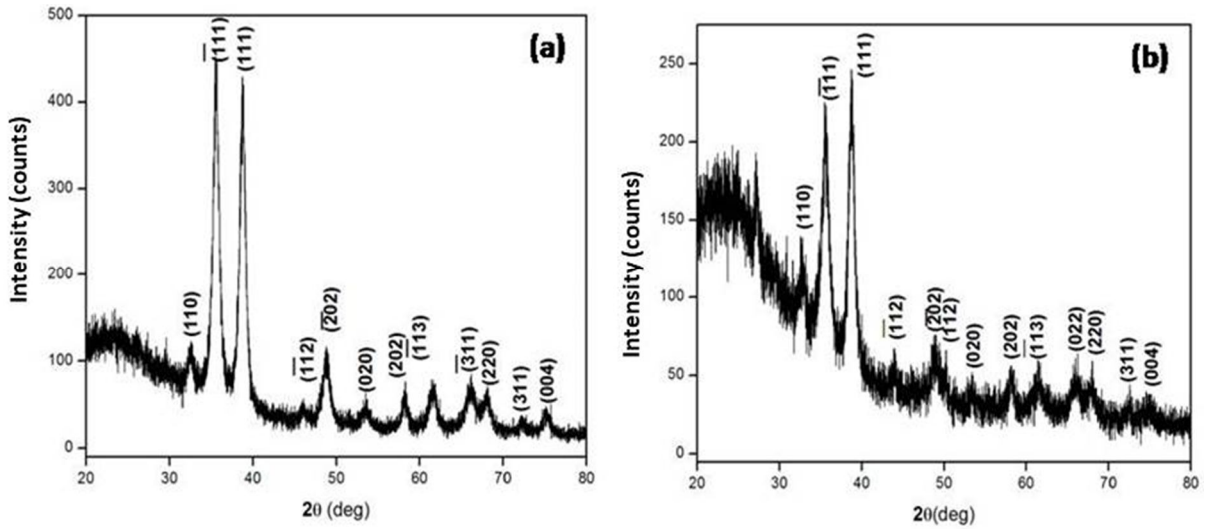

FIG. 1. XRD pattern of CuO nanostructured thin films prepared at a) 20 and b) 40 deposition cycles.

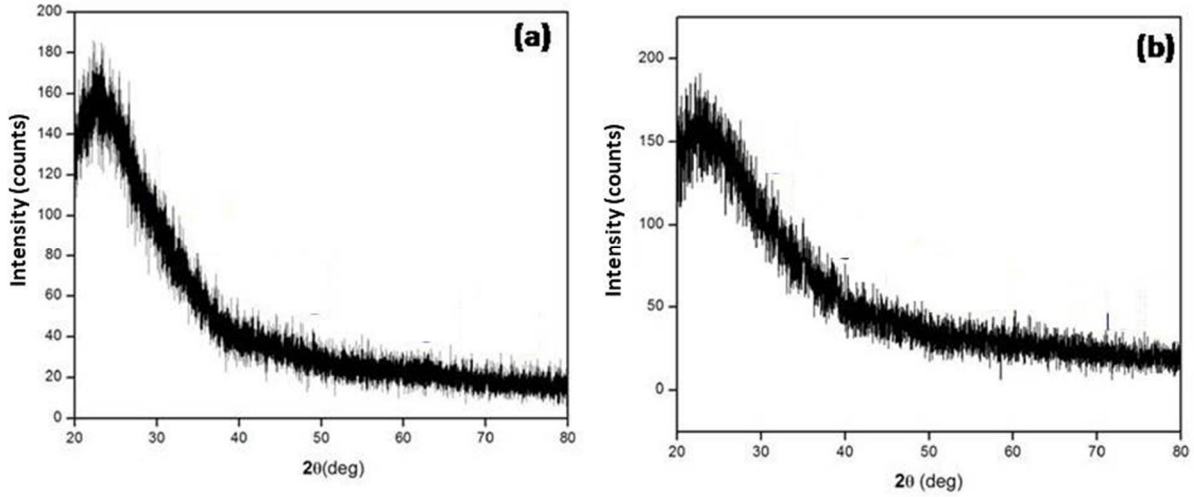

FIG. 2. XRD pattern of platinum-coated CuO nanostructured thin films.

3.2 Raman Spectra of CuO and Pt/CuO Nanostructured Thin Films

Raman spectroscopy, which is a sensitive probe to the local atomic arrangements and vibrations of the materials, has been also widely used to investigate the microstructural nature of the nanosized materials in general and CuO nanomaterial in particular. Raman scattering also provides useful information about the structures and bonds of materials. Raman scattering could help detect the existence of unintended phases, such as Cu_2O or Cu $(OH)_2$ or show the crystallinity of the product. Raman active normal modes of CuO are ΓRA = 4Au + 5Bu + Ag + 2Bg. Among these vibration modes, there are three acoustic modes (Au + 2Bu), six infrared active modes (3Au + 3Bg) and three Raman active modes (Ag + 2Bg). Three well known bands of CuO are Ag (278.81 cm^{-1}), Bg 1 (326 cm^{-1}) and Bg 2 (614.85 cm^{-1}) [5]. Fig.3 shows Raman spectra of CuO nanostructures prepared by SILAR method with different deposition

cycles. When increasing the deposition cycles to 40, the red shifts occur due to the phonon confinement effect in nanometer size materials. Multiphonon band of CuO nanostructures appears at a wave number of 1130 cm^{-1}. Fig. 4 shows the Raman spectra of platinum-coated CuO nanostructured thin films. The peaks observed at 328 cm^{-1}, 609.32 cm^{-1} and 1141.77 cm^{-1} are the different phonon modes of CuO. The peak at 2136 cm^{-1} provides strong evidence for the formation of platinum on CuO nanostructures.

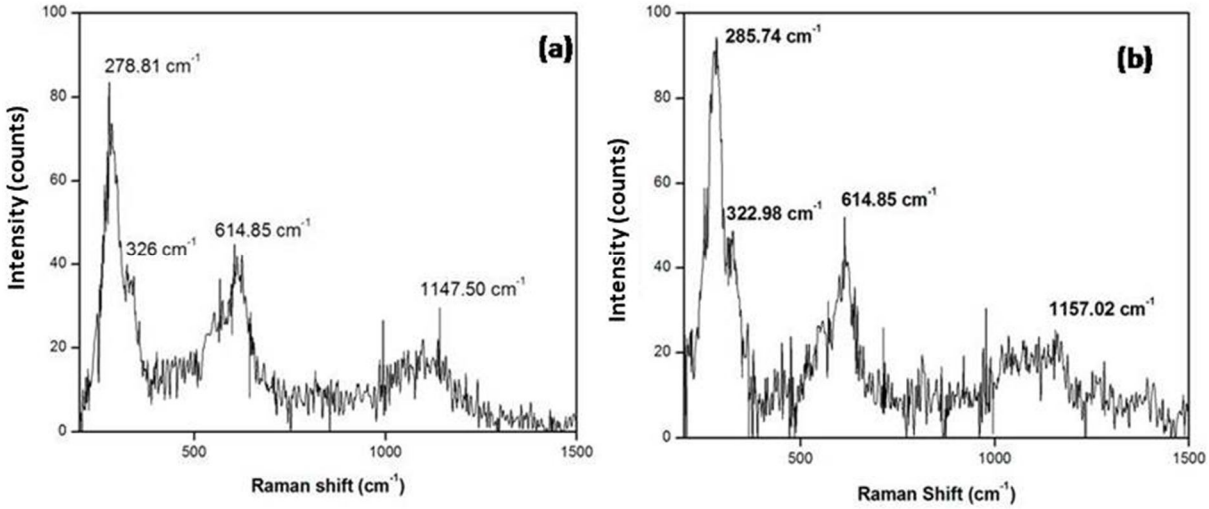

FIG. 3. Raman spectra of CuO nanostructured thin films prepared at a) 20 and b) 40 deposition cycles.

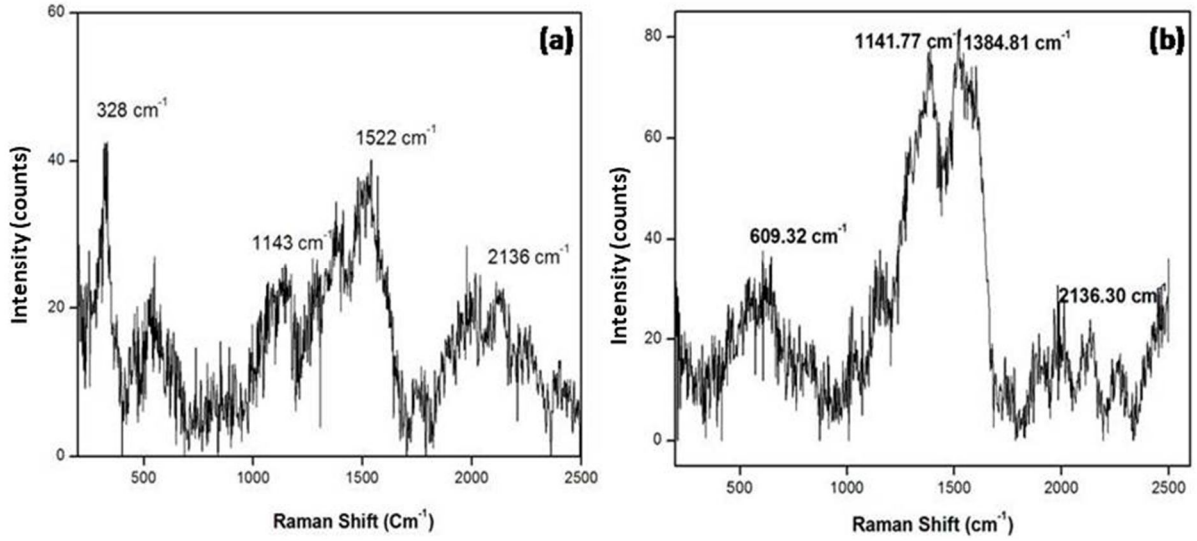

FIG. 4. Raman spectra of platinum-coated CuO nanostructured thin films.

3.3 Morphological Analysis

The morphology of designed CuO and Pt/CuO nanostructured thin films was determined by SEM and the prepared films are investigated in terms of shape, size and self-assembly of nanostructures. The morphology of CuO and Pt/CuO thin films for different cycles is shown in Fig. 5 and Fig. 6. All the micrographic images reveal that the nanostructures basically possess the petal shape and the petals are assembled together to form the floral structure. Initially, the floral structure is aggregated when platinum is coated over the CuO thin films. Grown nanopetals have been divided over the entire area of the film without any blowholes and assembled together to form a floral nanostructure, as shown in Fig. 5 and Fig. 6. The size of the flowers is around 200 nm.The self-assembled floral structure is due to the weak interaction by Van der Waals force.

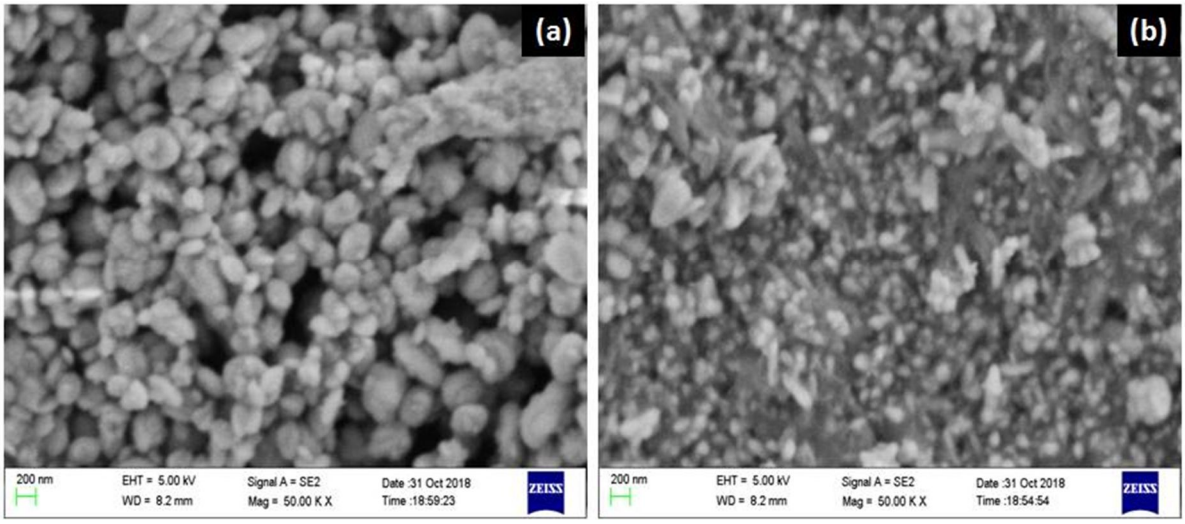

FIG. 5. SEM image of CuO nanostructured thin films prepared at a) 20 and b) 40 deposition cycles.

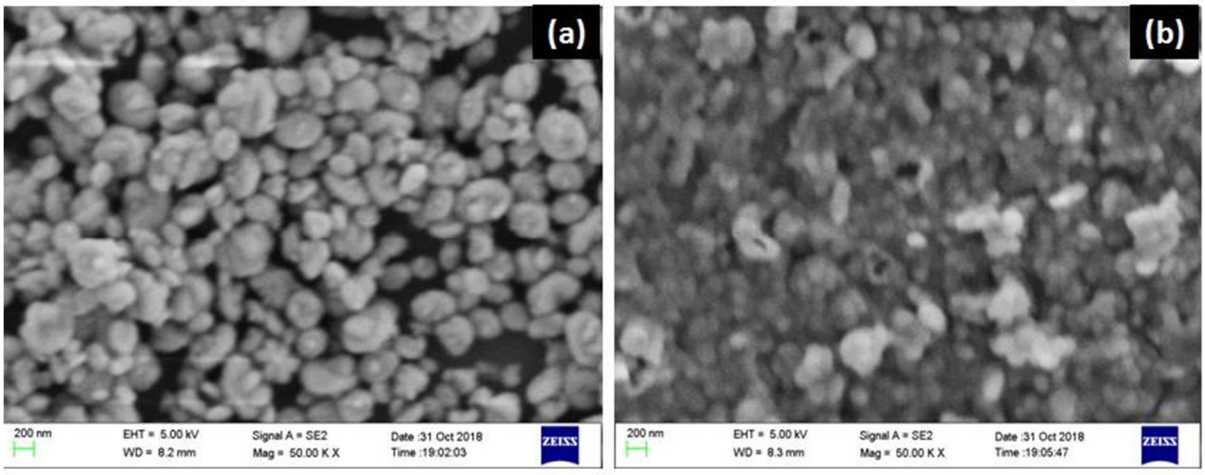

FIG. 6. SEM image of platinum-coated CuO nanostructured thin films prepared at a) 20 and b) 40 deposition cycles.

4. Conclusion

Copper oxide and platinum-coated copper oxide nanostructured thin films were prepared using the simple chemical method. Their structural properties have been studied using XRD and Raman spectroscopy. In XRD, the dominating intensity of the diffracted peaks (-111) and (111) reveals the improved crystallinity of CuO nanostructures. The average grain size estimated from XRD gives diameters in the range of 14 - 27 nm. Raman spectra explain the structural information of CuO and Pt/CuO nanostructured thin films, in which the peaks observed at 328 cm^{-1}, 609.32 cm^{-1} and 1141.77 cm^{-1} are the different phonon modes of CuO. The peak at 2136 cm^{-1} provides strong evidence for the formation of platinum on CuO nanostructures. Being more crystalline, CuO deposited thin films may be used in semiconductor devices and in optical fiber communication systems. The SEM micrograph confirms the floral morphology, which is basically composed of nano petals. From the observed morphology, it is observed that the deposited thin films, such as CuO and Pt/CuO, will give interesting applications to our society by being self-cleaning agents, photocatalysts, semiconductor devices, optical fibers, … etc.

References

[1] Forsyth, J.B. and Hull, S., J. Phys. Condens. Matter, 3 (1991) 5257.

[2] Zhang, Q., Zhang, K., Xu, D., Yang, G., Huang, H., Nie, F., Liu, C. and Yang, S., Progress in Materials Science, 60 (2014) 208.

[3] Ezenwa, I.A., Journal of Recent Sciences, 1 (2012) 46.

[4] Park, J.Y., Kwon, T.H., Koh, S.W. and Kang, Y.C., Bull. Korean Chem. Soc., 32 (4) (2011) 1331.

[5] Durig, J.R., TrAC Trends in Analytical Chemistry, 9 (10) (1990) IX.

[6] Cavusoglu, H. and Aydin, R., Superlattices and Microstructures, 128 (2019) 37.

[7] Bayansal, F., Gülen, Y., Sahin, B., Kahraman, S. and Çetinkara, H.A., Journal of Alloys and Compounds, 619 (2015) 378.

[8] Bayansal, F., Sahin, B., Yuksel, M., Biyikli, N., Cetinkara, H.A. and Guder, H.S., Journal of Alloys and Compounds, 566 (2013) 78.

[9] Tasdemirci, T.C., Electronic Materials Letters, 16 (2020) 239.

[10] Kovacı, H., Akaltun, Y., Yetim, A.F., Uzun, Y. and Çelik, Surface and Coatings Technology, 344 (2018) 522.

[11] Tian, X., Wang, Q., Zhao, Q., Qiu, L., Zhang, X. and Gao, S., Separation and Purification Technology, 209 (2019) 368.

[12] Rao, M.P., Sathishkumar, P., Mangalaraja, R.V., Asiri, A.M., Sivashanmugam, P. and Anandan, S., J. Environ. Chem. Eng., 6 (2018) 2003.

[13] Wang, D.G., Yan, B., Song, C.X., Ye, T. and Wang, Y.Q., J. Electron. Mater., 47 (2018) 744.

[14] Zgair, I.A., Alkhayatt, A.H.O., Muhmood, A.A. and Hussain, S.K., Optik, 191 (2019) 48.

[15] Daoudi, O., Qachaou, Y., Raidou, A., Nouneh, K., Lharch, M. and Fahoume, M., Superlattices and Microstructures, 127 (2018) 93.

[16] Shinde, S.K., Dubal, D.P., Ghodake, G.S., Kim, D.Y. and Fulari, V.J., Nano-Structures & Nano-Objects, 6 (2016) 5.

[17] Dhineshbabu, N.R., Rajendran, V., Nithyavathy, N. and Vetumperumal, R., Applied Nanoscience, 6 (6) (2015) 933.

[18] Shinde, S.K., Kim, D.Y., Ghodake, G.S., Maile, N.C., Kadam, A.A., Lee, D.S., Rath, M.C. and Fulari, V.J., Ultrasonics Sonochemistry, 40 (2018) 314.

[19] Prabu, R.D., Valanarasu, S., Ganesh, V., Shkir, M., AlFaify, S., Kathalingam, A., Srikumar, S.R. and Chandramohan, R., Materials Science in Semiconductor Processing, 74, (2018) 129.

[20] Nesa, M., Sharmin, M., Hossain, K.S. and Bhuiyan, A.H., Journal of Materials Science: Materials in Electronics, 28 (17) (2017) 12523.

[21] Gülen, Y., Bayansal, F., Şahin, B., Çetinkara, H.A. and Güder, H.S., Ceramics International, 39 (6) (2013) 6475.

[22] Jundale, D.M., Joshi, P.B., Sen, S. and Patil, V.B., Journal of Materials Science: Materials in Electronics, 23 (8) (2012) 1492.

[23] Gobbiner, C.R., Dillip, G.R., Joo, S.W. and Kekuda, D., Ceramics International, 44 (14) (2018) 16984.

Volume 14, Number 5, 2021. pp. 425-435

Jordan Journal of Physics

ARTICLE

Effect of ZrO_2 Nanofiller on the Physical Properties of Epoxy Composites: Mechanical, Thermal and Dielectric

N. Annlin Bezy[a], **A. Lesly Fathima**[b], **S. Sebastiammal**[b] and **S. Virgin Jeba**[b]

[a] *Research Scholar (Reg.No:20213042132006), Department of Physics, Holy Cross College (Autonomous), Nagercoil-629004, Tamil Nadu, India.*

[b] *Research Department of Physics, Holy Cross College (Autonomous), Nagercoil-629004, Tamil Nadu, India.*

(Affiliated to Manonmaniam Sundaranar University, Abishekapatti, Tirunelveli-627012, Tamil Nadu, India).

Doi: **https://doi.org/10.47011/14.5.4**

Received on: 01/05/2020; *Accepted on: 24/05/2021*

Abstract: In this present work, Zirconia nanoparticles were prepared by precipitation method, Zirconium Oxychloride ($ZrOCl_2.8H_2O$) and ammonia (NH_3) as starting materials. The synthesized Zirconia nanoparticles were characterized by XRD and the grain size in nanoscale was confirmed. The sheets of neat epoxy resin and epoxy with addition of ZrO_2 nanoparticles are primed by solution casting method. The structures of epoxy polymer and hardener were found out using FTIR analysis. The thermal properties were analyzed using Thermo Gravimetric Analysis (TGA) and Differential Thermal Analysis (DTA). Thermo gravimetric analysis has been employed to investigate the thermal characteristics and their mode of thermal degradation. Differential thermal analysis has been used to determine the glass transition temperature of epoxy nanocomposites. The mechanical properties like tensile and flexural studies were analyzed and thus influences of nanofiller loading on these parameters were found to be very low.

Keywords: Epoxy, ZrO_2 nanoparticles, Nanocomposites, Thermal stability, Dielectric properties, Tensile strength, Flexural strength.

Introduction

Polymer nanocomposites have attracted increasing attention in the last decade because of their significant improvement of physical and chemical properties over the matrix polymers. The effects of nanofillers on these properties have been extensively observed to make nanocomposites for application purpose. The addition of just a few percent by weight of nanofillers can result in significant enhancement in dielectric, thermal and mechanical properties. The incorporation of metal oxide nanoparticles with polymer is approached to improve the mechanical strength [1–6]. The effects of inorganic fillers on the properties of composites strongly depend on filler size and shape, type of particles and the degree of dispersion [7-8]. Various nanoscale fillers, including metal oxides, montmorillonite and calcium carbonate, have been reported to enhance the mechanical properties, thermal stability, gas barrier properties, electrical properties and flame retardancy of the polymer matrix [9-11]. Among various metal oxide fillers, nano-sized zinc oxide (ZnO), zirconium oxide (ZrO_2), titanium dioxide (TiO_2) and cerium oxide (CeO_2) fillers have attracted considerable attention because of their unique physical properties as well as their low cost and extensive applications in diverse areas [12-15]. Here, the purpose of study is to evaluate the physical properties of epoxy resin with Zirconia nanoparticles.

Corresponding Author: A. Lesly Fathima **Email**: leslysat@gmail.com

Experimental Part

X-Ray Diffraction

X-ray diffraction (XRD) was a spectroscopic method which has been used in the structure determination of crystalline materials. X-ray diffraction (XRD) of ZrO_2 nanoparticles was carried out on a XPERT – PRO diffractometer system with monochromated CuK_α (1.5406 Å) radiation working at 40 kV/30 mA. The grain size of ZrO_2 was calculated by De-bye Scherrer formula:

$$D = K\lambda/\beta cos\theta$$

where:

K is a constant;

λ is the wave length used;

β is the full width half maximum;

θ is the angle of diffraction.

Fourier Transformation Infrared Spectroscopy

Fourier Transform Infrared (FTIR) spectroscopy is used to identify organic, polymeric and in some cases inorganic materials. The FTIR analysis method uses infrared light to scan test samples and observe chemical properties. FTIR measurements for the samples were performed in SHIMADZU type IR Affinity-spectrophotometer in the range of 4000 – 400 cm^{-1}. The mode used in the FTIR characterization is transmission.

Thermal Analysis

The thermal properties were analyzed using differential scanning calorimetry and thermogravimetric analysis. Thermal stability of the nanocomposites was studied using thermogravimetric analysis (TGA) in SIINT 6300 thermogravimetric analyzer temperature ranges from 25°C to 1000°C with the heating rate of 10°C/min. Powder sample is used for thermal analysis.

Electrical Analysis

Dielectric spectroscopy was based on the phenomena of electrical polarization and electrical conduction in materials. The most common mechanisms of polarization will occur at high frequencies (10^3 Hz - 10^{15} Hz), while at very low frequencies (10^{-3} Hz – 10^3 Hz), DC conduction will become significant. Thus, dielectric spectroscopy was also well suited for the determination of both AC and DC conductivity of materials. In order to understand the influence of ZrO_2 on the dielectric property of the composites, the permittivity and dissipation factor of the composites were investigated. In the present work, the dielectric spectroscopy (DS) using the instrument HIOKI 3532-50 LCR Hitester, over a frequency range of 10^1 – 10^6 Hz, at three temperatures 50°C, 100°C and 150°C were found. For testing, the sample was cut into the dimensions of 7.5 X 6 X 4 mm. The applied voltage was set to 1V and during all the measurements, room temperature was maintained.

Mechanical Analysis

Tensile test and flexural strength test of developed sheets are performed using mechanical analyzer in tensile mode in accordance with the ASTM D-638 test standard and flexural mode with ASTM D-790 test standard, respectively. Before testing, the rectangular samples of fixed size are cut out from sheets using a clean razor blade and the upper side of cut sample for tensile test is polished to make flat surface. And the edges of the sample are polished by sand paper of a mesh of 1200. ASTM D-638 is a testing specification that determines the in-plane tensile properties of polymer matrix composite materials reinforced by high-modulus fibres. A tensile test measures the resistance of a material to a static or slowly applied force. ASTM D 790 is a method of measuring the flexural properties of plastic by setting a test bar across two supports and pushing it down in the middle until it breaks or bends at a specified distance. Flexural modulus is a measure of stiffness or rigidity.

Materials and Method

Materials

Zirconium oxychloride ($ZrOCl_2.8H_2O$) and ammonia (NH_3) purchased from Sigma Aldrich were used as starting materials for the synthesis of ZrO_2 nanoparticles. ARALDITE epoxy resin (LY 556) and hardener (HY 951) were taken as the materials for the development of polymer sheets.

Synthesis of ZrO_2 Nanoparticles

ZrO_2 nanoparticles were prepared by the precipitation method. Zirconium hydroxide precipitation ($Zr(OH)_4$) was obtained by adding

NH_3 solution drop-wise into the aqueous solution of 0.2M $ZrOCl_2.8H_2O$ at room temperature until the desired pH of 10 was reached. Zirconium hydroxide mixture was then dried in an oven at 100°C for 12 hours. Zirconia nanoparticles were obtained through calcination at 600°C for 2 hours.

Preparation of Epoxy/ ZrO_2 Nanocomposites

Epoxy resin and hardener were used in this study to develop pure and ZrO_2 nanofiller imposed epoxy nanocomposites for different ZrO_2 weight percentages (1, 3, 5 and 7) wt %. The method used in preparation of epoxy/ZrO_2 nanocomposite sample is solution casting. For pure sample, epoxy resin of 60g and hardener of 6g were poured separately in two beakers. To remove the air bubbles, both needed to be ultrasonicated for 30 minutes. After the completion of this process, the hardener was added to the epoxy resin and mixed by hand stirring. Then, it was ultrasonicated to remove air bubbles generated during the mixing process. After degassing, the mixture was poured into a metal mould. The metal mould was kept undisturbed for 1 hour at room temperature. Finally, the sample was cured by keeping the mould in an oven at 100°C for 2 hours. Thus, neat epoxy sheet was obtained. For epoxy/ZrO_2 nanocomposites, 1wt% ZrO_2 nanofillers were added with the epoxy resin and the same procedure was repeated for 3wt %, 5wt % and 7wt % ZrO_2 added epoxy nanocomposites [16-18]. The photograph of developed polymer sheets is shown in Fig.1.

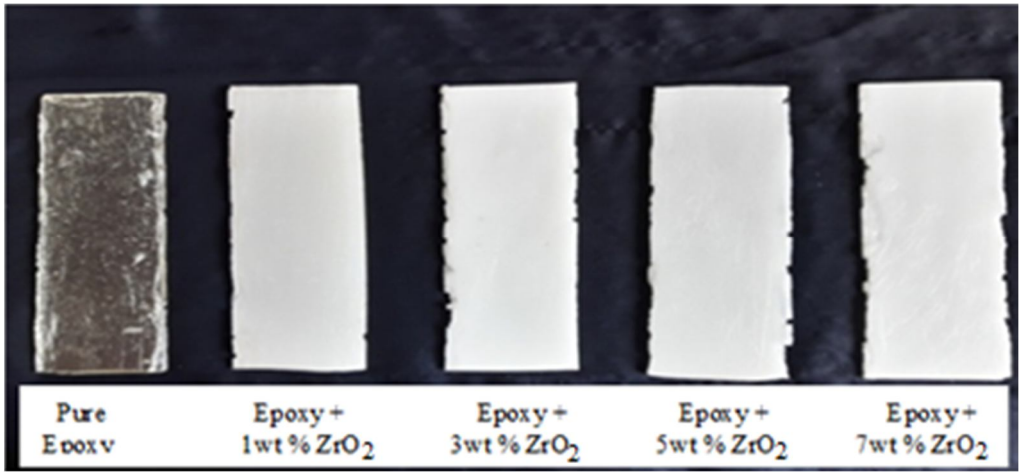

FIG. 1. Photograph of pure and ZrO_2-imposed nanocomposite sheets.

Results and Discussion

Powder X- ray Diffraction Analysis

PXRD pattern of synthesized Zirconia nanoparticles is reported in Fig.2. The XRD pattern of ZrO_2 nanoparticles is found to exhibit many diffraction peaks and of that, $(\bar{1}11)$ reflection plane is very predominant and has high intensity. The crystallite size of synthesized ZrO_2 is found to be 36.21nm and this confirms that the prepared ZrO_2 particles are in nanoscale. The X-ray diffraction spectrum confirms that the pure ZrO_2 nanopowder is in monoclinic crystalline phase. The data obtained is in good agreement with standard JCPDS file no 89-9066.

Fourier Transform Infrared Analysis

Fourier Transform Infrared spectroscopy was used to characterize the prepared pure epoxy and ZrO_2-imposed epoxy nanocomposite samples. The FTIR spectrum is shown in Fig.3 and assignments for prepared samples are listed in Table 1.

The structures of LY 556 epoxy resin and HY 951 hardener were confirmed by FTIR spectral analysis. In the FTIR spectrum of pure epoxy, the band at 3431 cm^{-1} corresponds to the vibration of hydroxyl (OH) group. The band at 3037 cm^{-1} corresponds to the CH stretching vibration in aromatic ring. The peaks at 2973 cm^{-1} and 2933 cm^{-1}indicate the asymmetric C-H stretching of CH_3 and CH_2 groups, respectively. The strong peaks at 1572 cm^{-1}, 1510 cm^{-1} and 1425 cm^{-1} indicate the C-C stretching vibration in aromatic ring. The asymmetric deformation of CH_2 produces absorption band at 1297 cm^{-1}. The asymmetric stretching of C-O in aromatic and aliphatic groups produces absorption bands at 1247 cm^{-1} and 1182 cm^{-1}, respectively. The asymmetric stretching mode of C-O-C vibration

appears at 1040 cm^{-1}. Absorption peak at 922 cm^{-1} corresponds to epoxide ring vibrations. The strong absorption peak at 828 cm^{-1} indicates C-H out-of-plane deformation in aromatic rings. The appearance of the bands at 649 cm^{-1} and 559 cm^{-1} indicates the bending vibrations of N-H and C-H, respectively. The sharpness and intensity vary for different weight percentages of ZrO_2 nanofiller-added epoxy nanocomposites. A slight shift in absorption bands is observed for ZrO_2 nanofiller-added epoxy systems. This is due to strong attraction of ZrO_2 nanoparticles with epoxy [19].

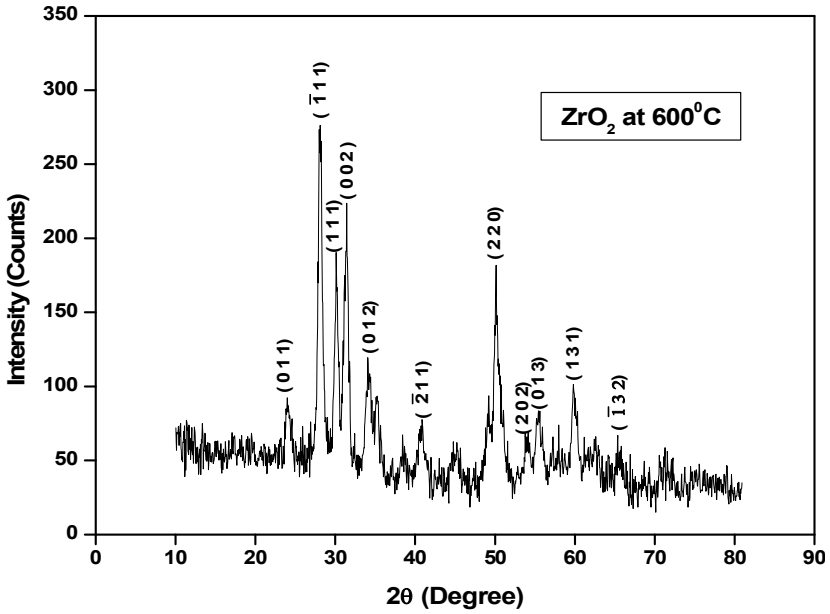

FIG. 2. XRD pattern of ZrO_2 nanoparticles.

TABLE. 1. Frequency assignments of pure and ZrO_2-epoxy nanocomposites.

Wave Number (cm^{-1})					Assignments
Pure Epoxy	Epoxy + 1wt % ZrO_2	Epoxy + 3wt % ZrO_2	Epoxy + 5wt % ZrO_2	Epoxy + 7wt % ZrO_2	
3431	3416	3433	3430	3419	O-H Stretching
3037	3036	3035	3032	3037	C-H Stretching in aromatics
2973	2971	2975	2975	2971	Asymmetric C-H Stretching of CH_3 group
2933	2932	2937	2935	2935	Asymmetric C-H Stretching of CH_2 group
1572	1572	1571	1571	1572	C-C Stretching vibration in aromatics
1510	1510	1510	1511	1510	
1425	1426	1424	1425	1426	
1297	1297	1297	1297	1297	Asymmetric CH_2 deformation
1247	1247	1247	1247	1247	Asymmetric aromatic C-O stretching
1182	1182	1182	1182	1182	Asymmetric aliphatic C-O stretching
1040	1039	1041	1042	1039	Stretching vibration of C-O-C
922	921	922	922	921	Epoxide ring vibrations
828	828	827	828	828	C-H out-of-plane deformation in aromatics
649	649	649	649	649	Bending vibration of NH
559	559	560	560	559	Bending vibration of C-H

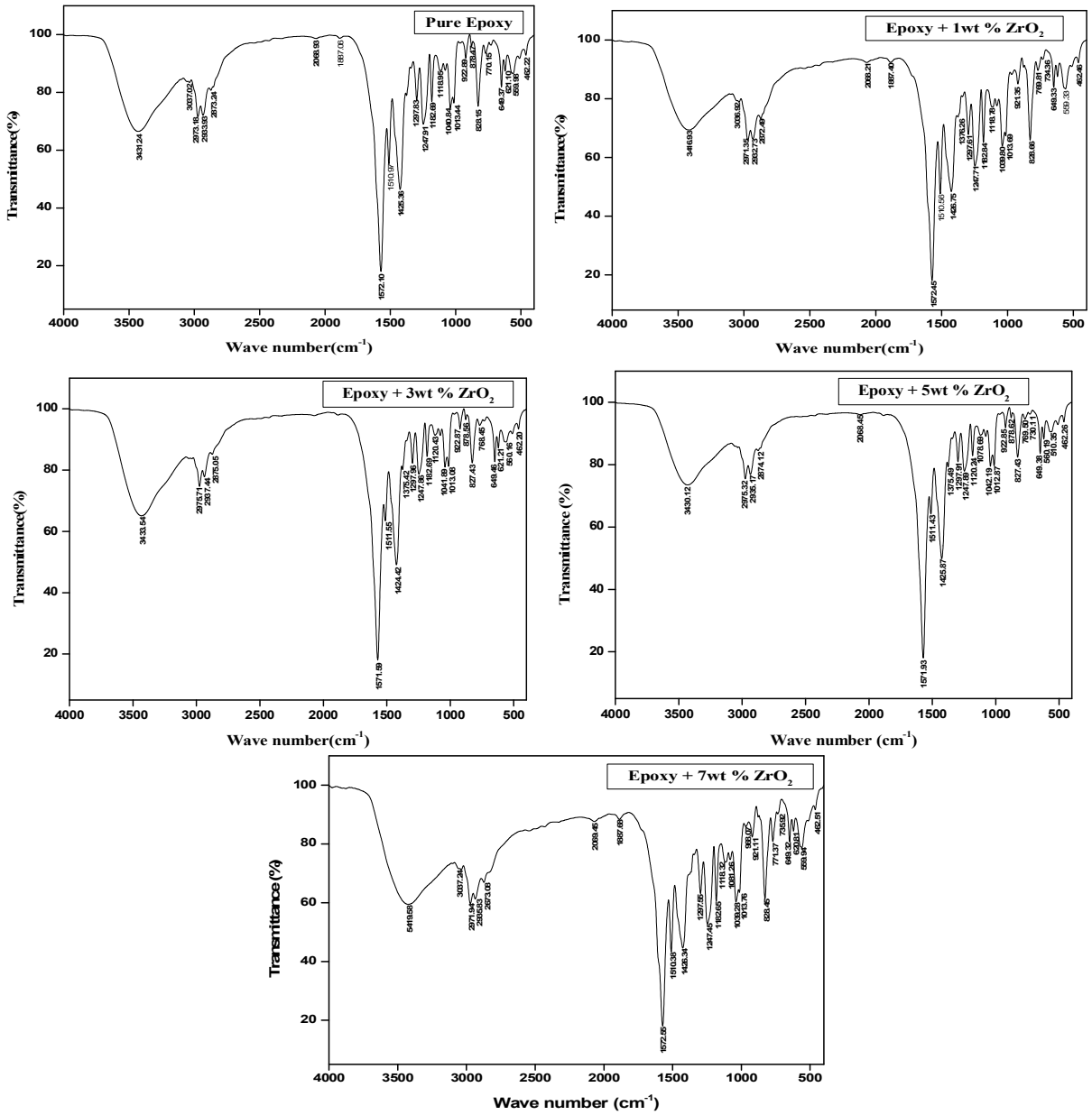

FIG. 3. FTIR spectra of pure epoxy and ZrO_2-epoxy nanocomposites.

Thermal Analysis

Thermo Gravimetric Analysis (TGA)

The thermal properties were analyzed using differential scanning calorimetry and thermogravimetric analysis. The thermo gravimetric curves are shown in Fig.4.

Both neat epoxy and ZrO_2/epoxy systems have similar decomposition profiles and the degradation takes place in two stages. Initial weight loss (weight started at 100°C) was observed in the thermograms corresponding to evaporation of water molecules from polymer samples [20]. The second step weight loss occurs due to the decomposition of polymer itself. As evident from thermograms, the nano-filler has a significant effect on thermal stability of polymers. Table 2 shows the TGA data of pure epoxy and ZrO_2-epoxy nanocomposites.

The relative thermal stability of epoxy nanocomposites has been evaluated by comparing the decomposition temperatures at different percentage weight losses. The thermal stability of the ZrO_2 nanofiller-added nanocomposites is observed to be slightly decreased as compared to that of neat epoxy. This may result from the spatial obstruction of nanoparticles on the formation of high cross-linked molecular structure of epoxy or increased free volume fractions in the polymer nanocomposites [21].

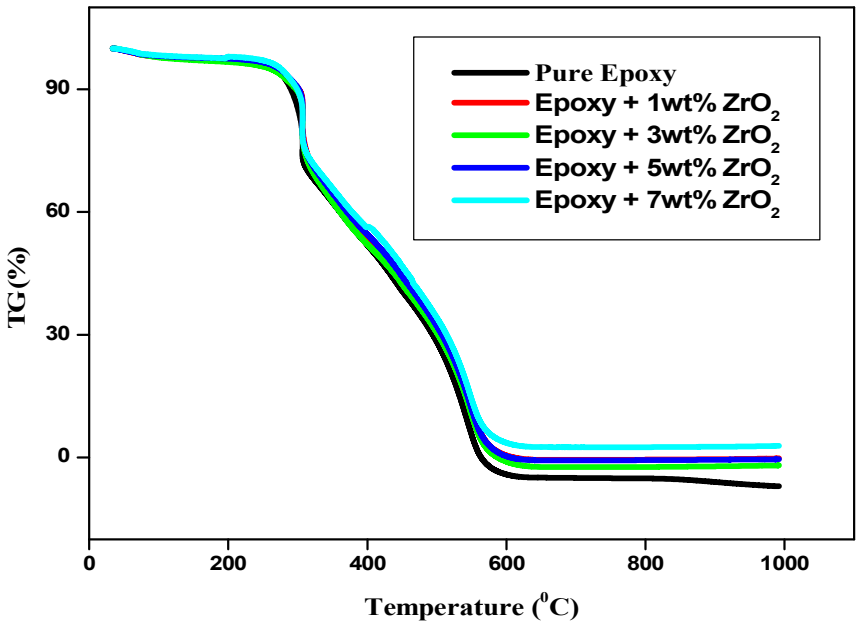

FIG. 4. Thermogravimetric curve of pure and ZrO_2-added epoxy nanocomposites.

TABLE. 2. TGA data of pure and ZrO_2-doped epoxy nanocomposites.

Sample	T_1 (T_{d1}°C)	T_2 (T_{d2}°C)
Pure Epoxy	281	507
E + 1wt%	275	500
E + 3wt%	273	489
E + 5wt%	271	509
E + 7wt%	268	504

Differential Thermal Analysis (DTA)

The DTA curves of pure and ZrO_2 imposed epoxy nanocomposites are presented in Fig. 5. It shows the effect of ZrO_2 nanoparticles on the glass transition temperature of the nanocomposites. The glass transition temperatures of pure epoxy and ZrO_2-imposed epoxy nanocomposites were listed in Table 3.

TABLE 3. Glass transition temperature of pure and ZrO_2-embedded epoxy nanocomposites.

Sample	Glass Transition temperature (T_g°C)
Neat Epoxy	71.5
E+1wt%	69.7
E+3wt%	70.7
E+5wt%	69.3
E+7wt%	70.2

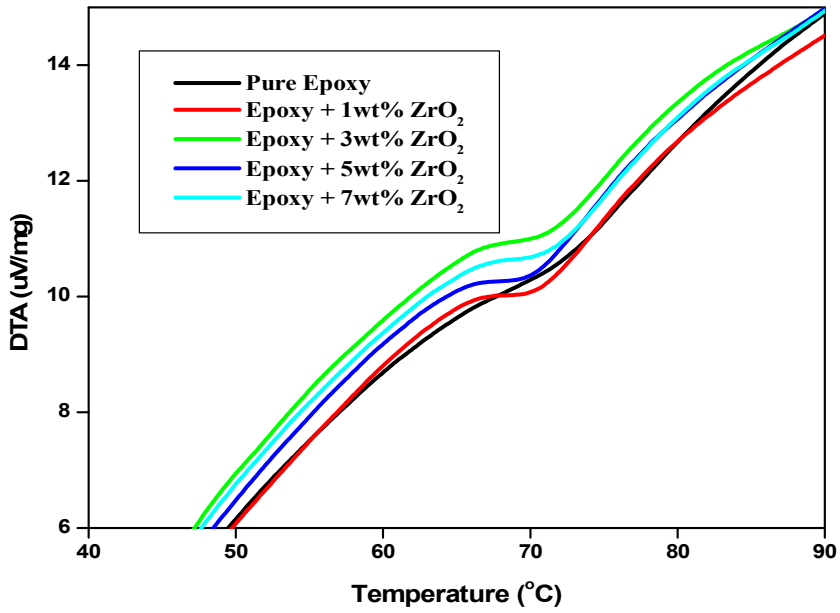

FIG. 5. DTA curves of pure and ZrO_2-added nanocomposites.

It can be ascertained from Fig. 5 that for the filler loadings, the glass transition temperature is lower than that of unfilled epoxy. The changes in T_g are due to the effect of nanoparticles only. Few studies on polymer nanocomposites have suggested that polymer nanoparticle interactions actually lead to the formation of more than one nanolayer around the nanoparticles [22].

In addition to the formation of the immobile polymer close to the particle, another polymer layer with a thickness slightly more than that of the immobile layer forms over it. The polymer segments in this extended layer are reported to be loosely bound and they relax faster causing a reduction in the nanocomposites' glass transition temperature [23].

Electrical Analysis

The variations of dielectric constant with temperature and frequency for the epoxy nanocomposites having ZrO_2 nanofillers at different filler concentrations are shown in Figs. 6-7.

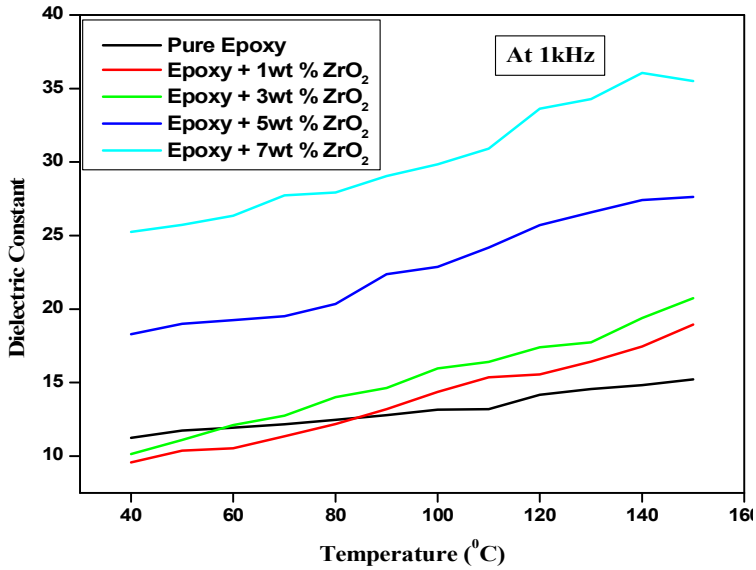

FIG. 6. Dielectric constant *vs*. temperature at 1 kHz.

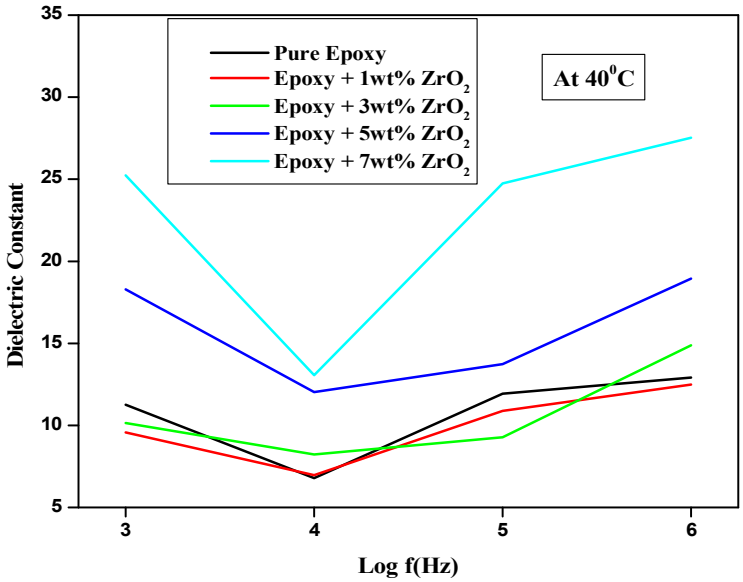

FIG. 7. Dielectric constant *vs*. frequency at 40^0C.

From Fig. 6, it can be seen that the dielectric constant increases with the increase in temperature for all the tested nanocomposites. This dependence is observed for pure and all the four filler concentrations. At low temperatures, the orientational mode cannot contribute to polarization. This leads to a lower dielectric constant at low temperatures. From Fig.7, the dielectric constant of neat and ZrO_2-imposed epoxy nanocomposites increases with increasing

frequency above 10^4 Hz. At lower frequencies of applied voltage, all the free dipolar functional groups in the epoxy chain can orient themselves resulting in a higher ε_r value at these frequencies. Further increasing frequency, the ε_r value increases. ZrO_2 displays strong ionic polarization due to Zr^{4+} and O^{2-} ions and therefore has a high value of dielectric constant [24]. In this study, it is found that 7wt% ZrO_2 nanofiller-added epoxy system has high dielectric constant.

Temperature at 1kHz, Frequency at 40^{0}C

From Fig. 8, it can be seen that the dielectric loss increases with the increase in temperature for all the tested samples. The dielectric loss values for ZrO_2 nanofiller-added epoxy nanocomposites are less than those of unfilled epoxy. From Fig. 9, pure and ZrO_2 nanofiller-added epoxy nanocomposites show that the values of dielectric loss with 1wt%, 3wt%, 5wt% and 7wt% filler concentrations are less than those of unfilled epoxy. Dielectric loss depends on the electrical conductivity in the epoxy composites. The electrical conductivity in turn depends on the number of charge carriers in the material, the relaxation time of the charge carriers and the frequency of the applied electric field. This observation is probably due to the presence of a significant number of nanoparticles in the system which influences the electrical conductivity mechanism in the nanocomposites [24].

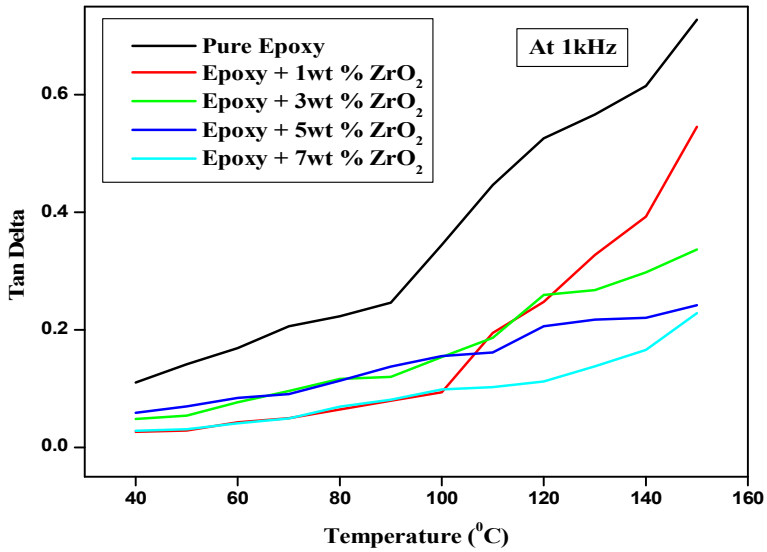

FIG. 8. Variation of tan delta *vs.* temperature at 1 kHz.

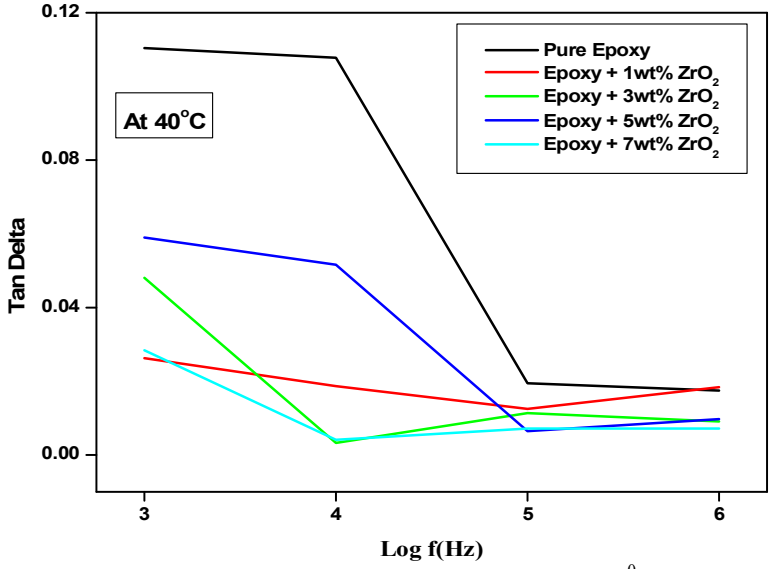

FIG. 9. Variation of tan delta *vs.* frequency at 40^{0}C.

From Fig.10, it can be seen that the AC conductivity increases with the increase in temperature for all the tested nanocomposites. Pure epoxy and ZrO_2-imposed epoxy nanocomposites show different dielectric behaviors, depending on the frequency and on the filler concentration. In our present study, the dielectric behavior is very little influenced by the type of filler and filler concentration.

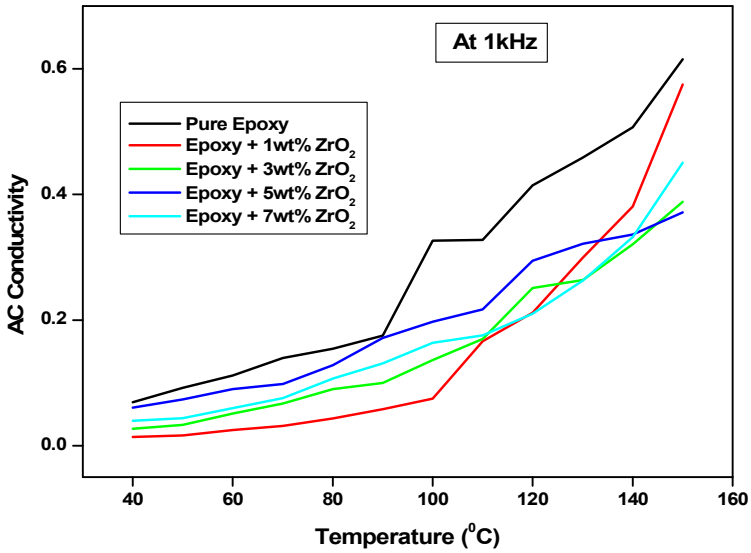

FIG. 10. Variation of AC conductivity *vs*. temperature at 1 kHz.

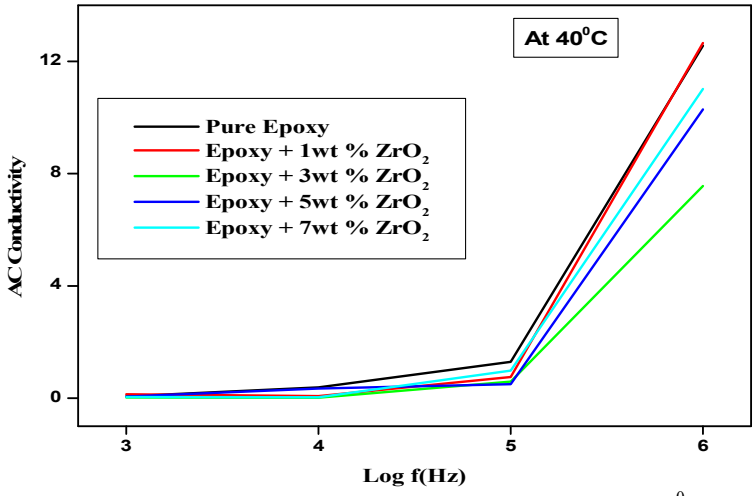

Fig. 11. Variation of AC Conductivity *vs*. Frequency at 40^0C.

Mechanical Analysis

Values of tensile strength and flexural strength for pure and ZrO_2 nanofiller (3 wt% and 5wt%) - imposed epoxy nanocomposites are shown in Table 4. It shows that the neat epoxy has maximum tensile strength. For ZrO_2 nanofiller (3wt% and 5wt%) - added epoxy nanocomposites, the tensile strength and flexural strength decreased when compared with neat epoxy. Thus, the results indicate that there may be agglomeration of nanoparticles owing to less interaction with resin [25]. Table 4 shows the values of tensile strength and flexural strength of pure epoxy and nanocomposites.

TABLE 4. Tensile strength and flexural strength.

Sample	Tensile strength (MPa)	Flexural strength (MPa)
Pure Epoxy	25.5	79.6
Epoxy + 3wt% ZrO_2	24.5	43.5
Epoxy + 5wt% ZrO_2	21.0	30.8

Conclusion

ZrO_2 nanoparticles were prepared by precipitation method. The prepared ZrO_2 nanoparticles were subjected to XRD characterization. The grain size of ZrO_2 was calculated by De-bye Scherrer formula. The grain size of synthesized ZrO_2 is found to be 36.21nm and this confirms that the prepared ZrO_2 particles are in nanoscale. Neat and ZrO_2 nanoparticles-imposed epoxy composites were synthesized by solution casting method. FTIR study proved the occurrence of epoxy and amine hardener and its interaction with ZrO_2 nanoparticles. The sharpness and intensity of the peak vary for different weight percentages of ZrO_2 nanofiller-added epoxy nanocomposites. Thermo gravimetric analysis has been employed to investigate the thermal characteristics and their mode of thermal degradation. The TGA thermograms of epoxy/ZrO_2 nanocomposites' systems exhibit lower decomposition temperature behaviours compared to neat epoxy. The glass transition temperature was determined using DTA curve and it was observed that the glass transition temperature of epoxy/ZrO_2 polymer nanocomposites decreases when compared with neat epoxy. The thermal stability was not enhanced in epoxy/ZrO_2 polymer nanocomposites when compared with neat epoxy.Dielectric properties, such as dielectric loss and dielectric constant, are evaluated to determine the electrical conductivity of prepared polymer samples. Dielectric results showed that it is a frequency-dependent parameter. For ZrO_2 nanofiller-added composites (3wt% and 5wt%), the tensile strength decreases compared with neat epoxy. Flexural strength is higher for neat epoxy when compared with ZrO_2-imposed epoxy system. This indicates that there may be agglomeration of nanoparticles owing to less interaction with resin.

References

[1] Majid, M., Hassan, E.-D., Davoud, A. and Saman, M., Composites Part B: Engineering, 42 (7) (2011) 2038.

[2] Sun, T., Chen, F., Dong, X. and Han, C.C., Polymer, 49 (11) (2008) 2717.

[3] Zhang, Q.X., Yu, Z.Z., Xie, X.L. and Mai, Y.W., Polymer, 45 (17) (2004) 5985.

[4] Luyt, A.S., Dramicanin, M.D., Antic, Z. and Djokovic, V., Polymer Testing, 28 (3) (2009) 348.

[5] Saminathan, K., Selvakumar, P. and Bhatnagar, N., Polymer Testing, 27 (3) (2008) 296.

[6] Zhao, H. and Li, R.K.Y., Polymer, 47 (9) (2006) 3207.

[7] Zaman, H.U., Hun, P.D., Khan, R.A. and Yoon, K.-B., Journal of Reinforced Plastics and Composites, 31 (5) (2012) 323.

[8] Chan, C.-M., Wu, J., Li, J.-X. and Cheung, Y.-K., Polymer, 43 (10) (2002) 2981.

[9] Galgali, G., Agarwal, S. and Lele, A., Polymer, 45 (17) (2004) 6059.

[10] Alexandre, M. and Dubois, P., Mater. Sci. Eng.: R: Reports, 28 (1-2) (2000) 1.

[11] Motha, K., Hippi, U., Hakkala, K, Peltonen, M., Ojanperä, V., Löfgren, B. and Seppälä, J., J. Appl. Polym. Sci., 94 (3) (2004) 1094.

[12] Chatterjee, A., J. Appl. Polym. Sci., 116 (6) (2010) 3396.

[13] Li, Y.J., Duan, R., Shi, P.B. and Qin, G.G., J. Crystal Growth, 260 (3-4) (2004) 309.

[14] Zeng, D.W., Xie, C.S., Zhu, B.L., Song, W.L. and Wang, A.H., Mater. Sci. Eng.: B, 104 (1-2) (2003) 68.

[15] Yang, Y., Chen, H., Zhao, B. and Bao, X., J. Crystal Growth, 263 (1-4) (2004) 447.

[16] Sumi, E., Virgin Jeba, S. and Lesly Fathima, A., Archives of Physics Research, 6 (1) (2015) 20.

[17] Annlin Bezy, N. and Lesly Fathima, A., International Journal of Engineering Research and General Science, 3 (5) (2016) 143.

[18] Lesly Fathima, A., International Journal of Engineering and General Science, 5 (2) (2017) 10.

[19] Mahulikar, P.P., Jadhav, R.S. and Hundiwale, D.G., Iranian Polymer Journal, 20 (5) (2011) 367.

[20] Liu, Y.L., Hsu, C.Y., Wei, W.L. and Jeng, R.J., Polymer, 44 (18) (2003) 5159.

[21] Zhu, J., Wei, S., Ryu, J., Sun, L., Luo, Z. and Guo, Z., ACC Appl. Mater. Interfaces, 2 (7) (2010) 2100.

[22] Gupta, A.K., Balakrishnan, V.R. and Tiwary, S.K., International Journal of Polymer Technology, 1 (2-3) (2009) 181.

[23] Tsagaropoulos, G. and Eisenberg, A., Macromolucules, 28 (18) (1995) 6067.

[24] Singha, S. and Thomas, M.J., IEEE Transaction on Dielectrics and Electrical Insulation, 15 (1) (2008) 12.

[25] Merad, L., Benyousef, B., Abadie, M. and Charless, J.P., Journal of Engineering and Applied Sciences, 6 (3) (2011) 205.

Volume 15, Number 1, 2022. pp. 437-444

Jordan Journal of Physics

ARTICLE

Albumen-assisted Synthesis of Nanocrystalline Nickel Ferrite Photocatalyst

P. Aji Udhaya[a,b], **M. Meena**[c], **M. Abila Jeba Queen**[a], **M. Mary Freeda**[a] and **T. Regin Das**[d]

[a] *Department of Physics, Holy Cross College, Nagercoil, Affiliated to Manonmaniam Sundaranar University, Abishekapatti, Tirunelvel-627012, India.*

[b] *Research Scholar, Reg. No. 18123152132038, Department of Physics, S.T. Hindu College, Nagercoil, Affiliated to Manonmaniam Sundaranar University, Abishekapatti, Tirunelvel-627012, India.*

[c] *Department of Physics, S.T. Hindu College, Nagercoil, Affiliated to Manonmaniam Sundaranar University, Abishekapatti, Tirunelvel-627012, India.*

[d] *Department of Physics, Lekshmipuram Arts and Science College, Neyyoor, Nagercoil, India.*

Doi: **https://doi.org/10.47011/14.5.5**

Received on: 01/05/2020; *Accepted on: 15/09/2020*

Abstract: As a simple step to remove the polluting dyes in aqua ecosystem, $NiFe_2O_4$ nanoparticles well known for their ferromagnetic properties, low conductivity and high electrochemical stability were prepared by simple auto combustion method using egg white as fuel *via* green synthesis route. The structural, morphological and magnetic properties of prepared $NiFe_2O_4$ was analyzed. The desirable phase purity of the prepared spinel ferrite was deliberated by X-ray Diffractometer (XRD), Fourier Transform Infrared Spectrometer (FTIR), Scanning Electron Microscopy (SEM), Energy Dispersive and Vibrating Sample Magnetometer (VSM). XRD predicts the phase formation, particle size and lattice parameter of the spinel ferrite. The FTIR spectrum confirms the ferrite structure. The morphological and elemental analysis was made using SEM and EDAX. The hysteresis curve reveals the magnetic properties, such as remanence magnetization (Mr), coercivity (H_c) and saturation magnetization (M_s). The photocatalytic efficiency of the synthesized samples was determined from degradation of methylene blue dye. The whole process was monitored using spectrophotometer at regular intervals of time. The maximum photocatalytic degradation efficiency for $NiFe_2O_4$ is around 95.6 %.

Keywords: $NiFe_2O_4$, Ferrite, Green synthesis, Egg white, Combustion, Photocatalyst.

1. Introduction

Wastewater management in developing countries is a major problem due to various industrial processes that meet human needs. Dyeing and pigment industries are of major environmental concern among the various industries, as wastewater includes several non-biodegradable organic colors. From textiles to food, dyes are widely used by humans. Methylene blue is an organic dye that is synthetic and water soluble. It is widely used as a colorant in textiles, paper, plastics, cosmetics, leather, food and many other industries, leading to large dye effluent discharges. If the effluents are not treated properly, they become a serious environmental problem that affects the flora and fauna, as well as human health. Methylene blue dye can irradiate the eyes and skin and damage the respiratory, reproductive, and nervous systems through carcinogenic actions. In

Corresponding Author: P. Aji Udhaya **Email**: ajiudhaya@gmail.com

addition, Methylene blue is dangerous even at very low concentrations and therefore, methylene blue effluent treatment becomes more vital [1].

For the treatment of methylene blue-containing water, techniques such as photocatalytic degradation, ozonation, electrochemical method, Fenton process and so on were employed. In the present day, photocatalysis is preferred over other methods of treatment for color degradation, as light irradiation generates pairs of electrons and holes on a semiconductor. The photogenerated hole (h^+) reacts in aqueous solution with H_2O and OH^- to form hydroxyl radical (OH^-), which is a key and effective oxidizing agent for the degradation of such a toxic dye [2].

Ferrites are ferrimagnetic materials encompassing complex oxides composed of oxides comprising ferric ions as the main constituent and classified as magnetic materials as they parade ferrimagnetic behavior. The magnetic chattels of ferrite rise from interactions amid metallic ions inhabiting particular positions comparative to the oxygen ions in the crystal structure of the oxide. Snoek and his associates advanced assortment of ferrites during 1945 to 1993 at the Philips Research Laboratories, Netherland.

Based on the molar ratio of Fe_2O_3 to other oxide components present in them and their crystal structure, ferrites can further be classified into four different groups as spinel ferrites, garnet ferrites, ortho ferrites and hexagonal ferrites [3-6]. All these ferrites are noteworthy for their exceptional chemical stability, remarkable mechanical hardness, high electromagnetic strength, … etc.

$NiFe_2O_4$ fascinated researchers with its vitalizing low conductivity ferromagnetic properties and therefore low eddy current loss, abundance in nature, catalytic behavior, high electrochemical stability, … etc.

Spinel ferrite nanoparticles can be synthesized using a range of techniques, including co-precipitation, micro emulsion sol-gel, citrate sol gel, hydrothermal, the redox process, combustion, … etc. [7-10]. These synthesis methods have their own advantages and disadvantages. Santi Maensiri et al. [11] have first reported egg white method for synthesis of spinel ferrite nanoparticles, which is a cost-effective, environmentally benevolent, eco-friendly and simple method for preparing transition metal-substituted ferrites at low temperatures. Also, the toxic precursors and harmful effluents out of the reaction can also be reduced as egg white is used as precursor.

Ferrites are superior nanoparticles finding applications in practically all fields of science and technology extending from millimeter wave integrated circuitry to power handling, data storage, protective coatings and basis for lithium ion batteries, catalyst and sensors, … etc. These magnetic nanoparticles find special applications in the field of biomedicine, like drug targeting, hyperthermia and magnetic resonance imaging, … etc. owing to their elemental composition which makes them biocompatible and degradable [12-17]. Ferrites are among the effective visible light sensitive photocatalysts, as they can be used directly to harness the freely available sunlight for pollutant degradation. Keeping this view, in our present study, we made an attempt to prepare $NiFe_2O_4$ nanoparticles *via* single-step synthesis technique. In order to use it for waste water retreatment which is a driving solution for water pollution prevention. Nickel ferrite nanoparticles were already reported to be a photocatalyst for methylene blue dye with 94% efficiency [18, 19]. But till now, there is no report for $NiFe_2O_4$ nanoparticles synthesized *via* green synthesis route using egg white as fuel as a photocatalyst.

2. Experimental Procedure

2.1 Preparation

Nickel ferrite magnetic nanoparticles were made using high-chemical purity ferric nitrate nonahydrate and nickel nitrate hexahydrate along with newly prepared egg white. Egg white, rich in albumen protein- is recognized for its foaming and emulsification characteristics and is easily soluble in water, which makes it easy to combine with metal ions, while egg white is also used as a binder cum gel for material shaping [11].

Egg white and double distilled water are combined in 3:1 ratio by vigorous stirring at room temperature for one hour to form a homogeneous solution. Ni $(NO_3)_2.6H_2O$ and Fe $(NO_3)_3.9H_2O$ are taken in such a way that the corresponding composition of nickel to ferrite is 1:2 mole ratio, added dropwise to the homogeneous solution of the egg white and

strongly stirred at room temperature for four hours. No pH changes are made during the process. The mixed solution was then heated for several hours on a hot plate at 80°C, until a dried precursor was obtained. Then, the powder as synthesized was calcined for 3 hours in a muffle furnace at 600°C [20].

2.2 Characterization

The nickel ferrite nanoparticles were characterized using X-ray diffractometer, Fourier transform infrared spectroscopic analysis using KBr pellets, High-resolution Scanning Electron Microscopy, Energy Dispersive X-ray spectroscopy analysis and Vibrating Sample Magnetometer were used. The crystallite phase of the nickel ferrite was confirmed by X - ray diffraction using XPERT PRO diffractometer. The Fourier Transform Infrared analysis was recorded using Bruker IFS66V FT-IR spectrometer. The morphology of the prepared sample was studied using High Resolution Scanning Electron Microscopy. The magnetic parameter was measured using Vibrating Sample Magnetometer.

3. Results and Discussion

3.1 X-ray Diffraction Analysis

The XRD pattern of nickel ferrite nanoparticles are shown in Fig. 1. The result got from XRD data is in good agreement with the standard values of nickel ferrite (JCPDS file No: 86 – 2267). The characteristic planes at (220), (311), (400), (511) and (440) in the figure specifies the existence of cubic spinel structure. The lattice parameter of the nickel ferrite nanoparticles are found to be a = 8.337 ± 1Å using UNITCELL software [21].

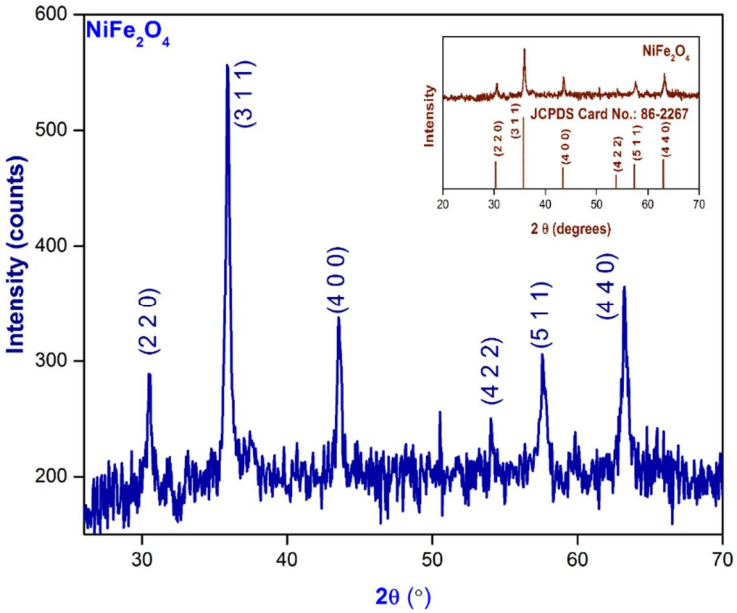

FIG. 1. XRD pattern of $NiFe_2O_4$.

Using Scherrer formula, the particle size of $NiFe_2O_4$ is calculated from the maximum intensity peak at (3 1 1) plane as 34 ± 3 nm.

$$D = \frac{k\lambda}{\beta cos\theta}$$

where 'D' is the particle size, 'λ' is the wavelength of X-ray beam used, 'β' and 'θ' represent full width half maximum and Bragg's diffraction angle of the corresponding peak, respectively and 'k' is the instrumental constant.

The X-ray density (P_x) is calculated using the following formula as 5.3020g/cc.

$$P_x = \frac{8M}{Na^3}$$

M, N and a represent molecular weight, Avagadro number and lattice constant of $NiFe_2O_4$ nanoparticles [22, 23].

Hopping lengths d_A and d_B of tetrahedral and octahedral sites are the distance between magnetic ions. d_A and d_B are calculated as d_A = 3.6291Å and d_B = 2.9632Å, respectively, using the following formulae [24]:

$$d_A = 0.25a\sqrt{3}$$

$$d_B = 0.25a\sqrt{2}$$

3.2 Fourier Transform Infrared Analysis (FT-IR) Measurement

FTIR approves the development of the spinel structure in $NiFe_2O_4$. FTIR spectrum of nickel ferrite nanoparticles are recorded in the wave number range of 4000 to 400 cm^{-1} and portrayed in Fig. 2. Two main broad metal – oxygen bands are seen in the spectrum, with the higher one (ν_1) in 589 cm^{-1} is caused by the stretching vibrations of the tetrahedral metal – oxygen [Fe–O] band, which the lower one (ν_2) in the range 419 cm^{-1} is caused by the metal – oxygen [Ni – O] vibrations in the octahedral sites [25]. The intensive wide band at 3410 cm^{-1} and less intensive one at 1574 cm^{-1} in the spectrum are owed to O–H stretching vibration intermingling through H bonds. The stretching vibration of the carboxylate group (CO_2^{2-}) is witnessed from the band at 1414 cm^{-1} and the band at 1109 cm^{-1} links to nitrate ion traces [26,27]. The values of the force constants K_T and K_O for corresponding frequencies ν_1 and ν_2 of the A-and B-sites of $NiFe_2O_4$ are calculated as 2.5379 Nm^{-1} and 1.2843 Nm^{-1}, respectively, using the formulae given below [28].

$$K_T = 4\pi c^2 \nu_1^2 \mu$$

$$K_O = 4\pi c^2 \nu_2^2 \mu$$

where, c is the velocity of light, ν_1 and ν_2 are the frequency of vibration of the A-and B-sites and μ is the reduced mass for the Fe^{3+} ions and the O^{2-} ions, which is approximately equivalent to 2.065×10^{-23}g.

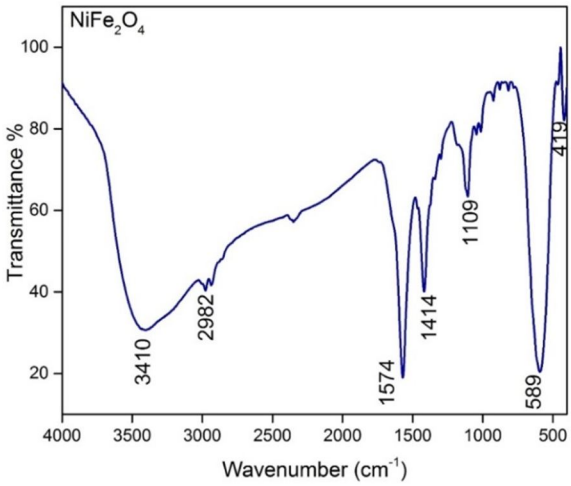

FIG. 2. FTIR spectra of $NiFe_2O_4$.

3.3 Vibrating Sample Magnetometer Analysis

From the data obtained from the Vibrating Sample Magnetometer, the magnetic property of nickel ferrite nanoparticles are analyzed. Fig. 3 illustrates the hysteresis loop for the nickel ferrite nanoparticles at room temperature. The hysteresis loop of the nickel ferrite nanoparticles is found to have less loop area which confirms the $NiFe_2O_4$ to belong to soft magnetic nanoparticles which find significance in magnetic memory devices. The magnetic moment, retentivity and coercivity of the nickel ferrite nanoparticles are 0.04319, 0.13001 emu and 137.79 G, respectively [20, 24].

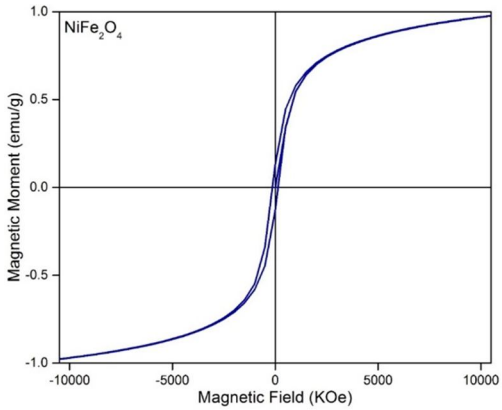

FIG. 3. Hysteresis loop of $NiFe_2O_4$.

3.4 EDX and HR-SEM Analysis

The elements present in the nickel ferrite nanoparticles are surveyed using EDX spectra. The EDX spectra of $NiFe_2O_4$ are depicted in Fig 4. The peaks at around 0.77 eV, 6.39 eV and 7 eV in the spectra support the existence of iron in the nickel ferrite nanoparticles. The peak at around 0.5 eV in the spectra discloses the existence of oxygen. The peaks at 0.85 eV, 7.47 eV and 8.2 eV in Fig. 4 narrate the existence of nickel [29].

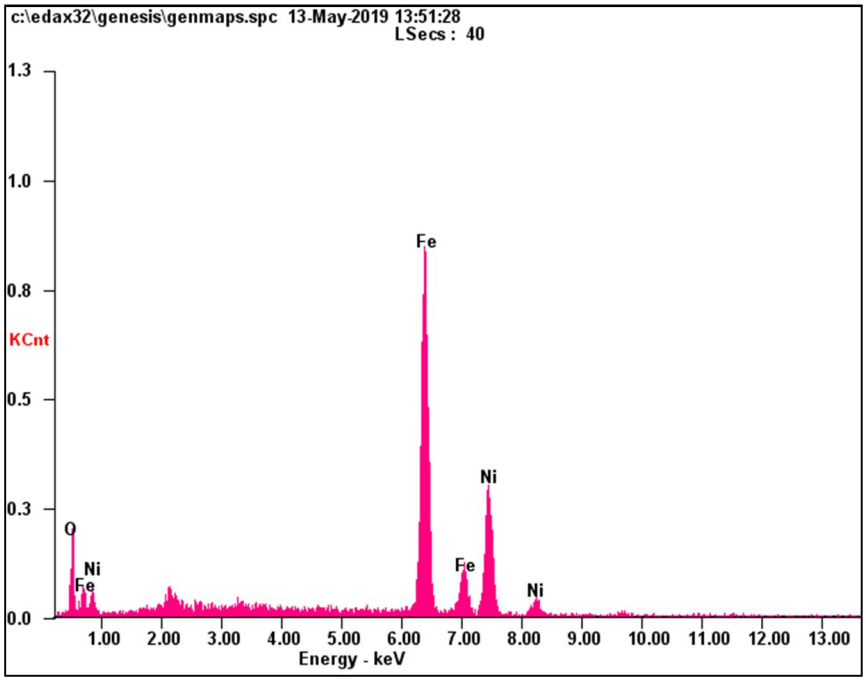

FIG. 4. EDX spectra of $NiFe_2O_4$.

The morphology of the synthesized nickel ferrite nanoparticles is recorded using HR-SEM. The HR-SEM image of $NiFe_2O_4$ at the magnification of 500 nm is represented in Fig. 5. The average particle size value was measured using ImageJ software considering as many particles as possible from the micrograph in Fig. 5 and was found to be in the range 10 to 45nm. The accumulation arises in ferrite nanoparticles owing to its magnetic nature and the binding of primary particles held together by fragile surface interactions, such as Vander Waals force. A histogram was plotted for the particle size by applying Gaussian curve to figure out the most probable value of particle size. From Gaussian fit in Fig. 5, the mean, median, maximum and minimum diameters of the $NiFe_2O_4$ nanoparticles have been determined and the values of maximum and minimum diameters are found to be 41.759 and 12.136 nm, respectively. The standard deviation of nickel ferrite nanoparticles was found to be 6.677 nm [30]. The particle size agrees well with the particle size calculated from XRD data.

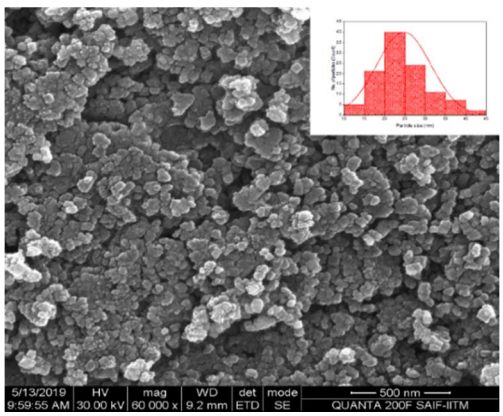

FIG. 5. Surface morphology and particle size distribution of $NiFe_2O_4$.

4. Photocatalytic Activity of Nickel Ferrite

The photocatalytic activities of nickel ferrite nanoparticles under ultraviolet light irradiation were evaluated by monitoring the decolorization of methylene blue dye. Methylene blue dye photocatalytic degradation was performed in a three-pyrex flask reactor, using $NiFe_2O_4$ nanoparticles as a photocatalyst under xenon arc lamp UV illumination (300W, Hamamatus: L 2479). 10ppm dye solution was prepared in 100ml DI water for the photocatalytic degradation of methylene blue dye, in which 0.15 g photocatalyst ($NiFe_2O_4$ nanoparticles) was added and the resulting mixture was expunged with Ar gas under continuous stirring. Consequently, the suspension obtained was balanced for 30 min to stabilize the absorption of methylene blue dye over $NiFe_2O_4$ nanoparticles before light exposure [31].

To track the process of photocatalytic degradation, the characteristic absorption of methylene blue dye at 655 nm was chosen. Fig. 6 shows a typical methylene blue dye (initial concentration: 10 mg l-1, 50 ml) photocatalytic degradation cycle using 0.05 g of the $NiFe_2O_4$ sample under UV light irradiation. With the increase in exposure time, the absorption peaks corresponding to methylene blue dye have slowly decreased.

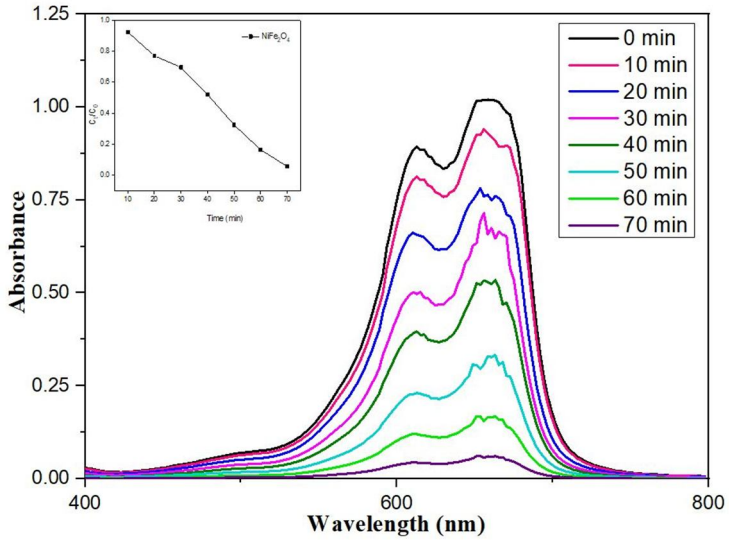

FIG.6. Absorption spectra of methylene blue dye solution in presence of $NiFe_2O_4$ photocatalyst and its degradation graph.

The photocatalytic performance of the sample with the exposure time was determined from the expression below:

$$\eta = \frac{A_o - A}{A_o} \times 100\%$$

where η is the removal efficiency, A_o is the initial absorbance and A is the variable absorbance [32].

The findings showed that the solution's absorbance decreases with increasing time intervals, suggesting that the dyes concentration decreases as exposure time increases. The degradation efficiency of $NiFe_2O_4$ photocatalyst against methylene blue is 95.6%. Thus, the nickel ferrite nanoparticles synthesized *via* the combustion process using egg white as fuel acts as an effective photocatalyst for methylene blue degradation.

5. Conclusion

The present research focused on the synthesis of nickel ferrite nanoparticles using egg white as the eco-friendly precursor *via* green synthesis path. In the auto combustion process, the egg white protein albumen was acting as fuel. The XRD results confirmed the formation of $NiFe_2O_4$ nanoparticles of nickel ferrite with a cubic spinel structure and particle size of 34 $\pm$ 3 nm. The absorption peaks in the FTIR spectra due to the vibrations of metal oxygen in 419 and 589 cm^{-1} confirms the spinel structure of nickel ferrite. The micrographs of the HRSEM showed highly agglomeration uniform spheres and the particle size to be varying from 12 to 43 nm, which is in good agreement with XRD results. The EDAX spectra clearly confirmed the existence of Ni, Fe and O in nanoparticles containing $NiFe_2O_4$. VSM was used to calculate the magnetic

parameters, such as coercivity, retentiveness and magnetic moment. The synthesized nickel ferrite nanoparticles were found to be a good photocatalyst for methylene blue dye in the ultraviolet region with efficiency of 95.6% which is more when compared to the nickel ferrite nanoparticles synthesized via chemical routes.

References

[1] Sundararajanl, M., John Kennedy, L., Nithya, P., Judith Vijaya, J. and Bououdina, M., Journal of Physical and Chemistry of Solids, 108 (2017) 61.

[2] Singhal, S., Sharma, R., Singh, C. and Bansal, S., Indian Journal of Materials Science, 2013 (2013) 1.

[3] Vinnik, D.A., Podgornov, F.V., Zabeivorota, N.S., Trofimov, E.A., Zhivulin, V.E., Chernukha, A.S., Gavrilyak, M.V., Gudkova, S.A., Zherebtsov, D.A., Ryabov, A.V., Trukhanov, S.V., Zubar, T.I., Panina, L.V., Podgornaya, S.V., Zdorovets, M.V. and Trukhanov, A.V. , Journal of Magnetism and Materials, 498 (2020) 166190.

[4] Kozlovskiy, A., Kenzhina, I. and Zdorovets, M., Ceramics International, 45 (2019) 8669.

[5] Almessiere, M.A., Trukhanov, A.V., Khan, F.A., Slimani, Y., Tashkandi, N., Turchenko, V.A., Zubar, T.I., Tishkevich, D.I., Trukhanov, S.V., Panina, L.V. and Baykal, A., Ceramics International, 46 (2020) 7346.

[6] Almessiere, M.A., Slimani, Y., Güngüneş, H., Kostishyn, V.G., Trukhanov, S.V., Trukhanov, A.V. and Baykal, A., Ceramics International, 46 (2020) 11124.

[7] Shumskaya, E.E., Kaniukov, E.Y., Vinnik, D.A., Zdorovets, M.V., Anisovich, M., Trukhanov, A.V., Tosi, D. and Molardi, C., Nanomaterials, 9 (2019) 1.

[8] Tishkevich, D.I., Korolkov, I.V., Kozlovskiy, A.L., Anisovich, M., Vinnik, D.A., Ermekova, A.E., Vorobjova, A.I., Shumskaya, E.E., Zubar, T.I., Trukhanov, S.V., Zdorovets, M.V. and Trukhanov, A.V., Journal of Alloys and Compounds, 797 (2019) 573.

[9] Almessiere, M.A., Trukhanov, A.V., Slimani, Y., You, K.Y., Trukhanov, S.V., Trukhanova, E.L., Esa, F., Sadaqat, A., Chaudhary, K., Zdorovets, M. and Baykal, A., Nanomaterials, 9 (2019) 202.

[10] Zdorovets, M.V. and Kozlovskiy, A.L., Surface and Coatings Technology, 383 (2020) 125286.

[11] Maensiri, S., Masingboon, C., Boonchom, B., Seraphin, S., Scripta Materialia, 56 (2007) 797.

[12] Trukhanov, S.V., Journal of Experimental and Theoretical Physics, 100 (2005) 95.

[13] Zdorovets, M.V. and Kozlovskiy, A.L., Vacuum, 168 (2019) 108838.

[14] Trukhanov, S.V., Troyanchuk, I.O., Pushkarev, N.V. and Szymczak, H., Journal of Experimental and Theoretical Physics, 95 (2002) 308.

[15] Trukhanov, S.V., Trukhanov, A.V., Vasil'ev, A.N., Maignan, A. and Szymczak, H., Journal of Experimental and Theoretical Physics Letters, 85 (2007) 507.

[16] Trukhanov, S.V., Khomchenko, V.A., Lobanovski, L.S., Bushinsky, M.V., Karpinsky, D.V., Fedotova, V.V., Troyanchuk, I.O., Trukhanov, A.V., Stepin, S.G., Szymczak, R., Botez, C.E. and Adair, A., Journal of Experimental and Theoretical Physics, 103 (2006) 398.

[17] Zdorovets, M.V., Arbuz, A. and Kozlovskiy, A.L., Ceramics International, 46 (2020) 6217.

[18] Mathubala, G., Manikandan, A., Arul Antony, S. and Ramar, P., Journal of Molecular Structure, 1113 (2016) 79.

[19] Adeleke, J.T., Theivasanthi, T., Thiruppathi, M., Swaminathan, M., Akomolafe, T. and Alabi, A.B., Applied Surface Science, 455 (2018) 195.

[20] Aji Udhaya, P. and Meena, M., Materials Today: Proceedings, 9 (2019) 528.

[21] https://www.esc.cam.ac.uk/research/research-groups/research-projects/tim-hollands-software-pages/unitcell.

[22] Annie Vinosha, P., Ansel Mely, L., Emima Jeronsia, J., Krishnan, S. and Jerome Das, S., Optik, 134 (2017) 99.

[23] Aji Udhaya, P., Bessy, T.C. and Meena, M., Materials Today: Proceedings, 8 (2019) 169.

[24] Nikam, D.S., Jadhav, S.V., Khot, V.M., Bohara, R.A., Hong, C.K., Mali, S.S. and Pawar, S.H., RSC Advances, 5 (2015) 2338.

[25] Raju, M.K., Chemical Science Transactions, 4 (2015) 137.

[26] Waldron, R.D., Physical Review, 99 (1955) 1926.

[27] Aji Udhaya, P., Meena, M. and Queen, M.A.J., International Journal of Scientific Research in Physics and Applied Sciences, 7 (2019) 71.

[28] Vijaya Babu, K., Satyanarayana, G., Sailaja, B., Santosh Kumar, G.V., Jalaiah, K. and Ravi, M., Results in Physics, 9 (2018) 55.

[29] https://www.edax.com/resources/interactive-periodic-table.

[30] Kumar, D., Kumar, A., Prakash, R., Singh, A.K., AIP Conference Proceedings, 2142 (2019) 070018.

[31] Vinosha, P.A., Xavier, B., Anceila, D. and Jerome Das, S., Optik, 157 (2018) 441.

[32] Pudukudy, M. and Yaakob, Z., Journal of Cluster Science, 25 (2014) 1.

Volume 15, Number 1, 2022. pp. 445-449

Jordan Journal of Physics

ARTICLE

Albumen-mediated Green Synthesis of $ZnFe_2O_4$ Nanoparticles and Their Physico-Chemical Properties

P. Aji Udhaya[a,b], **M. Meena**[c], **M. Abila Jeba Queen**[a], **M. Mary Freeda**[a] and **T. Regin Das**[d]

[a] *Department of Physics, Holy Cross College, Nagercoil, Affiliated to Manonmaniam Sundaranar University, Abishekapatti, Tirunelvel-627012, India.*

[b] *Research Scholar, Reg. No. 18123152132038, Department of Physics, S.T. Hindu College, Nagercoil, Affiliated to Manonmaniam Sundaranar University, Abishekapatti, Tirunelvel-627012, India.*

[c] *Department of Physics, S.T. Hindu College, Nagercoil, Affiliated to Manonmaniam Sundaranar University, Abishekapatti, Tirunelvel-627012, India.*

[d] *Department of Physics, Lekshmipuram Arts and Science College, Neyyoor, Nagercoil, India.*

Doi: **https://doi.org/10.47011/14.5.6**

Received on: 01/05/2020; *Accepted on: 15/9/2020*

Abstract: Spinel ferrites with general formula AB_2O_4 possess charming magnetic and electrical properties owing to their thermal and chemical steadfastness. Spinel zinc ferrite ($ZnFe_2O_4$) nanoparticles have attracted massive attention due to their unusual amalgamation of properties, especially magnetic properties, where these properties are equipped as suitable candidates in the field of electronics. Here, a simple self-combustion technique is made with the assistance of albumen to synthesize nanocrystalline zinc ferrite ($ZnFe_2O_4$) particles. The egg white (albumen) that is used in the synthesis process plays the fuel role in the process of combustion. The results of the powder X-ray diffraction (PXRD) and Fourier Transform Infrared Spectroscopy (FTIR) suggested that the synthesized nanoparticles are of single phase and show spinel structure. The photoluminescence studies reported a doublet peak at around 360-380 nm. The functional groups present in the synthesized nanoparticles were revealed from FTIR data. EDX findings give an account of the percentage composition of the elements Fe, Zn and O present in the synthesized sample. High-resolution Scanning Microscope (HRSEM) reveals the agglomerated coalescence nature of ferrite nanoparticles.

Keywords: Ferrite, PXRD, FTIR, HRSEM, EDX Albumen.

1. Introduction

Ferrites are of interest due to their electrical, magnetic and mechanical properties, which can be adapted to the requirements of device manufacturing and biological applications. Magnetic Nanoparticles have emerging biomedical applications in sundry areas, such as disease diagnostics, magnetic resonance imaging, sensors, actuators, magnetic storage devices, … etc. Nano-sized ferrites of the MFe_2O_4 type are the most significant magnetic materials which have yet to be properly investigated on the way to their physical and chemical properties. The metal-iron ratio plays a crucial role in the regulation of MFe_2O_4 nanoparticles' magnetic properties [1, 2]. Due to the increased volume fraction of surface atoms, surface effects may be crucial when reducing

Corresponding Author: P. Aji Udhaya **Email**: ajiudhaya@gmail.com

particle dimensions. As a competent appendage of the ferrite family, $ZnFe_2O_4$ has grasped researchers because of its invigorating magnetic properties as opposed to other ferrites. After a thorough study of the solid-state reaction, this approach was adopted. It is possible to synthesize nanoparticles using physical, chemical, mechanical and thermal processes, using techniques, such as coprecipitation, sol-gel, combustion, ball milling, … etc. But, non-toxic eco-friendly precursors, such as plant extracts and animal by-products, are used for the synthesis of nanoparticles to reduce or eliminate the use or production of toxic substances, which is known as green synthesis. The albumen-enriched egg white was first recorded by Santi Maensiri et al. [3] for the preparation of ferrites substituted for transition metal. The magnetic, electrical, optical, morphological and other properties of nanoparticles can be studied using various tools, such as X-ray diffraction, Scanning Electron Microscope, Vibrating Sample Magnetometer, Fourier Transfer Infrared Spectroscopy, … etc.

The ultimate objective of this work is to examine the physical, chemical and morphological properties of zinc ferrite.

2. Experimental Procedure

2.1 Preparation

Zinc ferrite magnetic nanoparticles were synthesized using ferric nitrate nonahydrate and zinc nitrate hexahydrate of high chemical purity along with freshly prepared egg white. Egg white, rich in albumen protein, is recognized for its frothing and emulsifying features and it is easily soluble in water, which makes it combine with metal ions easily. Egg white also assists as binder cum gel for shaping materials. Egg white and double distilled water are mixed in 3:1 ratio to form a homogeneous solution by vigorous stirring at room temperature for one hour. Zn $(NO_3)_2.6H_2O$ and Fe $(NO_3)_3.9H_2O$ are taken such that corresponding zinc to ferrite composition is 1:2 mole ratio, gradually added to the homogenous egg white solution and vigorously stirred at room temperature for four hours. pH adjustments are not made during the process. Then, the mixed solution was heated on a hot plate at 80°C for several hours until a dried precursor was obtained. Then, the synthesized powder was calcined in a muffle furnace at 600°C for 3 hours [4].

2.2 Characterization

The calcined zinc ferrite nanoparticles were characterized using X-ray diffractometer, Fourier Transform Infrared spectroscopic analysis using KBr pellets, High-resolution Scanning Electron Microscopy and Energy Dispersive X-ray spectroscopy analysis. The crystallite phase of the zinc ferrite was confirmed by X - ray diffraction using XPERT PRO diffractometer. The infrared analysis of the Fourier Transform was reported using the IFS66V FT-IR spectrometer from Bruker. The morphology of the prepared samples was studied using High-resolution Scanning Electron Microscopy.

3. Results and Discussion

3.1 X-ray Diffraction Analysis

The PXRD profile of $ZnFe_2O_4$ nanoparticles is illustrated in Fig. 1. The typical reflection at (2 2 0), (3 1 1), (4 0 0), (4 2 2), (5 1 1) and (4 4 0) in the figure corresponds to face-centered cubic spinel structure of $ZnFe_2O_4$ matching incredibly well with the JCPDS card No.22-1012. The lattice parameter of the prepared zinc ferrite nanoparticles is found to be a = 8.4056 ± 0.01Å from UNITCELL software. The particle size of $ZnFe_2O_4$ is calculated using De-bye Scherrer formula and it was found to be ranging from 30 to 62 nm. X-ray density and hopping length of $ZnFe_2O_4$ nanoparticles were obtained as ρ_x = 5.3706g/cc, d_A = 3.639 Å and d_B = 2.9718 Å, respectively.

The X-ray density (ρ_x) is calculated using the following formula (Eq. 1):

$$\rho_x = \frac{8M}{Na^3} \quad (1)$$

where M, N and a represent molecular weight, Avagadro number and lattice constant of the nanoparticles [4, 5].

And Eqs. 2 and 3 are used to calculate the values of the hopping lengths of the tetrahedral (A) and octahedral (B) sites [6].

$$d_A = 0.25a\sqrt{3} \quad (2)$$

$$d_B = 0.25a\sqrt{2} \quad (3)$$

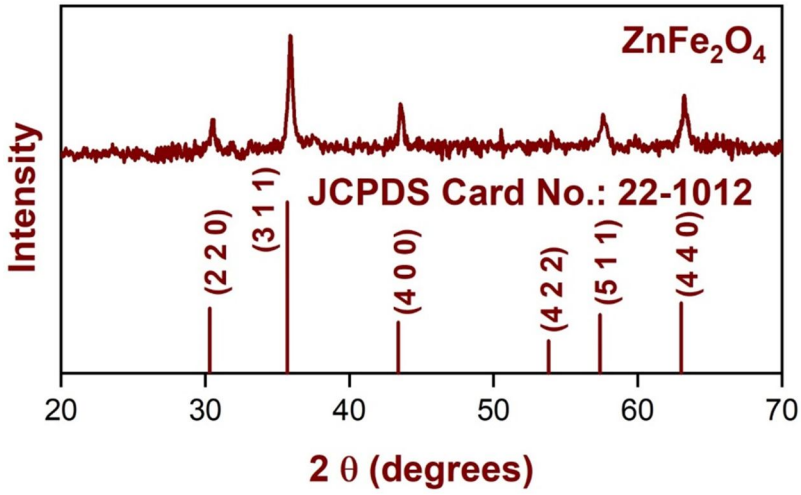

FIG. 1. XRD pattern of $ZnFe_2O_4$.

3.2 Fourier Transform Infrared Analysis (FT-IR) Measurement

FTIR confirms the formation of spinel structure in $ZnFe_2O_4$. FTIR spectra of the prepared zinc ferrite samples were recorded in the wave number range of 4000 to 400cm^{-1} and portrayed in Fig. 2. Two main broad metal – oxygen bands are seen in the samples, with the higher one (ν_1) in 546 cm^{-1} is caused by the stretching vibrations of the tetrahedral metal – oxygen [Fe–O] band, while the lower one (ν_2) in the range 432 cm^{-1} is caused by the metal – oxygen [Zn – O] vibrations in the octahedral sites. The values of force constant are calculated for $ZnFe_2O_4$ as 2.1808 Nm^{-1} and 1.365 Nm^{-1}, respectively.

The values of the force constants K_T and K_O for corresponding frequencies ν_1 and ν_2 of the A- and B-sites of $ZnFe_2O_4$ are calculated using the formulae given below [7].

$$K_T = 4\pi c^2 \nu_1^2 \mu \quad (4)$$

$$K_O = 4\pi c^2 \nu_2^2 \mu \quad (5)$$

where, c is the velocity of light, ν_1 and ν_2 are the frequency of vibration of the A- and B-sites and μ is the reduced mass for the Fe^{3+} ions and the O^{2-} ions, which is approximately equivalent to 2.065x10^{-23}g.

The bands observed around 3410 and 1632 cm^{-1} are attributed to the tensional stretching modes of water molecules absorbed by the nanoparticle. The stretching vibration of the carboxylate group (CO_2^{2-}) is witnessed at 2927 cm^{-1} and 2346 cm^{-1}. The band at 1104 cm^{-1} links to nitrate ion traces [3, 4, 8-10].

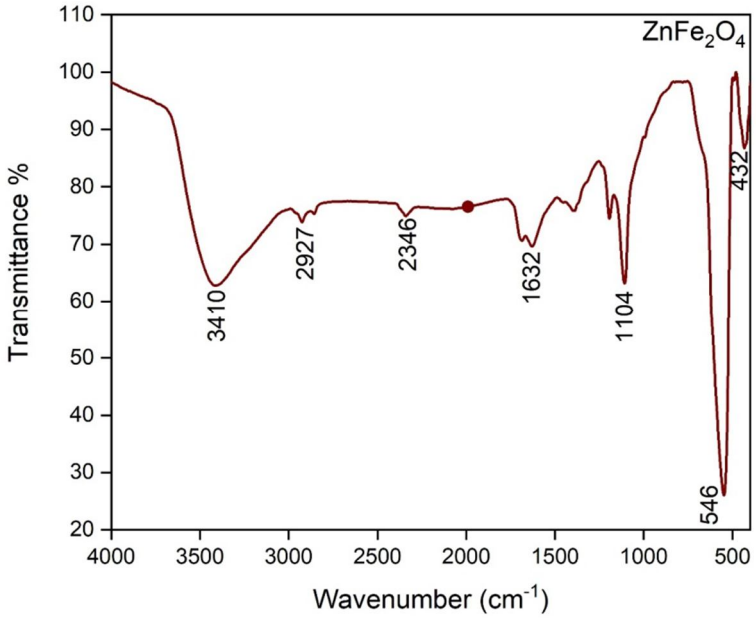

FIG. 2. FTIR pattern of $ZnFe_2O_4$.

3.3 EDX and HR-SEM Analysis

The elements present in the zinc ferrite nanoparticles are surveyed using EDX spectra. The EDX spectra of $ZnFe_2O_4$ are depicted in Fig 3. The peaks at around 0.7 eV, 6.4 eV and 7 eV in the spectra approve the existence of iron in the Zinc Ferrite nanoparticles. The peak at around 0.5 eV in the spectra reveals the existence of oxygen. The peaks at 1.1 eV, 8.7 eV and 9.6 eV in Fig. 3 relate to the existence of zinc [11].

The morphology of the synthesized zinc Ferrite nanoparticles is recorded using HR-SEM. The HR-SEM image of $ZnFe_2O_4$ at the magnification of 500 nm is portrayed in Fig. 4. From the figure, it is evident that the particle size of $ZnFe_2O_4$ varies from 15 to 55 nm. There is a considerable degree of accumulation of unifora m spherically formed zinc ferrite nanoparticles. The agglomeration arises in ferrite nanoparticles owing to their magnetic nature and the binding of primary particles held together by fragile surface interactions, such as Vander Waals force [12]. From Gaussian fit in Fig. 4, the maximum and minimum diameters of the $ZnFe_2O_4$ nanoparticles have been determined and the values are found to be 51.43 and 16.97 nm, respectively. The standard deviation of zinc ferrite nanoparticles was found to be 7.138 nm [13]. The particle size agrees well with the particle size calculated from XRD data.

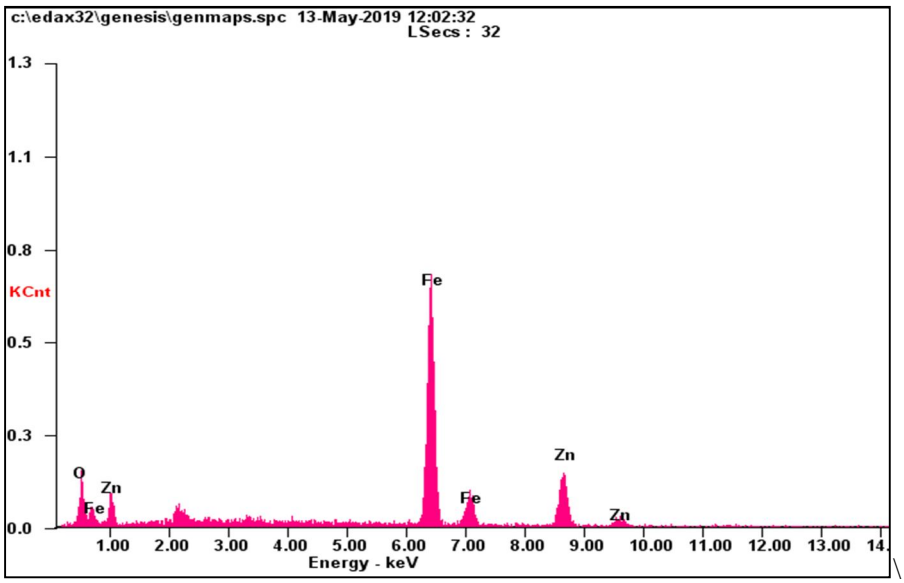

FIG. 3. EDX spectra of $ZnFe_2O_4$.

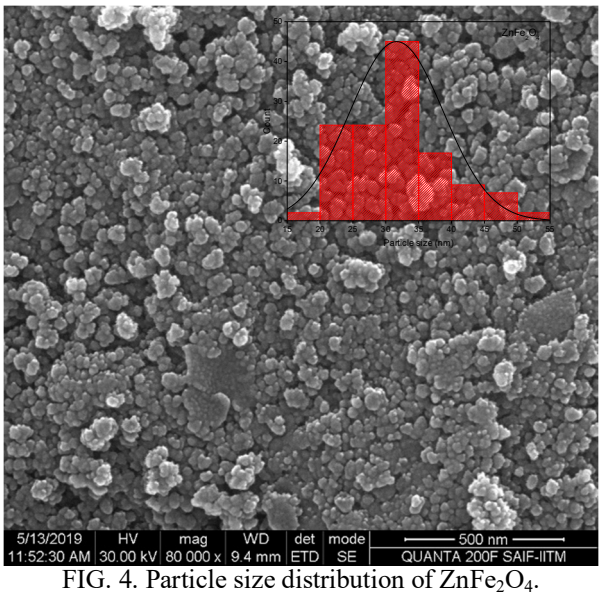

FIG. 4. Particle size distribution of $ZnFe_2O_4$.

4. Conclusion

$ZnFe_2O_4$ nanoparticles have been successfully prepared via simple self-combustion method using albumen (a protein in egg white) as fuel. The gel formed by water soluble egg white has served as a matrix for the entrapment of metal ions. From the XRD analysis, it is found that $ZnFe_2O_4$ exhibits a cubic spinel structure with particle size varying from 30 to 62 nm. FTIR spectra confirmed the spinel structure from the two main broad metal-oxygen bands in the spectra. From HR-SEM analysis, the prepared zinc ferrite nanoparticles were found to be accumulated uniform spherical particles. EDX spectra show the presence of Zn, Fe and O in the $ZnFe_2O_4$ nanoparticles.

References

[1] Vinosha, P.A., Mely, L.A., Jeronsia, J.E., Monica, F.H., Raja, K. and Das, S.J., Nano Hybrids and Composites, 17 (2017) 1.

[2] Sundararajan, M., Sailaja, V., Kennedy, L.J. and Vijaya, J.J., Ceramics International, 43 (2017) 540.

[3] Maensiri, S., Masingboon, C., Boonchom, B. and Seraphin, S., Scripta Materialia, 56 (2007) 797.

[4] Udhaya, P.A., Bessy, T.C. and Meena, M., Materials Today: Proceedings, 8 (2019) 169.

[5] Vinosha, P.A., Mely, L.A., Jeronsia, J.E., Krishnan, S. and Das, S.J., Optik, 134 (2017) 99.

[6] Nikam, D.S., Jadhav, S.V., Khot, V.M., Bohara, R.A., Hong, C.K., Mali, S.S. and Pawar, S.H., RSC Advances, 5 (2015) 2338.

[7] Vijaya Babu, K., Satyanarayana, G., Sailaja, B., Santosh Kumar, G.V., Jalaiah, K. and Ravi, M., Results in Physics, 9 (2018) 55.

[8] Udhaya, P.A., Meena, M. and Queen, M.A.J., International Journal of Scientific Research in Physics and Applied Sciences, 7 (2019) 71.

[9] Sundararajan, M., Kennedy, L.J., Aruldoss, U., Pasha, S.K, Vijaya, J.J. and Dunn, S., Materials Science in Semiconductor Processing, 20 (2015) 1.

[10] Udhaya, P.A. and Meena, M., Materials Today: Proceedings, 9 (2019) 528.

[11] Li, L., Bi, H., Gai, S., He1, F., Gao, P., Dai, Y., Zhang, X., Yang, D., Zhang, M. and Yang, P., Scientific Reports, 7 (2017) 43116.

[12] Babić-Stojić, B., Jokanović, V., Milivojević, D., Jagličić, Z., Makovec, D., Jović, N. and Marinović-Cincović, M., Journal of Nanomaterials, 2013 (2013) 741036.

[13] Jeseentharani, V., George, M., Jeyaraj, B., Dayalan, A. and Nagaraja, K.S., Journal of Experimental Nanoscience, 8 (3) (2013) 358.

Volume 15, Number 1, 2022. pp. 451-456

Jordan Journal of Physics

ARTICLE

Synthesis and Characterization of Zn-doped $CuWO_4$Nanoparticles and Their Opto-structural Properties

V.Balasubramanian[a], **S. Kannan**[b], **T. Daniel**[a], **J. Henry**[a], **K. Mohanraj**[a] and **G. Sivakumar**[c]

[a] *Department of Physics, Manonmaniam Sundaranar University, Tirunelveli – 627 012, Tamil Nadu, India.*

[b] *Department of Physics, Excel Engineering College, Namakkal-637 303, Tamil Nadu, India.*

[b] *CISL, Department of Physics, Annamalai University, Annamalai Nagar – 608 002, Tamil Nadu, India.*

Doi: **https://doi.org/10.47011/14.5.7**

Received on: 01/05/2020; *Accepted on: 15/9/2020*

Abstract: $CuWO_4$ and Zn-doped $CuWO_4$ nanoparticles were prepared by a solid-state reaction method. The XRD study confirms the triclinic crystal structure for both samples and the peak shift is noticed for Zn-doped $CuWO_4$ particles with high crystallinity. The FTIR spectra show metal oxide vibration which arose from the $CuWO_4$ and Zn-doped $CuWO_4$ particles. The optical absorption spectra exhibit strong absorption in the visible region and the band gap of Zn-doped $CuWO_4$ is found to be increased to 2.44 eV compared to that of $CuWO_4$ (2.36 eV), which is due to the elevated conduction band levels after Zn-doping. The SEM images of both $CuWO_4$ and Zn-doped $CuWO_4$ nanoparticles show densely aggregated particles.

Keywords: Copper tungstate, Zn-doped $CuWO_4$, Absorption, Nanoparticles.

1. Introduction

Copper (Cu) - containing oxides have wide potential applications in the fields of catalysis and electrochemistry. Among them, Cu-ternary oxides showed more stability against photocorrosion than Cu-binary oxides [1]. Introducing CuO into WO_3 for the formation of $CuWO_4$ results in reduced bandgap between 2.1-2.3 eV with increased stability [2]. $CuWO_4$ can easily oxidize water due to maximum absorption of visible light from the solar spectrum [3]. It is observed that $CuWO_4$ has the ability to degrade methanol, methylene blue, methyl orange and phenol under visible light. However, the reported efficiencies are lower due to high charge recombination. Wen Yan et al. (2019) reported that $ZnWO_4$nanocystals exhibited improved photocatalytic activity for the degradation of methylene blue dye and are highly active in UV range due to their large bandgap[4]. It is learnt from the literature that noble metal oxides, such as $CoWO_4$, Ag_2WO_4 and Bi_2WO_6, have potentially tuned their structural and optical properties by doping [5-7]. In the present work, Zn was chosen as doping element owing to (i) similar oxidation state and ionic radius of Cu, (ii) it absorbs the entire visible region in the solar spectrum, (iii) it is cost-effective and available in abundance when compared with other elements, such as Ni, Nb, Zr, Mo, Ru and Rh. Doping of molybdenum, fluorine cations with $CuWO_4$ have been already investigated and the incorporation of zinc has not been explored well [8, 9]. Thus, the results suggest that doping of Zn into $CuWO_4$ particles can increase the efficiency of the photocatalyst due to large electron density. Besides, zinc is an

Corresponding Author: K. Mohanraj **Email**: kmohanraj.msu@gmail.com

effective strategy to retard the surface modification due to similar ionic radius[10]. Herein, we synthesizes $CuWO_4$ and Zn-doped $CuWO_4$ nanoparticles *via* solid-state reaction method. The enhancement in structural, optical and morphological properties is analyzed with zinc-doped $CuWO_4$ nanoparticles.

2. Experimental Details

Facile solid-state reaction method was adopted for the preparation of $CuWO_4$ nanoparticles. First, 0.1 M of CuO and WO_3 were taken and well ground for one hour with the help of mortar and pestle. The well-ground particleswere transferred to alumina crucible which was kept in a muffle furnace at 600°C for three hours. Then, the $CuWO_4$ particles were allowed to cool within the furnace itself. To synthesize Zn-doped $CuWO_4$ nanoparticles, 0.5 M of CuO, 0.5 M of ZnO and 1 M of WO_3 were taken and the aforesaid process was adopted as that of $CuWO_4$ particles.The structural, optical and morphological studies were carried out using PANalytical XPERT-PRO) diffractometer system with Cu Kα radiation (λ=1.5406 Å) for recording X-ray diffraction patterns, Perkin Elmer spectrometer (Spectrum Two, Model: C92107) with resolution of $4cm^{-1}$ was used for recording the FTIR spectra, JEOL - JSM 5610LV Scanning electron microscope was used to analyze the surface morphology and Shimadzu UV-2700 for recording the UV-DRS analysis, respectively.

3. Results and Discussion

The reaction mechanism involved in the formation of $CuWO_4$ and Zn-doped $CuWO_4$ is given below:

$$CuO + WO_3 \longrightarrow CuWO_4 \quad (1)$$

$$0.5\ CuO + 0.5\ ZnO + WO_3 \longrightarrow Cu_{0.5}Zn_{0.5}WO_4 \quad (2)$$

The XRD pattern of $CuWO_4$ and Zn-doped $CuWO_4$is shown in Fig.1. The $CuWO_4$ nanoparticles show the prominent peak at 2θ = 28.77° belonging to (-1-11) plane and some high intense peaks are seen at 2θ = 30.24°, 2θ = 31.76°, 2θ = 32.24°, 2θ = 35.74° and 2θ = 38.67° belonging to (111), (-111), (1-11), (0-21) and (-120) plane, respectively, of triclinic crystal system (JCPDS card: 72-0616). All the sharp and intense diffraction peaks suggested the highly crystalline nature of $CuWO_4$. While introducing Zn, the major diffraction peak shifted with high intensity at 2θ=30.48° belonging to 1-11 plane. The shift in peaks from 2θ = 28.77° to 2θ = 30.48° indicates the incorporation of Zn into $CuWO_4$. Besides, the other intense peaks are seen at 2θ = 30.89°, 2θ = 36.34°, 2θ = 23.14° and 2θ = 23.64° belonging to 020, 0-21, -110 and 011 plane, respectively. Some additional peaks are also observed in the pattern at 2θ = 24.43°, 2θ = 33.30° and 2θ = 34.23°, which may be due to excess ZnO or WO_3 which are not involved in the reaction to completely transform into $Cu_{0.5}Zn_{0.5}WO_4$. All the peaks obtained are well-matched with the standard JCPDS card: 88-0260 has the triclinic system. The crystalline size was calculated using scherrer formula and it is found to be 34 nm and 40 nm for $CuWO_4$ and Zn-doped $CuWO_4$ nanoparticles, respectively.

Fig.2 shows the FTIR spectra of $CuWO_4$ and Zn-doped $CuWO_4$ nanoparticles. In the spectrum for $CuWO_4$, a band appears around 904 cm^{-1} attributed to stretching vibration of W=O in WO_3 octahedron associates with $CuWO_4$ [11]. Besides, a vibrational band is seen around 530 cm^{-1} corresponding to bending vibration of Cu-O of $CuWO_4$ due to $3d^{10}$ configuration of Cu_2O [12]. A broad band is also seen between 800 cm^{-1} and 650 cm^{-1}. In the case of Zn-doped $CuWO_4$, the broad band which appeared at 904 cm^{-1} becomes widened. It is important to note that the vibrational band observed at 536 cm^{-1} is shifted to 520 cm^{-1}, respectively. These findings confirmed the incorporation of Zn into $CuWO_4$ nanoparticles and well-agreed with the XRD results.

Fig.3 shows the SEM image of $CuWO_4$ and Zn-doped $CuWO_4$ nanoparticles. In $CuWO_4$ image, the uniformly synthesized particles are distributed over the surface and are strongly aggregated with one another in the form of network-like structure [13]. In the case of Zn-doped $CuWO_4$, the strongly aggregated particles are randomly distributed over the surface with fine grains. These observations strongly suggest the incorporation of zinc into $CuWO_4$. Interestingly, the surface decoration of zinc into $CuWO_4$ promotes efficient charge separation and it may increase the efficiency of the photocatalyst [14].

The EDX spectrum clearly evidenced the W-rich $CuWO_4$ and Zn-$CuWO_4$ nanocomposites. From the EDX analysis, the existence of Cu, W,

O and Zn signals confirms the synthesized product. The elemental composition of both $CuWO_4$ and Zn-$CuWO_4$ nanoparticles is given in Table 1 and Table 2. The non-stoichiometric ratio of the obtained nanoparticles is due to the formation of WO_3 as an additional product which is in turn reflected by W-rich $CuWO_4$ andZn-$CuWO_4$ nanoparticles.

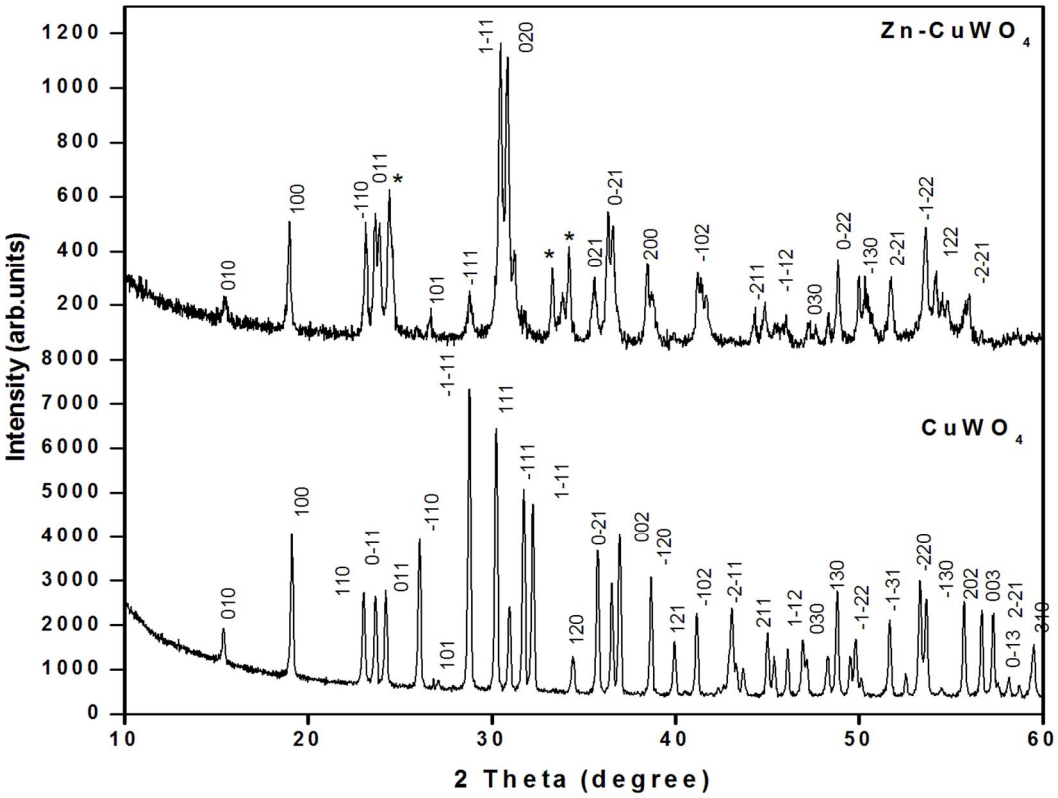

FIG. 1. XRD patterns of $CuWO_4$ and Zn-doped $CuWO_4$ nanoparticles.

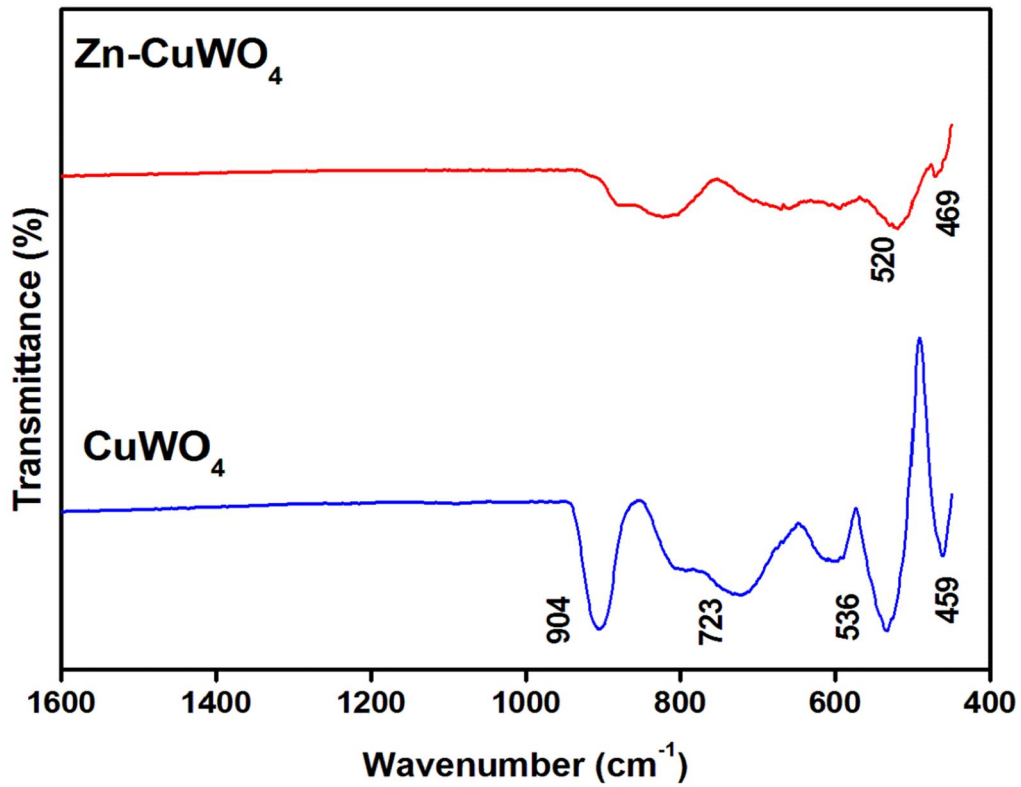

FIG.2.FTIR Spectra of $CuWO_4$ and Zn-doped $CuWO_4$ nanoparticles.

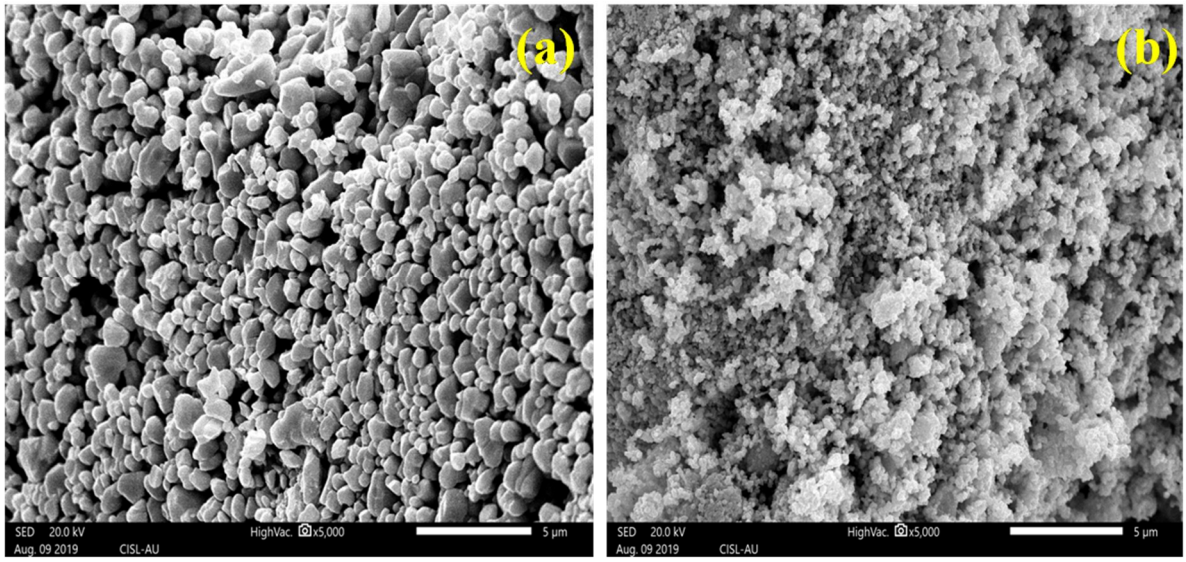

FIG.3. SEM images of (a) $CuWO_4$ and (b) Zn-doped $CuWO_4$ nanoparticles.

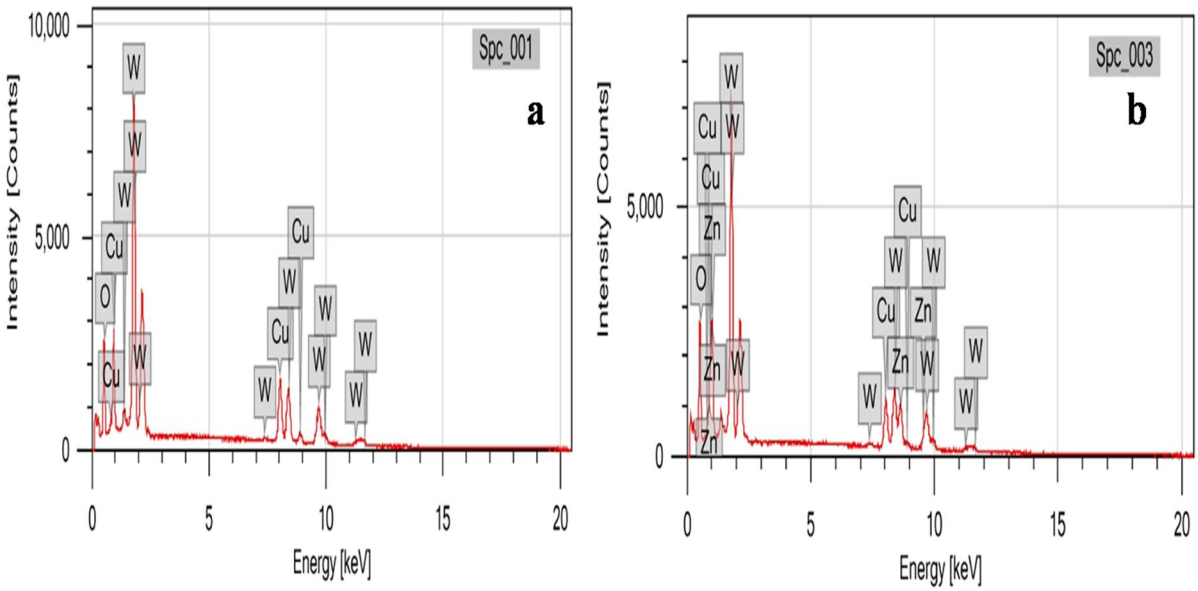

FIG.4. EDX Spectrum of (a) $CuWO_4$ and (b) Zn-doped $CuWO_4$ nanoparticles.

TABLE 1.Elemental composition of $CuWO_4$.

S. No.	Element	Mass (%)	Atom (%)
1	O	11.68	50.03
2	Cu	24.13	26.04
3	W	64.19	23.93
Total		100.00	100.00

TABLE 2. Elemental composition of Zn doped $CuWO_4$.

S. No.	Element	Mass (%)	Atom (%)
1	O	12.03	48.52
2	Cu	15.06	15.30
3	Zn	16.62	16.41
4	W	56.29	19.77
Total		100.00	100.00

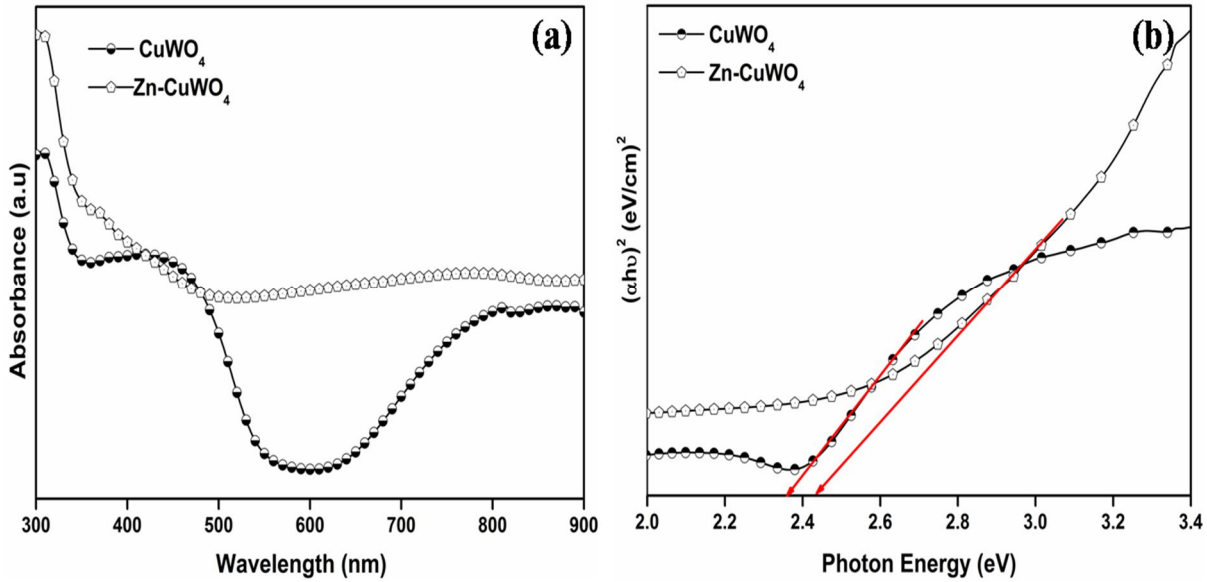

FIG.5.(a) UV-vis absorption spectra and (b) Tauc's plot of $CuWO_4$ and Zn-doped $CuWO_4$ nanoparticles.

The UV-vis absorption spectra of $CuWO_4$ and Zn-doped $CuWO_4$ are shown in Fig.5a. From the spectra, it is observed that both the $CuWO_4$ and Zn-doped $CuWO_4$ possess maximum absorption in the visible region. The band gap values are estimated from Tauc's plot and found to be 2.36 eV and 2.44 eV for $CuWO_4$ and Zn-doped $CuWO_4$, respectively. The increase in bandgap values of Zn-doped $CuWO_4$ may be attributed to incorporation of zinc ions which usually possess elevated conduction band levels [15]. However, the obtained bandgap values for $CuWO_4$ are lower than previously reported results [16, 17]. Moreover, the relatively lower bandgap of $CuWO_4$ allows it to absorb a wider range of visible region and hence it can be effectively used as a photoanode for solar water splitting [18].

4. Conclusion

In this work, we report $CuWO_4$ and Zn-doped $CuWO_4$ nanoparticles synthesized by solid-state reaction method. The XRD study confirms the triclinic crystal structure for both samples. For Zn-doped $CuWO_4$ nanoparticle, the shift in peak position indicates the successful incorporation of zinc into $CuWO_4$ without affecting the crystal structure.The FTIR spectrum shows the presence of Cu-O, W-O and Zn-O stretching vibrations, which confirms the formation of $CuWO_4$ and Zn-doped $CuWO_4$ particles. The SEM images of $CuWO_4$ nanoparticles show densely aggregated particles in which zinc was decorated over the surface of $CuWO_4$ particles. The band gap value is found to be 2.36 eV for $CuWO_4$ and 2.44 eV for Zn-doped $CuWO_4$. Hence, it is concluded that dopant zinc could modify the structural, optical and morphological properties and thus it can be used as a photoanode for solar water splitting.

Acknowledgement

The authors express their sincere thanks to DST-SERB (EMR/2017/000351), New Delhi for providing financial assistance to this research work. We thank UGC-SAP, DST-FIST, New Delhi for providing financial support to Department of Physics, Manonmaniam Sundaranar University, Tirunelveli.

References

[1] Gawande, M.B., Goswami, A., Felpin, F.X., Asefa, T., Huang, X., Silva, R. and Varma, R.S., Chemical Reviews, 116(2016) 3722.

[2] Yourey, J.E. and Bartlett, B.M., Journal of MaterialsChemistry, 21 (2011) 7651.

[3] Martínez-García, A., Vendra, V.K., Sunkara, S., Haldankar, P., Jasinski, J. and Sunkara, M.K., Journal of MaterialsChemistry A, 48 (2013) 15235.

[4] Yan, W., Liu, X., Hou, S. and Wang, X.,Catalysis Science &Technology, 5 (2019) 1141.

[5] Gohari, M.S. and Yangjeh, A.H.,Ceramic International, 43 (2017) 063.

[6] Pirhashemi, M. and Yangjeh, A.H., Journal of Colloids and Interface Science, 491 (2017) 216.

[7] Hill, J.C. and Choi, K.S., Journal of MaterialsChemistry A, 16 (2013) 5006.

[8] Yang, J., Li, C.and Diao, P., ElectrochimicaActa, 308 (2019) 195.

[9] Li, C. and Diao, P., Electrochimica Acta, 121(2020)136471.

[10] Montini, T., Gombac, V., Hameed, A., Felisari, L., Adami, G. and Fornasiero, P., Chemical PhysicsLetters, 498 (2010) 113.

[11] Mohamed, M.M., Ahmed, S.A. and Khairou, K.S.,AppliedCatalysis B: Environmental, 150 (2014) 63.

[12] Xu, Y., Jiao, X. and Chen, D., The Journal of Physical Chemistry C,43 (2008) 16769.

[13] Li, C., Guo, B., Peng, B., Yue, C. and Diao, P., International Journal of Electrochemical Science, 14 (2019) 9017.

[14] Bohra, D. and Smith, W.A., Physical Chemistryand Chemical Physics, 17 (2015) 9857.

[15] Yourey, J.E., Kurtz, J.B. and Bartlett, B.M., InorganicChemistry, 51 (2012) 10394.

[16] Jin, T., Diao, P., Xu, D. and Wu, Q.,Electrochimica Acta, 114 (2013) 271.

[17] Hill, J.C. and Choi, K.S., Journal of MaterialsChemistry A, 16 (2013) 5006.

[18] Hu, D., Diao, P., Xu, D., Xia, M., Gu, Y., Wu, Q. and Yang, S.,Nanoscale, 11 (2016) 5892.

المراجع: يجب طباعة المراجع بأسطر مزدوجة ومرقمة حسب تسلسلها في النص. وتكتب المراجع في النص بين قوسين مربعين. ويتم اعتماد اختصارات الدوريات حسب نظام Wordlist of Scientific Reviewers.

الجداول: تعطى الجداول أرقاما متسلسلة يشار إليها في النص. ويجب طباعة كل جدول على صفحة منفصلة مع عنوان فوق الجدول. أما الحواشي التفسيرية، التي يشار إليها بحرف فوقي، فتكتب أسفل الجدول.

الرسوم التوضيحية: يتم ترقيم الأشكال والرسومات والرسومات البيانية (المخططات) والصور، بصورة متسلسلة كما وردت في النص.

تقبل الرسوم التوضيحية المستخرجة من الحاسوب والصور الرقمية ذات النوعية الجيدة بالأبيض والأسود، على ان تكون أصيلة وليست نسخة عنها، وكل منها على ورقة منفصلة ومعرفة برقمها بالمقابل. ويجب تزويد المجلة بالرسومات بحجمها الأصلي بحيث لا تحتاج إلى معالجة لاحقة، وألا تقل الحروف عن الحجم 8 من نوع Times New Roman، وألا تقل سماكة الخطوط عن 0.5 وبكثافة متجانسة. ويجب إزالة جميع الألوان من الرسومات ما عدا تلك التي ستنشر ملونة. وفي حالة إرسال الرسومات بصورة رقمية، يجب أن تتوافق مع متطلبات الحد الأدنى من التمايز (1200 dpi Resolution) لرسومات الأبيض والأسود الخطية، و 600 dpi للرسومات باللون الرمادي، و300 dpi للرسومات الملونة. ويجب تخزين جميع ملفات الرسومات على شكل (jpg)، وأن ترسل الرسوم التوضيحية بالحجم الفعلي الذي سيظهر في المجلة. وسواء أرسل المخطوط بالبريد أو عن طريق الشبكة (Online)، يجب أرسال نسخة ورقية أصلية ذات نوعية جيدة للرسومات التوضيحية.

مواد إضافية: تشجع المجلة الباحثين على إرفاق جميع المواد الإضافية التي يمكن أن تسهل عملية التحكيم. وتشمل المواد الإضافية أي اشتقاقات رياضية مفصلة لا تظهر في المخطوط.

المخطوط المنقح (المعدّل) والأقراص المدمجة: بعد قبول البحث للنشر وإجراء جميع التعديلات المطلوبة، فعلى الباحثين تقديم نسخة أصلية ونسخة أخرى مطابقة للأصلية مطبوعة بأسطر مزدوجة، وكذلك تقديم نسخة إلكترونية تحتوي على المخطوط كاملا مكتوبا على Microsoft Word for Windows 2000 أو ما هو استجد منه. ويجب إرفاق الأشكال الأصلية مع المخطوط النهائي المعدل حتى لو تم تقديم الأشكال إلكترونيا. وتخزن جميع ملفات الرسومات على شكل (jpg)، وتقدم جميع الرسومات التوضيحية بالحجم الحقيقي الذي ستظهر به في المجلة. ويجب إرفاق قائمة ببرامج الحاسوب التي استعملت في كتابة النص، وأسماء الملفات على قرص مدمج، حيث يعلَم القرص بالاسم الأخير للباحث، وبالرقم المرجعي للمخطوط للمراسلة، وعنوان المقالة، والتاريخ. ويحفظ في مغلف واقٍ.

حقوق الطبع

يُشكِّل تقديم مخطوط البحث للمجلة اعترافاً صريحاً من الباحثين بأنّ مخطوط البحث لم يُنْشَر ولم يُقَدَّم للنشر لدى أي جهَة أخرى كانت وبأي صيغة ورقية أو إلكترونية أو غيرها. ويُشترط على الباحثين ملء أنموذج يَنُصُّ على نقْل حقوق الطبع لتُصبح ملكاً لجامعة اليرموك قبل الموافقة على نشر المخطوط. ويقوم رئيس التحرير بتزويد الباحثين بإنموذج نقل حقوق الطبع مع النسخة المُرْسَلَة للتنقيح. كما ويُمنع إعادة إنتاج أيِّ جزء من الأعمال المنشورة في المجلّة من دون إذن خَطِّيٍّ مُسبَق من رئيس التحرير.

إخلاء المسؤولية

إن ما ورد في هذه المجلة يعبر عن آراء المؤلفين، ولا يعكس بالضرورة آراء هيئة التحرير أو الجامعة أو سياسة اللجنة العليا للبحث العلمي أو وزارة التعليم العالي والبحث العلمي. ولا يتحمل ناشر المجلة أي تبعات مادية أو معنوية أو مسؤوليات عن استعمال المعلومات المنشورة في المجلة أو سوء استعمالها.

الفهرسة: المجلة مفهرسة في:

Scopus	ULRICHSWEB GLOBAL SERIALS DIRECTORY

معلومات عامة

المجلة الأردنية للفيزياء هي مجلة بحوث علميّة عالمية متخصصة مُحكمة تصدر بدعم من صندوق دعم البحث العلمي، وزارة التعليم العالي والبحث العلمي، عمان، الأردن. وتقوم بنشر المجلة عمادة البحث العلمي والدراسات العليا في جامعة اليرموك، إربد، الأردن. وتنشر البحوث العلمية الأصيلة، إضافة إلى المراسلات القصيرة Short Communications، والملاحظات الفنية Technical Notes، والمقالات الخاصّة Feature Articles، ومقالات المراجعة Review Articles، في مجالات الفيزياء النظرية والتجريبية، باللغتين العربية والإنجليزية.

تقديم مخطوط البحث

تقدم البحوث عن طريق إرسالها إلى البريد الإلكتروني : jjp@yu.edu.jo

تقديم المخطوطات إلكترونيًا: اتبع التعليمات في موقع المجلة على الشبكة العنكبوتية.

ويجري تحكيمُ البحوثِ الأصيلة والمراسلات القصيرة والملاحظات الفنية من جانب مُحكّمين اثنين في الأقل من ذوي الاختصاص والخبرة. وتُشَجّع المجلة الباحثين على اقتراح أسماء المحكمين. أما نشر المقالات الخاصّة في المجالات الفيزيائية النَشِطَة، فيتم بدعوة من هيئة التحرير، ويُشار إليها كذلك عند النشر. ويُطْلَب من كاتب المقال الخاص تقديم تقرير واضح يتّسم بالدقة والإيجاز عن مجال البحث تمهيداً للمقال. وتنشر المجلةُ أيضاً مقالات المراجعة في الحقول الفيزيائية النشطة سريعة التغيُّر، وتُشَجّع كاتبي مقالات المراجعة أو مُستَكتبيها على إرسال مقترحٍ من صفحتين إلى رئيس التحرير. ويُرْفَق مع البحث المكتوب باللغة العربية ملخص (Abstract) وكلمات دالة (Keywords) باللغة الإنجليزية.

ترتيب مخطوط البحث

يجب أن تتم طباعة مخطوط البحث ببنط 12 نوعه Times New Roman، وبسطر مزدوج، على وجه واحد من ورق A4 (21.6 × 27.9 سم) مع حواشي 3.71 سم ، باستخدام معالج كلمات ميكروسوفت وورد 2000 أو ما استَجَد منه. ويجري تنظيم أجزاء المخطوط وفق الترتيب التالي: صفحة العنوان، الملخص، رموز التصنيف (PACS)، المقدّمة، طرق البحث، النتائج، المناقشة، الخلاصة، الشكر والعرفان، المراجع، الجداول، قائمة بدليل الأشكال والصور والإيضاحات، ثَمَّ الأشكال والصور والإيضاحات. وتُكْتَب العناوين الرئيسة بخطٍ **غامق**، بينما تُكْتَب العناوين الفرعية بخطٍ *مائل*.

صفحة العنوان: وتشمل عنوان المقالة، أسماء الباحثين الكاملة وعناوين العمل كاملة. ويكتب الباحث المسؤول عن المراسلات اسمه مشارا إليه بنجمة، والبريد الإلكتروني الخاص به. ويجب أن يكون عنوان المقالة موجزا وواضحا ومعبرا عن فحوى (محتوى) المخطوط، وذلك لأهمية هذا العنوان لأغراض استرجاع المعلومات.

الملخص: المطلوب كتابة فقرة واحدة لا تزيد على مائتي كلمة، موضحة هدف البحث، والمنهج المتبع فيه والنتائج وأهم ما توصل إليه الباحثون.

الكلمات الدالة: يجب أن يلي الملخص قائمة من 4-6 كلمات دالة تعبر عن المحتوى الدقيق للمخطوط لأغراض الفهرسة.

PACS: يجب إرفاق الرموز التصنيفية، وهي متوافرة في الموقع http://www.aip.org/pacs/pacs06/pacs06-toc.html.

المقدمة: يجب أن توضّح الهدف من الدراسة وعلاقتها بالأعمال السابقة في المجال، لا أن تكون مراجعة مكثفة لما نشر (لا تزيد المقدمة عن صفحة ونصف الصفحة مطبوعة).

طرائق البحث (التجريبية / النظرية): يجب أن تكون هذه الطرائق موضحة بتفصيل كاف لإتاحة إعادة إجرائها بكفاءة، ولكن باختصار مناسب، حتى لا تكون تكرارا للطرائق المنشورة سابقا.

النتائج: يستحسن عرض النتائج على صورة جداول وأشكال حيثما أمكن، مع شرح قليل في النص ومن دون مناقشة تفصيلية.

المناقشة: يجب أن تكون موجزة وتركز على تفسير النتائج.

الاستنتاج: يجب أن يكون وصفا موجزا لأهم ما توصلت إليه الدراسة ولا يزيد عن صفحة مطبوعة واحدة.

الشكر والعرفان: الشكر والإشارة إلى مصدر المنح والدعم المالي يكتبان في فقرة واحدة تسبق المراجع مباشرة.

Subscription Form

Jordan Journal of

PHYSICS

An International Peer-Reviewed Research Journal issued by the Support of the Scientific Research Support Fund

Published by the Deanship of Research & Graduate Studies, Yarmouk University, Irbid, Jordan

Name: ..... الأسم:

Specialty:..... التخصص:

Address: ..... العنوان:

P.O. Box:..... صندوق البريد:

City & Postal Code: ..... المدينة/الرمز البريدي:

Country: ..... الدولة:

Phone: ..... رقم الهاتف:

Fax No:..... رقم الفاكس:

E-mail:..... البريد الإلكتروني:

No. of Subscription: ..... عدد الإشتراكات:

Method of Payment:..... طريقة الدفع:

Amount Enclosed:..... المبلغ المرفق:

Signature: ..... التوقيع:

Cheques should be paid to Deanship of Research and Graduate Studies - Yarmouk University.

I would like to subscribe to the Journal
For

- One Year
- Two Years
- Three Years

One Year Subscription Rates

	Inside Jordan	Outside Jordan
Individuals	JD 8	€ 40
Students	JD 4	€ 20
Institutions	JD 12	€ 60

Correspondence

Subscriptions and Sales:

Prof. Ibrahim O. Abu Al-Jarayesh
Deanship of Research and Graduate Studies
Yarmouk University
Irbid – Jordan
Telephone: 00 962 2 711111 Ext. 2075
Fax No.: 00 962 2 7211121

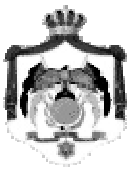

المملكة الأردنية الهاشمية

جامعة اليرموك

المجلة الأردنية

للفيزياء

مجلة بحوث علمية عالمية متخصصة محكّمة

تصدر بدعم من صندوق دعم البحث العلمي

المجلد (14)، العدد (5)، كانون الأول 2021م / جمادى الأولى 1443هـ

المجلة الأردنية

للفيزياء

مجلة بحوث علمية عالمية محكّمة

المجلد (14)، العدد (5)، كانون الأول 2021م / جمادى الأولى 1443هـ

المجلة الأردنية للفيزياء: مجلة علمية عالمية متخصصة محكّمة تصدر بدعم من صندوق دعم البحث العلمي، عمان، الأردن، وتصدر عن عمادة البحث العلمي والدراسات العليا، جامعة اليرموك، إربد، الأردن.

ترسل البحوث إلى العنوان التالي:

الأستاذ الدكتور إبراهيم عثمان أبو الجرايش
رئيس تحرير المجلة الأردنية للفيزياء
عمادة البحث العلمي والدراسات العليا، جامعة اليرموك
إربد ، الأردن
هاتف 7211111 2 962 00 **فرعي** 2075

E-mail: *jjp@yu.edu.jo* **Website**: *http://Journals.yu.edu.jo/jjp*